

# University of St Andrews

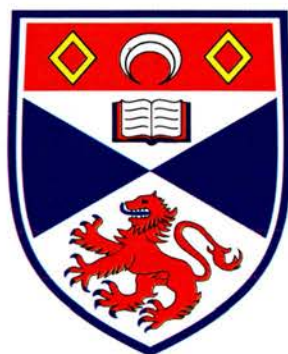


Full metadata for this thesis is available in  
St Andrews Research Repository  
at:

<http://research-repository.st-andrews.ac.uk/>

This thesis is protected by original copyright

# Tunable Monolithic Coupled Cavity Lasers



University  
of  
St Andrews

Donald Henderson Brown M.Eng.

October, 2005

A Thesis submitted to the School of Physics and Astronomy, at the  
University of St. Andrews, for the degree of Doctor of Philosophy.



Th F87

# Declaration

I, Donald Henderson Brown, hereby certify that this thesis, approximately 40,000 words in length, has been written by me, that it is a record of work carried out by me and that it has not been submitted in any applications for a higher degree.

Date: 18/10/05 ..... Signature of Candidate:

I was admitted as a research student and as a candidate for the degree of Doctor of Philosophy in April 2000: the higher study for which this is a record was carried out at the University of St. Andrews between April 2000 and April 2005.

Date: 18/10/05 ..... Signature of Candidate:.

I hereby certify that the candidate has fulfilled the conditions of the Resolution and Regulations appropriate for the degree of Doctor of Philosophy in the University of St. Andrews and that the candidate is qualified to submit this thesis in application for that degree.

Date: 19/10/05 ..... Signature of Supervisor:.

In submitting this thesis to the University of St. Andrews I understand that I am giving permission for it to be made available for use in accordance with the regulations of the University Library for the time being in force, subject to any copyright vested in the work not being affected thereby. I also understand that the title and abstract will be published, and that a copy of the work may be made and supplied to any *bona fide* library or research/worker.

Date: 18/10/05 ..... Signature of Candidate:.

# Dedication

*Velsign, o Gud, månen som er over meg.  
Velsign, o Gud, jorden som er under meg.  
Velsign, o Gud, min ektefelle og mine barn.  
og velsign, o Gud, meg selv og min omsorg for dem.*

*Velsign, o Gud, de ting som mine øyne hviler på.  
Velsign, o Gud, de ting som mitt håp hviler på.  
Velsign, o Gud, min forstand og mitt forsett.  
Velsign dem du, livets Gud.*

*Velsign min kjærlighets livsledsager.  
Velsign mine hendes gjerning.  
Velsign, ja velsign mitt forsvars innhenging  
og velsign den evige hvile for meg.*

*For C, M & J*

# Acknowledgements

The realisation of this work would not have been possible without the assistance and support from a large number of people. I realise that it is almost impossible to grant everyone the thanks and regards which he or she wholeheartedly deserves. I can only hope that no offence will be taken if I should forget anyone.

## **University of St. Andrews**

First, I would like to thank Thomas F. Krauss, Professor at the School of Physics & Astronomy, University of St. Andrews. I am deeply indebted to his kind support and confidence throughout the time of this project. I would also like to acknowledge the past and present members of the Microphotonics & Photonic Crystals research group, with whom I have enjoyed working in the stimulating and exciting environment they have provided.

No research team could exist without the efforts of its technical staff. Mr. George Robb must be acknowledged for all of his activities in the design, creation and maintenance of the cleanroom facility of St. Andrews.

This work has benefited from the collaboration of many colleagues, I would especially like to thank Dr. Michael Flynn, Dr. William Whelan-Curtin, Dr. Michael Mazilu Dr. Maria Kotlyar and Dr. Tim Karle for all their efforts and contributions. Last but by no means least I'd like to offer a heart felt thanks to Dr. Robert Wilson for his frequent and revealing insights into the human condition.

## **IntensePhotonics**

I would like to express my appreciation to the industrial members of the project, Prof. John Marsh, Dr. Christopher M. Smith, both for their financial and technical support. I would further like to thank Dr. Dan Yanson for his time and effort in explaining the fabrication and operation of harmonic modelocked compound-cavity lasers and for the numerous contributions to my own designs.

**USSL - University of Glasgow**

I would like to express my appreciation to Dr. Steve Thoms and Dr. Douglas Macintyre, for the use of the ultra-small structures laboratory. Their contribution and regular discussions regarding the workings of their Leica EBPG 5-HR100 electron beam exposure tool and the practicalities of proximity correction methods, have proven both insightful and invaluable. I'd also like to mention the staff of the USSL and Dry Etch facilities, Mr. Robert Harkins for all his assistance with file transfer and data recovery, Dave and Helen for always being available and willing to assist no matter what the problem, Dave Clifton, Colin Roberts and Ronnie Roger for almost always 'finding' a slot and then achieving the impossible.

**University of York**

I would like to express my gratitude to Dr. Eugene Avrutin and gratefully acknowledge the input of fellow research student Ben for the work they have conducted on modelling the coupled cavity devices demonstrated.

**National Centre for III-V Technologies - University of Sheffield**

I would like to acknowledge Dr. John S. Roberts and Dr. Matthew Steer from the National Centre for III-V Technologies for the growth and supply of semiconductor materials and provision of photoluminescence results.

**In the Back Kitchen**

It would be inappropriate not to mention at least some of the friends and colleges, without whom the experience of conducting the PhD program would have been very different. Firstly, I would like to express my appreciation to Prof. Lars Othar Svaasand for starting the ball rolling and smoothing the way for my departure from NTNU. A special thanks to Craig Hamilton for remaining a true friend and his insistence that I complete the project and repay his taxes, Juraj Chmelar for being incredibly supportive and always pleasantly surprising me with kind words and actions, Torfinn Utne and Pauline Haddow for providing reason when there seemed none, Sverre 'Georgie Boy' Pettersen for his assistance with all that 'gulv-list' and continual updates on the career of the heroic Morten Abel, Snorre Aunet for always finding and expressing the 'other' other point of view. Finally Jennifer, Mandy and Andrew 'Treehorn' Mclean for their support at these final stages.

I would finally like to thank Mr. Gregor Duncan, for his invaluable contributions to the overall thesis text and document layout and for his patience in

*ACKNOWLEDGEMENTS*

v

reading and correcting, I can only hope that the finished document in some small way reaches an acceptable standard.

# Abstract

This thesis reports on the research activities conducted under the Tunable Monolithic Coupled Cavity Laser project at the School of Physics & Astronomy, University of St. Andrews.

The design, fabrication and testing of monolithic coupled cavity semiconductor lasers is presented. Coupled cavity lasers are formed by electrically and optically sectioning a single mode ridge waveguide using air slots of appropriate widths. A method for creating deeply etched features using a chemically assisted ion beam etching (CAIBE) process was developed. Etch depths greater than  $2.2 \mu\text{m}$  in GaAs/AlGaAs substrates were routinely demonstrated.

Electron beam lithography is used to define the sub-wavelength features of the pattern which act as inter-cavity reflectors and one dimensional Bragg mirrors. The effects of proximity exposure was found to be prevalent and methods for compensating for the effects of proximity exposure were investigated. The development of the correction method for this effect is described and results presented. Some work was conducted on the application of the proximity correction methods to photonic crystal coupled cavity patterns, resulting in planar photonic-crystal coupled cavity waveguides and photonic crystal based curved reflectors.

The devices were fabricated from GaAs/AlGaAs material containing two InGaAs quantum wells, demonstrating emission around a wavelength of 980 nm. Monolithic integration of the device is achieved by substituting one feedback mirror with a 1-Dimensional Bragg reflector. Lasers demonstrating side-mode suppression ratios upwards of 35 dB and tuning ranges over 4 nm have been fabricated. Modelling of the tuning mechanism based on cavity interactions provided values which were in good agreement with the measured results.

# Publications

## Publications

Tim J. Karle, Donald H. Brown, Robert Wilson, Matthew Steer and Thomas F. Krauss, "Planar Photonic Crystal Coupled Cavity Waveguides", *IEEE Journal of Selected Topics in Quantum Electronics*, Vol. 8(4), pp. 909-918 July/August 2002.

Donald H. Brown, Michael B. Flynn, Liam OFaolain, and Thomas F. Krauss, "Low Tuning Current Semiconductor Coupled-Cavity Lasers Incorporating Bragg Reflectors" *IEEE Photonics Technology Letters*, Estimated publication date October 2005.

## Conference Papers

Donald H. Brown, Michael B. Flynn, Liam O Faolain, Wilson Sibbett and Thomas F. Krauss, "Coupled Cavity Lasers Incorporating Bragg Mirrors" presented at *The 16<sup>th</sup> Annual Meeting of the IEEE Lasers and Electro-Optics Society*, Tucson Arizona, paper WL6, 2003.

Michael B. Flynn, Donald H. Brown, and Thomas F. Krauss, "Coupled Cavity Tunable Semiconductor Diode Lasers Incorporating Multi-Layer Mirrors" presented at *The 17<sup>th</sup> Annual Meeting of the IEEE Lasers and Electro-Optics Society*, Puerto Rico, 2004.

Liam OFaolain, Michael B. Flynn, Donald Brown and Thomas F. Krauss, "Q-Switched Modelocking of Semiconductor Lasers" presented at *Semiconductor and Integrated OptoElectronics04*, Cardiff, Wales April 5-7, 2004.

# Thesis Outline

This thesis is organised into seven chapters. Because of the breadth and nature of topics covered, it was often difficult to know exactly how to divide and where to place the topics covered by the thesis. The organisation of the thesis is as follow:

Chapter one presents an introduction to wavelength agile sources. A review of the technologies currently being utilised by key players in the field is conducted. The key applications and possible operating regimes for coupled cavity tunable lasers are presented. The chapter concludes by outlining the key aims and motivations behind the project.

In chapter two aspects pertaining to materials and the material structure used in the project are presented. A brief overview of semiconductors is presented followed by the methods used in determining material quality. Typical characterisation results of the material as it comes from the grower are presented. In concluding the chapter, the shortcomings of the characterisation technique used and sources of discrepancies are discussed.

The design of the laser structure is presented in chapter three. The creation of an optical ridge waveguide using material composition and physical dimensions is discussed. The creation and usefulness of Bragg reflectors as a cavity mirror is investigated and a case built for the use of high contrast/deeply etched mirrors. Finally a review of the device parameters and operating principles is presented.

Chapter four addresses the topic of fabrication, with regards to the single and dual cavity laser devices. The effect of ‘proximity exposure’ is discussed and the approach used to minimise/correct for this effect is presented. The methods of characterising the contacts and typical contact resistance measure-

ments obtained are presented.

The fifth chapter briefly reviews the evolution of the laser, outlining the key stages of device development during the life of the project.

In chapter six the experimental set-ups and results are discussed. The mechanisms involved in the cavity interactions are presented and the underlying model is applied to the cavity configurations created. Direct correlation to the predicted behaviour and observed results are made.

Conclusions on the viability of the coupled cavity laser configuration as a tunable source are drawn in chapter seven. Here, suggestions for areas of research where further work may provide interesting results are offered should the project be considered for continuation.

# Contents

<b>Declaration</b>	<b>i</b>
<b>Dedication</b>	<b>ii</b>
<b>Acknowledgements</b>	<b>iii</b>
<b>Abstract</b>	<b>vi</b>
<b>Publications</b>	<b>vii</b>
<b>Thesis Outline</b>	<b>viii</b>
<b>1 Introduction</b>	<b>1</b>
1.1 Introduction . . . . .	1
1.2 Semiconductor Laser Diodes . . . . .	1
1.2.1 A Historical Perspective . . . . .	3
1.2.2 Development of the Tunable Laser . . . . .	4
1.2.3 Single Frequency Lasers . . . . .	5
1.2.4 Tunable Laser Technologies . . . . .	10
1.3 Applications for Tunable Lasers . . . . .	17
1.3.1 Optical Communications Systems . . . . .	18
1.3.2 Optical Networking . . . . .	23
1.4 Aims and Motivation for Work . . . . .	25
<b>2 Material</b>	<b>28</b>
2.1 Introduction . . . . .	28
2.2 Semiconductor Overview . . . . .	28
2.2.1 Band Structure . . . . .	29
2.2.2 Doping Semiconductors . . . . .	32
2.2.3 The p-n Junction . . . . .	33

2.2.4	Quantum Wells . . . . .	37
2.3	Semiconductor Lasers . . . . .	38
2.3.1	Laser Prerequisites . . . . .	38
2.3.2	Material Structure Optimisation . . . . .	40
2.3.3	Material Gain . . . . .	44
2.4	Material Characterisation . . . . .	46
2.4.1	Broad Area Lasers . . . . .	46
2.4.2	Broad Area Analysis Theory . . . . .	46
<b>3</b>	<b>C3 Laser Design</b>	<b>50</b>
3.1	Introduction . . . . .	50
3.2	Material Design . . . . .	50
3.2.1	Semiconductor Slab Waveguide . . . . .	51
3.2.2	Single Mode Ridge Waveguide . . . . .	56
3.3	Cavity Mirrors . . . . .	58
3.3.1	Cleaved Facet . . . . .	58
3.3.2	Multilayer Stack . . . . .	59
3.3.3	Investigating the Grating Design . . . . .	64
3.4	Tunable Coupled Cavity Lasers . . . . .	68
3.4.1	Principles of Operation . . . . .	68
3.4.2	Cavity Length Ratios . . . . .	69
3.4.3	Inter Cavity Reflector . . . . .	71
3.4.4	Current Tuning . . . . .	75
3.4.5	Tunability . . . . .	79
<b>4</b>	<b>Fabrication</b>	<b>84</b>
4.1	Introduction . . . . .	84
4.2	Wafer Preparation . . . . .	84
4.2.1	Wafer Growth . . . . .	84
4.2.2	Silicon Dioxide Deposition . . . . .	85
4.3	Device Patterning . . . . .	86
4.3.1	Optical Lithography . . . . .	86
4.3.2	Electron Beam Lithography . . . . .	88
4.3.3	Electron Beam Proximity Effect . . . . .	92
4.3.4	Development . . . . .	102
4.4	Pattern Transfer . . . . .	104
4.4.1	Reactive Ion Etching . . . . .	104
4.4.2	Chemically Assisted Ion Beam Etching . . . . .	106
4.5	Coupled Cavity Laser Fabrication . . . . .	108
4.5.1	High Resolution Electron Beam Lithography . . . . .	108
4.5.2	Deeply Etched Bragg Reflectors and ICR . . . . .	109

4.5.3	Waveguide Ridge Definition . . . . .	110
4.5.4	Electrical Contact Isolation . . . . .	111
4.5.5	Electrical Contact Deposition . . . . .	113
4.6	Contact Characterisation . . . . .	114
4.6.1	Transmission Line Measurements . . . . .	116
4.6.2	2 Probe and 4 probe Setups . . . . .	118
4.6.3	Cleaving and Testing . . . . .	119
<b>5</b>	<b>Device Evolution</b>	<b>120</b>
5.1	Introduction . . . . .	120
5.2	Coupled Cavity Laser Device Design . . . . .	120
5.2.1	Towards Integration . . . . .	121
5.3	Design Iterations . . . . .	122
5.3.1	Design Stage 1 . . . . .	122
5.3.2	Design Stage 2 . . . . .	125
5.3.3	Design Stage 3 . . . . .	128
5.4	Device Summary . . . . .	130
<b>6</b>	<b>Experimental Results and Discussion</b>	<b>131</b>
6.1	Introduction . . . . .	131
6.2	Experiment . . . . .	131
6.2.1	Light/Current Measurements . . . . .	133
6.2.2	Tuning Spectra Measurements . . . . .	134
6.3	Results . . . . .	135
6.3.1	L-I Curves . . . . .	135
6.3.2	Tuning Curves - Long-Short Results . . . . .	136
6.3.3	Tuning Curves - Long-Long Results . . . . .	138
6.3.4	Overview of Results . . . . .	140
6.4	Basis for Operation . . . . .	143
6.4.1	Single Cavity Laser . . . . .	143
6.4.2	Coupled Cavity Laser . . . . .	144
6.5	Discussion . . . . .	149
6.5.1	Device Modelling . . . . .	150
<b>7</b>	<b>Conclusions and Further Work</b>	<b>156</b>
7.1	Introduction . . . . .	156
7.2	Conclusion on Results . . . . .	156
7.3	Suggestions for Further Work . . . . .	158
7.3.1	Further Investigation . . . . .	158
7.3.2	Towards Integration . . . . .	160
7.3.3	Possible Applications . . . . .	161

*CONTENTS*

xiii

7.4 Thesis Summary . . . . . 162

# List of Abbreviations

DBR - Distributed Bragg Reflector  
DFB - Distributed FeedBack  
SG-DBR - Sampled Grating-DBR  
SSG-DBR - Super Structure Grating-DBR  
CW - Continuous Wave  
LED - Light Emitting Diode  
FP - Fabry-Perot  
C<sup>3</sup> - Cleaved Coupled Cavity  
DHS - Double HeteroStructure  
S/D/MQW - Single/Double/Multiple Quantum Well  
RWG - Ridge WaveGuide  
VCSEL - Vertical Cavity Surface Emitting Laser  
ECL - External Cavity Laser  
ETECAL - Electrically Tunable External Cavity Laser  
LCA - Liquid Crystal Array  
EAM - Electro-Absorption Modulator  
TEC - Thermal Electric Cooler  
TTG-DFB - Tunable Twin Guide-DFB  
PLC - Planar Light Circuit  
SOA - Semiconductor Optical Amplifier  
(S)MSR - (Side) Mode Suppression Ratio  
RIN - Relative Intensity Noise  
MEMs - Micro-Electro Mechanical systems  
(D)WDM - (Dense) Wavelength Division Multiplexing  
IPoWDM - Internet Protocol over WDM

## CONTENTS

xv

AWG - Array WaveGuide

FBG - Fiber Bragg Grating

ITU - International Telecommunications Union

MOCVD - Metal Organic Chemical Vapor Deposition

PECVD - Plasma Enhanced Chemical Vapor Deposition

RIE - Reactive Ion Etching

CAIBE - Chemically Assisted Ion Beam Etching

PMMA - PolyMethyl-MethAcrylate

HSQ - Hydrogen SilsesQuioxane

EBL - Electron Beam Lithography

MIBK - MethylIsoButylKetone

SCCM - Standard Cubic Centimeters

# List of Variables

- $E$  - Energy of an electron  
 $p$  - Momentum of electron  
 $\bar{p}_c$  - Crystal momentum  
 $m_0$  - Electron mass  
 $e$  - Charge of an electron  
 $c$  - Velocity of light  
 $m_n, m^*$  - Electron effective mass  
 $E_g$  - Bandgap energy  
 $\epsilon$  - Material permittivity  
 $\epsilon_0$  - Permittivity of vacuum  
 $n_i$  - Refractive index of material 'i'  
 $n_{\text{eff}}$  - Effective refractive index  
 $\rho$  - Density of states  
 $\hbar$  - Plank's constant (reduced)  
 $\omega$  - Angular frequency  
 $k_i$  - Wave number in material 'i'  
 $\lambda$  - Wavelength  
 $F$  - Optical flux density  
 $g$  - Optical gain coefficient  
 $\alpha$  - Optical absorption coefficient  
 $R_i$  and  $T_i$  - Reflection and Transmission coefficient from interface 'i'  
 $L, L_{\text{opt}}, w, d, l_i, L_{\text{gap}}$  - Length  
 $g_{\text{th}}$  - Optical threshold gain  
 $g_w$  - Peak quantum well gain  
 $J_{\text{th}}$  - Threshold current density

- $J_{tr}$  - Transparent current density  
 $J_w$  - Quantum well injected current density  
 $G_{th}$  - Modal threshold gain  
 $I_{th}$  - Threshold current  
 $\Gamma, \Gamma_w$  - Optical confinement factor (quantum well)  
 $n_w, n_{opt}$  - Number of quantum wells (optimum)  
 $\eta_{int}, \eta_{inj}, \eta_{ext}$  - Internal, injection and external quantum efficiencies,  
 $g_m$  - Material gain  
 $f_c, f_v$  - Fermi-Dirac probability coefficients  
 $\varphi_{ij}$  - Phase shift at interface between materials 'i' and 'j'  
 $V, b, a$  and  $d$  - Normalised frequency, propagation and asymmetry parameters  
 $N, P$  - Free electron and hole concentrations  
 $\alpha, \beta$  and  $\eta$  - Proximity correction parameters (Chapter 4)  
 $R_{tot}, R_{s*}$  and  $R_C$  - Total, Sheet and Contact resistances (Chapter 4)  
 $E$  - Electric field strength  
 $H$  - Magnetic field strength

# Chapter 1

## Introduction

### 1.1 Introduction

In this chapter, an introduction to semiconductor lasers is presented. The chapter begins with Section 1.2 where a brief history of semiconductor laser development from the ideas put forward by Arthur Schawlow and Charles Townes to the latest work on widely-tunable Superstructure grating (SSG) distributed Bragg reflector (DBR) lasers. Attention is drawn to the design and technological milestones associated with the development of present day tunable lasers.

The dominant applications for which semiconductor lasers have found use are discussed in Section 1.3. A brief overview of typical communications systems and the roles that tunable lasers play to increase and optimise the utilisation of existing in-situ optical networks is covered. A review of the coupled cavity laser configuration, the component for the main body of work which has been conducted is presented. The final section of this chapter, Section 1.4 presents the aims and motivations for this project.

### 1.2 Semiconductor Laser Diodes

The principal of Light Amplification through Stimulated Emission of Radiation (LASER) was first demonstrated by Theodore H. Maiman in 1960 [1] at the

Hughes Laboratory, California. Maiman's pioneering advancement followed on from the work of Arthur L. Schawlow and Charles H. Townes [2] of Bell Laboratories<sup>1</sup>. Maiman is accredited with the invention of the first solid state laser, formed from a crystal of ruby pumped by a high intensity flash lamp. When the flash lamp was activated, an intense pulse of (red) optical radiation was emitted from the facet of the ruby etalon. The emitted radiation displayed two distinct features of laser radiation i.e. it was both monochromatic and coherent. Within a short period of time, lasing action had been demonstrated in further solid state, gaseous, liquids and semiconductor crystal media<sup>2</sup>.

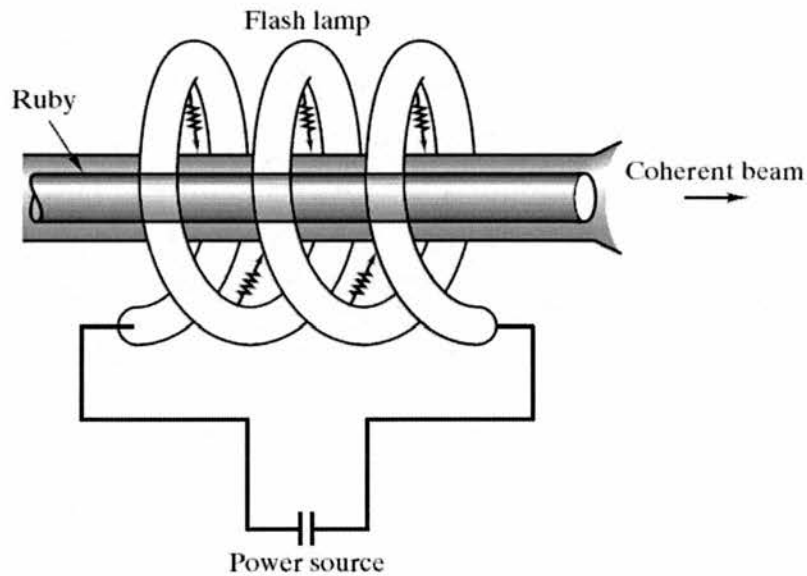


**Figure 1.1:** Figure of a typical Ruby Laser

<sup>1</sup>Schawlow and Townes published the basic principles of the laser in 1958, and are reputed to have described it as 'a solution looking for a problem'

<sup>2</sup>Solid State lasers should not be confused with Semiconductor or Diode lasers which although being 'solid state' are almost always electrically pumped

### 1.2.1 A Historical Perspective

During 1962, four separate research groups [3, 4, 5, 6] reported the observation of stimulated emission from homojunction gallium arsenide (GaAs) semiconductor diodes. The material structures of these early laser were based on the simple p-n junction, which due to its nature is not the most ideal of solutions, the primary concern being the overheating and eventual junction failure. Lasers employing a single semiconductor, i.e. GaAs, require a significant amount of pumping in order to initiate the lasing action. Various methods of achieving CW operation using these structures were investigated, when finally in 1963, Herbert Kroemer and Zhores Ivanovich Alfyorov proposed independently the approach of using a semiconductor sandwich structure, more commonly known as the heterostructure.

By incorporating a thin layer of different material with a slightly smaller band gap between two slabs of bulk material, one can effectively confine the process of population inversion and hence the process of lasing to this ‘active’ region. The optical mode generated through the recombination process is localised to the region immediately surrounding the active layer. Although Alfyorov’s early experiments, based on GaP-GaAs, proved to be fruitless, a breakthrough occurred in 1967. Alfyorov, then in the Soviet Union, and Hans Rupperecht and Jerry Woodall at IBM, independently reported the first GaAs-AlGaAs heterojunctions grown by liquid-phase epitaxy. GaAs-AlGaAs eventually emerged as the material pairing of choice, once researchers correctly recognized the close values of their lattice constants and realized that, whereas AlAs will oxidize in air, the binary alloy  $\text{Al}_x\text{Ga}_{1-x}\text{As}$  is chemically stable for low to moderate Al concentrations.

In 1970, continuous-wave (CW) room-temperature semiconductor lasers were at last reported, in GaAs-AlGaAs double heterostructure (DHS) devices, by Alferov, and one month later by Izuo Hayashi and Morton Panish of Bell Labs. Ternary compounds, such as GaAsP and InGaAs, and quaternary compounds like InGaAsP also received much attention. In 1974, Raymond Dingle and company at Bell Labs reported observing quantized size effects. Exploiting this reduced dimensionality, Dupuis, Dapkus, Holonyak,

and coworkers reported a CW room-temperature quantum well laser in 1978 [7, 8]. From these heterostructures incorporating two-dimensional quantum wells, researchers have explored even fewer dimensions i.e. one-dimensional quantum wires and zero-dimensional quantum dots in addition to structures ultimately with single-atom thicknesses.

The controlled layer deposition facilitated the fabrication and study of heterostructure superlattices by Leo Esaki, Raphael Tsu, and Leroy Chang at IBM, which have in turn led to resonant tunnel diodes and quantum cascade lasers developed by Federico Capasso at Bell Labs Lucent Technologies. Near-infrared semiconductor lasers and LEDs are now commonplace. The telecommunications industry has blossomed with the development of long-wavelength InGaAsP heterostructure lasers, lattice-matched to InP substrates, for use with optical fibers. Recent developments within the AlGaInN material base permit heterostructures capable of producing blue and violet emitting diode lasers and LEDs. Heterostructures have emerged as the basic building block of semiconductor devices.

### 1.2.2 Development of the Tunable Laser

The development of the modern semiconductor laser stems from work conducted by Prof. Yasuharu Suematra. Suematra's group at the Tokyo Institute of Technology was responsible for early developmental work leading to distributed-Bragg-reflector (DBR) lasers incorporating discrete active and passive grating reflector regions [9, 10].

In their infancy, early laser diodes were based upon the simple Fabry-Perot cavity. In this arrangement the cavity facets, formed while cleaving the laser chip from the substrate, act as mirrors providing optical feedback for the laser. The Fabry-Perot (FP) cavity supports oscillation over several longitudinal modes, the frequencies of which correspond to the different FP resonances sustainable by the gain spectrum of the material. The bandwidth, often called linewidth, of this spectrum, which is typically measured at the full-width half maximum point for these modes, lies in the region of 1-2 nm. By modern standards, the 2 nm wide peak from the FP laser configuration is considered

wide and consequently this type of laser, while seeing use in consumer products such as CD players, it is not suitable for demanding telecommunication applications. In fact, for use in dense wavelength division multiplexing schemes, modern lasers operating in the 1500 nm low loss window, a much narrower linewidths of about 10 MHz is common.

### 1.2.3 Single Frequency Lasers

Different methods have been investigated to reduce the linewidth of lasers and obtain single frequency operation. The most significant includes the distributed-feedback (DFB) arrangement, distributed-Bragg reflector (DBR) arrangement, the cleaved-coupled cavity ( $C^3$ ), and the external wavelength selective feedback method. Figure 1.2 demonstrates the basic elements for each of these methods.

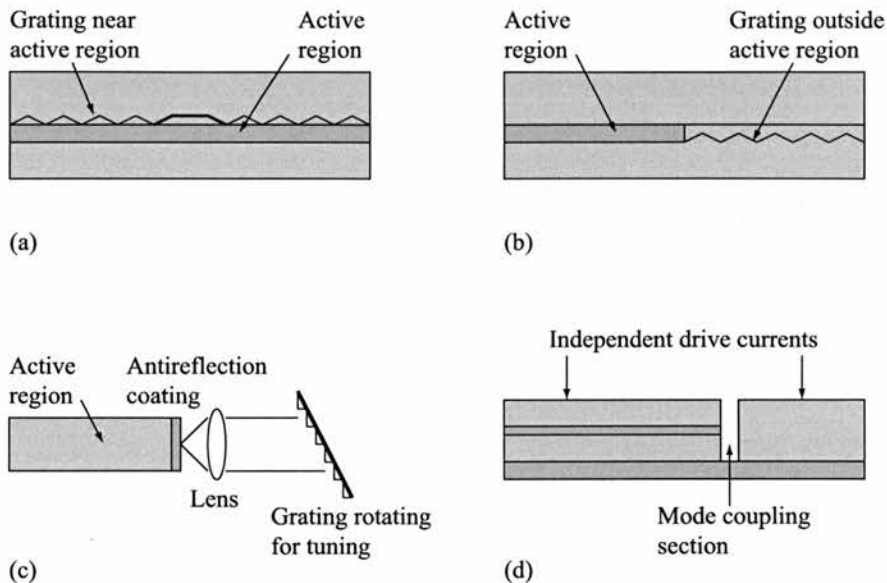


**Figure 1.2:** Single-frequency semiconductor lasers following four principle designs: (a) DFB, a grating replaces two mirrors of the cavity to provide feedback; (b) DBR, the cavity mirrors consist of one grating on the semiconductor outside the active region and a cleaved facet; (c) external cavity laser; and (d) cleaved coupled-cavity laser.

### Distributed Feedback (DFB) Laser

Proposed in the early 1970's, today's DFB lasers are used in almost all installed optical networks. In general, multiple quantum well (MQW) DFB ridge waveguide structures are created in two growth steps. A base structure is grown first, which includes the MQW active region, an etch-stop layer and the grating layer. First-order Bragg gratings are fabricated in the grating layer by using a holographic photolithographic process in conjunction with conventional reactive ion etching (RIE) techniques. After defining the grating close to the epitaxial structure, the wafer is returned to the growth chamber for the second growth step. In this second step, the laser structure growth is completed by growing the cladding layer over the grating layer followed by the upper contact layers.

The grating position and corresponding tooth height are designed to produce a product  $\kappa L \approx 1$ , where  $\kappa$  is the grating coupling coefficient and  $L$  is the cavity length. Lateral mode confinement is provided by a dual-channel ridge waveguide (RWG) structure. Single-mode operation for lasers with a specific ridge width can be maintained by accurate control of the channel etch depth utilising the grown-in etch-stop layer in the laser structure.

The principle behind the DFB configuration is the effective replacement of the FP cavity facets as reflectors. The wavelength at which the feedback occurs is strictly controlled by the grating periodicity and its coupling coefficient. The distribution of the incremental reflection along the length of the laser in this manner acts to significantly reduce the number of longitudinal modes which can be sustained by the cavity, effectively reducing the overall linewidth of the laser output.

The operational wavelength of the laser is defined by the introduction of a  $\lambda/4$  phase-shift defect. This creates a laser cavity between the DFB mirrors. The resonance of this cavity permits laser operation at this wavelength.

### Distributed Bragg Reflector Laser

In a similar fashion to the DFB laser configuration, the DBR laser (Figure 1.2 (b)) utilises a Bragg grating. The significant difference being that the

grating is not integrated onto the surface of the laser, but placed outside of the active region. This greatly simplifies the epitaxial growth procedure used to bury the heterostructure. Variations on the general layout include devices incorporating two gratings, replacing both facet reflectors. Similarly, the operational wavelength of the device is determined by the period of the grating(s).

Variations of this laser configuration known as the sampled grating (SG) DBR and superstructure grating (SSG) DBR lasers exist. These devices are discussed in more detail in the proceeding Section 1.3 on tunability in lasers.

### External Cavity Laser

In the external cavity laser (ECL) configuration (Figure 1.2 (c)) a wavelength selective filtering element, usually a grating, takes the role of the second reflector [11]. Anti-reflection coatings are utilised on the internal facet of the laser diode and traditional bulk optic elements employed in the arrangement for beam capture and collimation. Single frequency operation of the ECL is achieved by the spectral filtering effect of the grating, while the wavelength of operation can be dictated, within the boundaries of the material gain spectra, by rotating the grating such that only a specific wavelength is coupled back into the laser cavity.

### Coupled Cavity Laser

Single longitudinal frequency selection in the coupled cavity laser arrangement is due to the coincidence of the individual resonances of the two cavities that make up the device. In most cases, the cavity lengths differ by a relatively small fraction. The effect of this length difference on the mode spacing of the individual cavities and the overall operating wavelength of the device is summarised in Figure 1.3.

From Figure 1.2 (d) the front or longer cavity possesses a longer optical path, where the spacing between resonant modes is smaller. The regular spacing of the resonant frequencies forms a comb-like function of resonant wavelengths. The second, shorter cavity demonstrates an increase in the modal

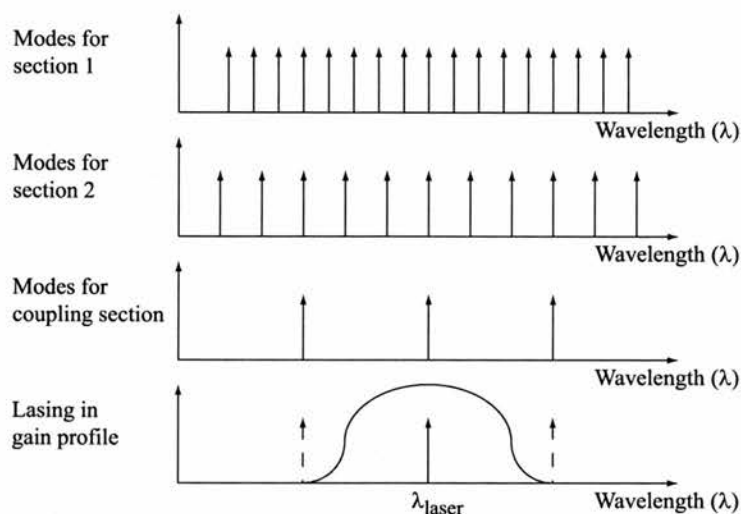


**Figure 1.3:** Spectra indicating resonant peaks for the different cavity lengths. Graphs a) and b) represent the resonances of the longer and shorter cavities of the device. Graph c) represents the resonance conditions for the intercavity reflector. The material gain profile d) provides an envelope under which the tuning range is confined.

spacing of the comb. Figure 1.3 presents representative spectra for these cavities. The two cavities are separated by a gap, which itself adds a spectral filtering effect. The wavelength of operation for the composite device is essentially the coincidence wavelength of all the cavities involved in the selection.

### Vertical Cavity Surface Emission Laser

The vertical cavity surface emitting laser (VCSEL) is the chief alternative to edge-emission devices. In its construction, the VCSEL differs from the lasers previously described in that the reflectors and cavity lie in the plane of the semiconductor substrate. The configuration of a typical VCSEL is illustrated in Figure 1.4

A VCSEL emits light in a direction perpendicular to the semiconductor wafer. This one property accounts for a vast simplification in VCSEL manufacture. Compared with that of edge emitters, the cavity of a VCSEL is complete, requiring no cleaving of facets or any other mechanical intrusion

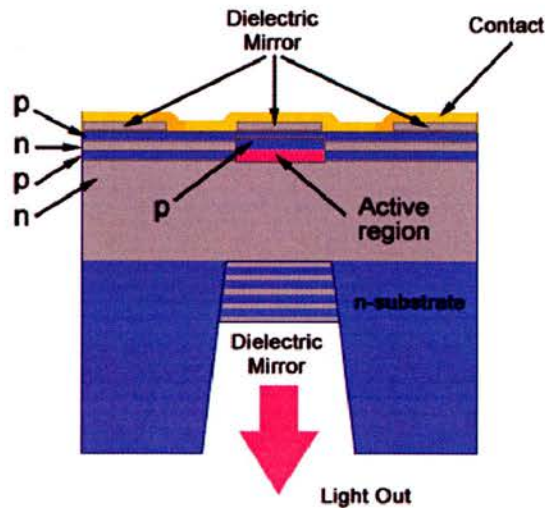


**Figure 1.4:** Typically, most VCSEL devices employ quantum wells within the cavity. In doing so, control of recombination and optical properties of the laser can be achieved. The schematic shown is a specific example of an Etched Well VCSEL. Figure courtesy of [12]

into the device. Most VCSEL devices employ quantum wells within the cavity. By depositing a thin layer of semiconductor with a slightly smaller band gap, one can not only define a region for the recombination of carriers to occur, but also tailor the optical properties of the device.

Due to the shortness of the cavity length, typically 1-3 wavelengths of the emitted light, a single pass of the cavity, provides a photon with little chance of triggering a stimulated emission event at low carrier densities. For this reason, highly reflective mirrors are required for efficient VCSELs operation. In edge-emitting lasers, a reflectivity coefficient of about 30 % can be expected at the facet. For VCSELs requiring low threshold currents, facet reflectivities greater than 99.9 % are required, and the use of distributed Bragg reflectors (DBR) are deemed the obvious choice. The distributed Bragg reflectors are formed by depositing alternating layers of dielectric materials with a difference in refractive index.

### 1.2.4 Tunable Laser Technologies

A variety of methods have been developed in an effort to obtain tunability from semiconductor lasers. These methods, while offering different ranges of tunability, are in the main based upon or adapted from the methods already described for obtaining single frequency laser operation. The technologies can be loosely classified into four different categories. The external cavity laser (ECL), the vertical cavity surface emitting laser (VCSEL), DFB and DBR grating based laser configurations. Of these, only the later three have proven successful candidates for monolithic integration, while devices based on the ECL approach have been realised as a packaged component [13].

#### External Cavity Tuning Approach

The first approach to be considered is the adaptation of the external cavity laser technology presented in Section 1.2.3. This technology is widely used to provide tunable lasers for test and measurement applications. Wide tuning ranges with high output power and good optical properties (SMSR, RIN, narrow linewidth) have been demonstrated for a long time by ECL [14]. Three fundamental drawbacks exist with this configuration. The first is the physical size of the elements involved in its construction and operation. The second drawback is the speed at which the tuning can occur. Being a mechanical mechanism its operation is slow in comparison to other technologies. The third consideration relates to the tuning mechanism. As previously described, the tuning mechanism in an ECL laser involves the rotation/translation of a dispersive element in the cavity [15]. The existence of moving parts bring into question the long-term reliability of this technology.

Attempts to address the the possibility of mechanical instabilities have led to the development of electronically tunable external cavity laser diodes (ETECAL) [16, 17]. The configuration of the ETECAL is shown in Figure 1.5. The introduction of collimating optics (represented by lens 2 in the Figure) and a liquid crystal array (LCA) into the path of the beam in front of what was traditionally the retro-reflector permits the selection of specific spatial components of the spectral output from the laser diode. The tuning rate of lasers based

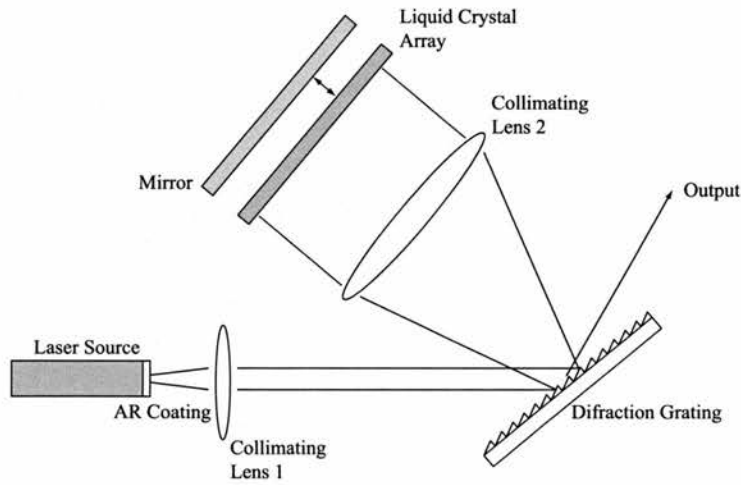


**Figure 1.5:** Schematic of the ETECAL setup. Elements in the liquid crystal array are modulated allowing only specific wavelengths to be fed back into the cavity.

on this arrangement is limited by the speed of the LCA, typically this speed lies in the range of a few megahertz. Substitution of the LCA with semiconductor based electroabsorption modulators (EAM) permit switching rates in the megahertz range [18, 19]. Operation of this configuration has also demonstrated synchronous dual wavelength emission operation [20]. Time-resolved emission measurements have demonstrated simultaneous dual-mode emission [21], offering the ETECEL configuration as a viable source for pump-probe spectroscopy and difference-frequency generation in the terahertz regime. The elimination of any mechanical parts alleviates inherent instabilities in this laser configuration.

In an alternative approach, the construction of an ‘intra-cavity liquid crystal pixel mirror’ has demonstrated digital single-longitudinal mode tuning [22]. 40 channels at a spacing of 100 GHz displaying side mode suppression ratios in excess of 30 dB were measured.

Io $\lambda$ on<sup>3</sup> have employed a silicon based micro-electro-mechanical system (MEMS) approach to reduce overall size of the external cavity arrangement [24]. A

<sup>3</sup>Io $\lambda$ on have used balanced MEMS electrostatic rotary actuators to create a 20 mW external cavity diode laser capable of addressing ITU C- or L-band channels over 37 nm, maintaining  $\pm 1.25$  GHz frequency stability and 55 dB side-mode suppression.

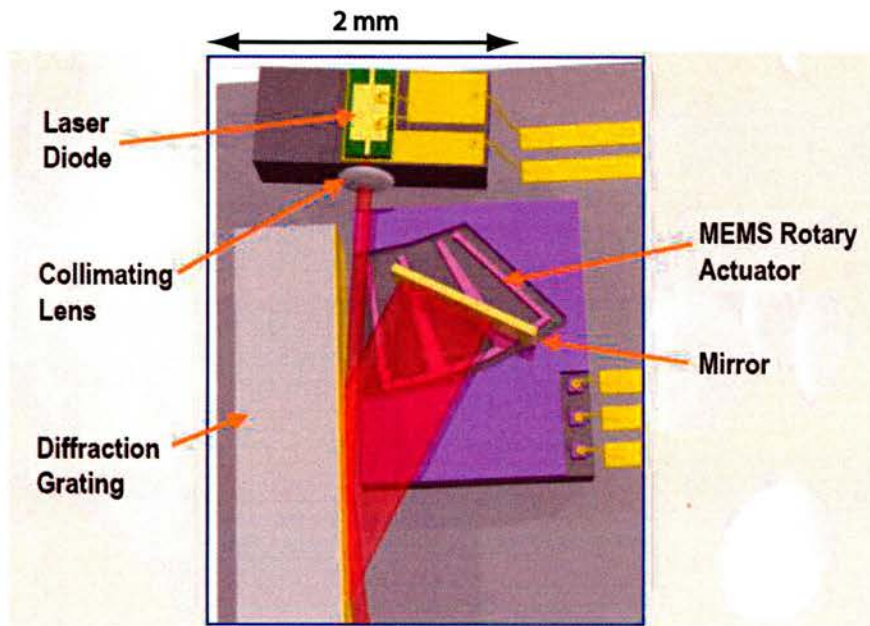


**Figure 1.6:** Miniaturisation of the classical Littman external cavity laser configuration. Courtesy of  $\text{io}\lambda\text{on}$  [23]. The complete device measures approximately 2 mm by 4 mm.

schematic of the Littman external cavity based device [25] is presented in Figure 1.6. Wavelength tuning is achieved by rotating a mirror using an electrostatic comb drive. Typically voltages up to 140 V are required to drive this comb element. The mechanical nature of the tuning mechanism means that the tuning times lie in the region of 15 ms. Being based on the external cavity configuration, the instantaneous linewidth is less than 1 MHz with a side mode suppression ratio greater than 50 dB. The rotary actuator enables full C-band continuous tuning with 50 GHz channel spacing.

### Tunable VSCEL Laser

The adaptation of the VCSEL laser configuration to obtaining tunability depends predominantly on the use of MEMs. In [26] a deformable upper curved DBR reflector [27] was used to demonstrate continuous tuning over a range of 44 nm. This single mode operation, displaying a side mode suppression ratio

greater than 25 dB, was achieved by applying an electrostatic voltage swing of 14 Volts.

### Tuning of DFB Lasers

Temperature can be used to tune the emission wavelength of a DFB laser cavity. Two approaches may be used to change the cavity resonances. The first, and possibly the simplest, arrangement for tuning a semiconductor laser is to combine a thermal electric cooler (TEC) or thin film heating element with the DFB laser structure. Thermal tuning of DFB laser cavities in this manner offers a tuning range limited to around 8 nm. Although a thermal tuning range of 13 nm has been reported using a tunable twin-guide (TTG) DFB laser structure [28].

Two major drawbacks with using temperature as a tuning method are a) tuning the device in this fashion reveals a slow tuning rate, which precludes these devices from many applications requiring rapid switching times and b) the subsequent loss in efficiency of the DFB laser at high temperatures, often referred to as ‘thermal rollover’, limits the effective range for which tuning can be accessed. For a) thermal conductivity limits the tuning rate, by using temperature achievable tuning ranges from 1.9 nm in 10 min [29] for moderately sized temperature controlling devices, up to 0.3 nm in 250  $\mu$ s from methods involving joule heating by the modulation of the injection current to the active region [30]. Recently the gap between tuning range and tuning rate has been bridged using a VCSEL structure [31]. In [32] devices capable of achieving a tuning range of 2 nm in 50  $\mu$ s have been reported. In [33, 34] rapid thermal (RT) tuning of a standard DFB diode laser using a pulsed auxiliary 2.7 W 532 nm laser beam in conjunction with a small thermal mass TEC element has demonstrated 4 nm tuning range (10-fold increase over previously reported ranges) for a temperature range of 60 °C (from -10 to +50 °C) cycled at kilohertz rates.

Extended tunability using DFB lasers is achieved by employing arrays of these lasers integrated either monolithically [35] or on a hybrid planar light-wave circuit (PLC) [36]. Each laser differs slightly in its design and operate at

different wavelengths. In [37] the fabrication of 40 different wavelength DFB lasers has been reported. This DFB laser array integrated with power combiners enables the addressing of a total tuning range of 75 nm from 1,518.2 to 1,593.2 nm [38]. In compensating for inadequate laser output power, integration of semiconductor optical amplifiers (SOA) has been achieved [39]. While the use of SOA with DFB laser arrays offers a solution to the problem, progress made in the fabrication of antireflection coatings now allow for reflectivities on the order of  $10^{-5}$ . This warrants weak optical feedback from the SOA and recent studies have suggested [40] that the monolithic integration of a SOA with a DFB laser could degrade the side mode suppression ratio from -45 dB to -10 dB.

### Grating Based Laser

As previously indicated, the cavity of the DBR laser is defined by the use of distributed Bragg gratings. The tuning of the DBR laser may occur either by the same thermal effects used to tune the DFB laser or tuning may result from the 'plasma' effect. The 'plasma' effect is a change of refractive index experienced by a semiconductor when it is exposed to the direct injection of electrical current.

Tuning the resonances of DBR structures using current injection has been reported for a considerable time [41]. The development of mirror tuning has given rise to several subclasses of grating based lasers, most notably the sampled grating (SG) distributed Bragg reflector [42, 43] and the super structure grating (SSG) distributed Bragg reflector [44, 45, 46, 47] laser configurations.

While technologically the same as other DBR lasers, the SG- and SSG-DBR lasers have demonstrated enhanced tuning ranges and reasonable side mode suppression ratios. Recent reports [48, 49, 50, 51] demonstrate tuning ranges in the region of around 30 nm and over 100 nm for the SG- and SSG-DBR lasers respectively.

### Sampled Grating DBR Laser

The sampled grating laser structure differs from the standard DBR laser in that the periodic variation in refractive index which constitutes the distributed reflector does not occupy the complete length of the mirror section. Instead the reflector is formed by small discontinuous elements of the complete Bragg structure as demonstrated in Figure 1.7. By injecting current in the distributed Bragg reflector, the laser's emission wavelength can be selected.

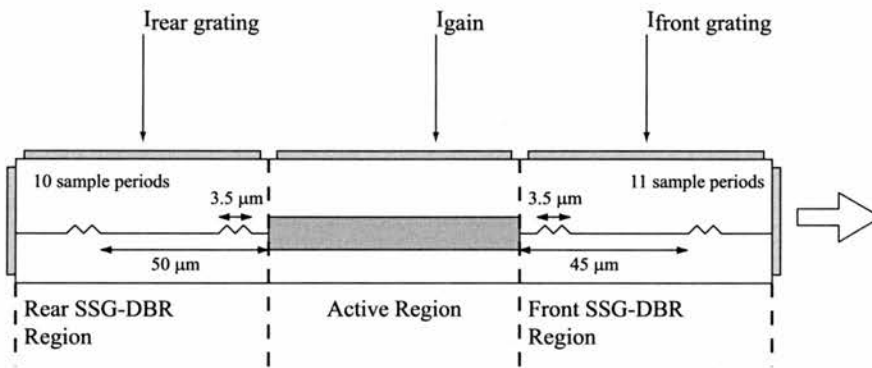


**Figure 1.7:** Typical three section sampled grating DBR laser with two dissimilar gratings. Antireflection coatings on the cavity facets are often employed.

Typically only 10 % of the grating sample period contains the Bragg elements in an SG-DBR laser structure. This leads to a relatively low power reflectivity from the grating, while the reflectivity drops off rapidly away from the Bragg wavelength. The sampled grating distributed Bragg reflector laser was the first [47] monolithic device to ever tune over a wavelength range of 30 nm, albeit with a side mode suppression ratio  $< 25$  dB.

The sampled grating design uses two different multielement mirrors to create two reflection combs with different wavelength spacings. The laser operates at a wavelength where a reflection peak from each mirror coincide. Since the peak spacings are different only one pair of peaks can line up at a time. The peak spacing is generally chosen to be a little less than the available direct index tuning range i.e. between 6-8 nm so that the range between peaks can be accessed by tuning both mirrors together. By tuning the mirrors relative to

each other, termed differential tuning or vernier tuning, an enhancement in the tuning can be achieved. Since the distance between each mirror resonances is much less than the resonance spacing of either mirror, only a small amount of differential tuning is required to line-up adjacent reflection peaks. Combining ‘equal’ and ‘differential’ tuning permits coverage over the full desired tuning range.

### Superstructure-Grating DBR Laser

Most of the features of the SGDBR are shared by the superstructure-grating DBR (SSGDBR) design shown in Figure 1.7. The super structure grating differs in as much as the desired multiple-peaked reflection spectrum of each mirror is created by using a phase modulation of the grating rather than an amplitude modulation function as in the SGDBR. Periodic bursts of a grating with a chirped period are typically used.

The gratings are designed along the same principle as those for the sampled grating device and merged with several another sampled grating of a different spacing, forming a superstructure grating. This provides the advantage that the reflection peaks obtained from these gratings are more uniform, hence reducing the output power variations during tuning

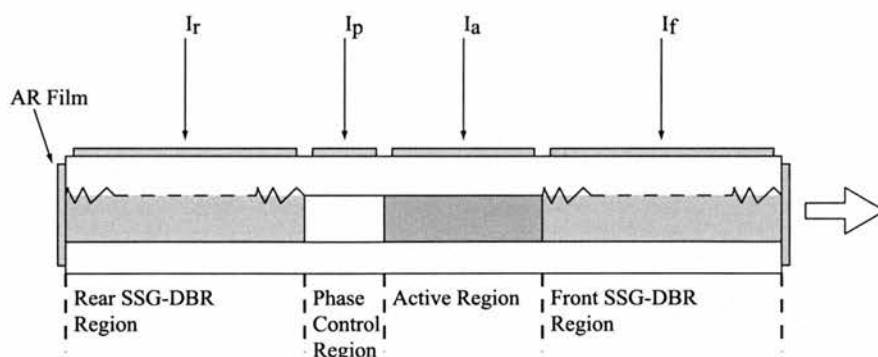


**Figure 1.8:** Example of a four section superstructure grating DBR laser. Slightly different gratings simultaneously occupy a larger proportion of the mirror regions, hence the optical output is somewhat reduced.

The formation of this grating is very complex, and typically requires direct

E-beam exposure. Because the grating exists throughout the mirror, the carrier lifetimes in the mirror regions tends to be lower than in the SGDBR, in which 90 % of the mirror region contains no grating.

### 1.3 Applications for Tunable Lasers

There are many applications for wavelength agile sources in the form of tunable lasers. Wherever one currently finds a single fixed frequency source, the application may be enhanced and extra functionality incorporated if the fixed wavelength source is exchanged for a tunable source. The most commonly discussed applications are those pertaining to the communications industry. Wavelength agile sources can also play a significant role in conducting spectrometric measurements in difficult or harsh environments.

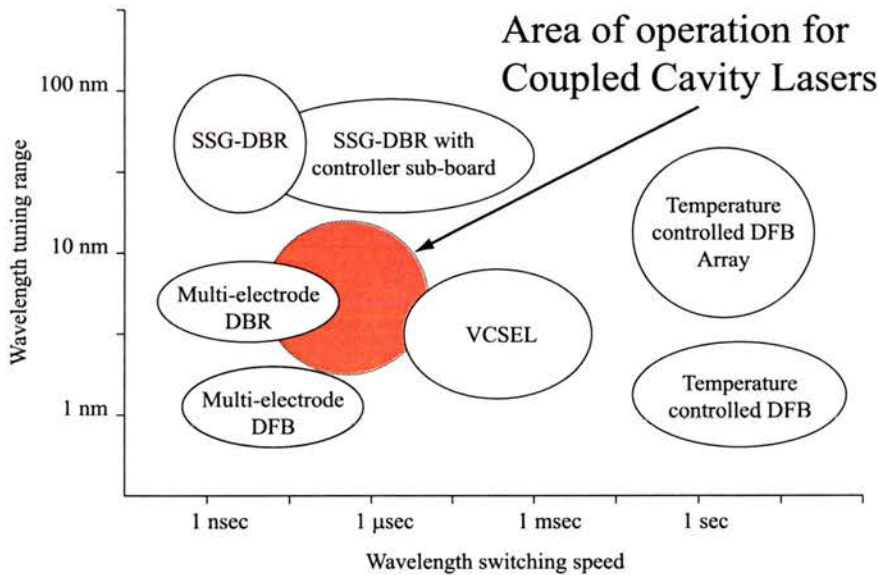


**Figure 1.9:** Graph of the mainstream technologies and relative positions with respect to tuning range and tuning speed.

Figure 1.9 demonstrates the relative operating regimes of the main tuning mechanisms in terms of typical device tuning range and tuning speed. Clearly, for applications requiring devices capable of high speed operating

multi-electrode DBR and DFB lasers are an optimal choice. Greater tuning ranges can also be achieved by using a super-structure grating DBR laser solution.

### 1.3.1 Optical Communications Systems

After an abrupt stop in the development of wavelength agile sources primarily due to a drop in expenditure of research funding bodies, research into the sources has started to gain momentum. Although still enjoying an 80 to 100 % growth rate per annum<sup>4</sup>, the killer applications of dynamic networks and wavelength reconfigurability have given way to the more mundane potential for reduced operational overheads through inventory reduction and system redundancy. Here the development of WDM and DWDM systems are discussed.

#### Fixed wavelength Systems

The key components for any communications system are the transceiver and receiver, the medium over which transmission is to occur and finally the information to be sent. Figure 1.10 demonstrates this generic communications system. For optical communications, the simplest case is that of a fixed wavelength system where a single laser is modulated and the resulting light pulse train is transmitted using an optical fibre as the medium. Optical fibres can transmit light at much higher speeds than individual lasers can be modulated. Typically the optical pulse source generates an optical pulse train with a 2.5 Gbit/s repetition rate.

#### System Limitation

The cost effectiveness for the providers of services based on optical communication systems is based on the price chargeable per information-mile. In order to optimise and improve on this value, three methods exist for enhancing the system's capacity. The first is to increase the number of optical fibers; a very expensive option when one considers that a majority of fibres are installed

---

<sup>4</sup>Article: The Economic Times, 'Global bandwidth demand to double' Monday, February 14, 2005

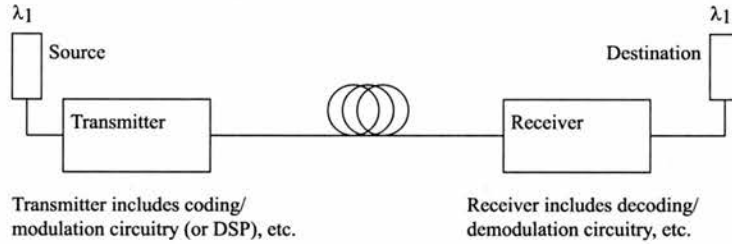


**Figure 1.10:** Fundamental elements making up a typical communication link.

in a subterranean environment, while the second is to increasing the overall speed of operation or data rate of the entire system, essentially pushing more information through the channel for any unit of time. The bandwidth of an optical fiber determines the amount of information that can be supported. The mechanism that limits a fibers bandwidth is known as dispersion. Typically a dispersion parameter value of  $D = 17 \text{ ps/Km} - \text{nm}$  is defined for single mode fibers operating at  $1.5 \mu\text{m}$ .

Dispersion manifests itself by spreading the optical pulses as they travel down the fiber. The result is that pulses then begin to spread into one another and the pulse train becomes indistinguishable. The limit on transmission distance is described by Equation 1.1 [52]

$$B^2 L < 16 \frac{\lambda^2 D}{2\pi c} \quad \text{OR} \quad L < \frac{16\lambda^2 D}{B^2 2\pi c} \quad (1.1)$$

where  $B$  is the bandwidth,  $L$  is the length of the fiber,  $c$  is the speed of light in the fiber and  $\lambda$  is the wavelength of operation. Therefore, the relationship between the bandwidth and the channel length is given by Equation 1.2

$$L < KB^2 \quad (1.2)$$

where  $K$  is a constant; therefore, as  $B$  increases,  $L$  decreases with the square root of  $B$ . Clearly, the higher the value of the dispersion the greater its limitation on the system performance.

The third method for increasing the cost effectiveness over a single channel is to employ a Wavelength Division Multiplexing (WDM) scheme. Multiplex-

ing  $N$  optical signals operating at different wavelengths over a single medium effectively enables the transmission of  $N$ -channels simultaneously. The adaptation of currently in-situ system in such a fashion proves to be a far more cost-effective means of increasing the transmission capacity of metropolitan area networks.

### Wavelength Division Multiplexing

Silica or glass based optical fibers are known to possess low attenuation “optical windows” centered around 1300 nm and 1550 nm wavelength ranges. These low loss windows measure approximately 18,000 GHz and 12,000 GHz respectively, offering a potential total of 30,000 GHz of available bandwidth in each fiber. The loss experienced by light propagating in these windows is around 0.5 dB/km and 0.4 dB/km for the windows around 1.3  $\mu\text{m}$  and 1.55  $\mu\text{m}$  respectively. Between these two windows there is a spike in the attenuation at 1.39  $\mu\text{m}$ . Increasing the capacity of the system can, as explained above, be achieved by using multiple wavelength channels, i.e. using the wavelength division multiplexing technique.

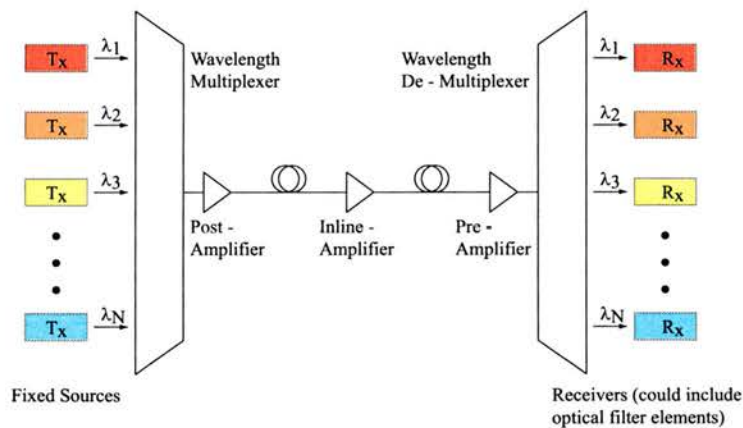


**Figure 1.11:** Schematic of a basic wavelength division multiplexing communication system. A set of  $N$  fixed sources of different wavelengths provide the input to the system, while combined filters and detectors form the output receiver array.

Figure 1.11 outlines the basic components required for the multiplexing

of several signal onto a common communications channel. There are a number of multiplexing technologies available with different cost and performance profiles. The main options include: integrated optics arrayed waveguide gratings (AWG), fiber Bragg gratings (FBG) and cascaded Mach-Zehnder based devices. Optical attenuation, material dispersion and channel cross-talk all act on the signals to during transmission to deteriorate successful signal recovery. To some extent the choice of adequate channel spacing reduces these effects. The International Telecommunication Union (ITU) proposes standardised frequency grid for determination of the channel spacing. WDM systems comprising 32, 64 and 128 different wavelengths spaced with a 100, 50 and 25 GHz grid have been demonstrated.

### **Channel Sparing and Inventory Reduction**

The introduction of tunable lasers to WDM systems permits operators to maintain the overall transmission capacity, by incorporating tunable lasers in the communication system, one can build in channel redundancy, in the event of a laser failure the channel containing the tunable source may take over the load. This scenario, depicted in Figure 1.12, although simplistic in it's approach will require that the tunable laser perform to (if not better than) the specifications of the DFB laser it is intended to replace. The aspects of power, spurious mode suppression, wavelength stability and lifetime over the entire wavelength range must be addressed.

The second benefit of using tunable lasers in conjunction with WDM systems is through opportunistic operating savings. With a WDM system utilising fixed wavelength lasers, each wavelength used requires manufacturing a tailored laser and an associated line-card. The resulting inventory requirements for a system runs to many tens of different wavelengths.

The financial burden of maintaining such an inventory can be reduced with the introduction of a tunable source. With an appropriate line card, a single or a handful tunable lasers may take the place of dozens of inventoried devices. Replacement of failing devices would require only the extra stage of setting up the operating wavelength before installation.

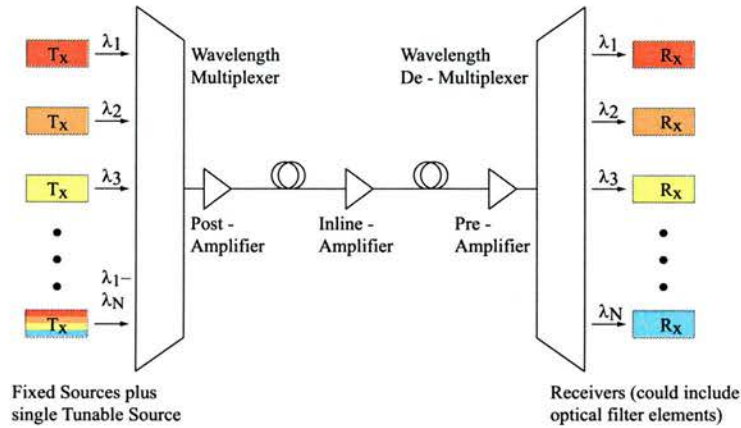


**Figure 1.12:** Schematic of a wavelength division multiplexing communication system incorporating a single Tunable Source.

The temperature change induces a change in the cavity's optical path length (with the degree of change dependent on cavity material), which could also produce unacceptable changes in the optical characteristics of the subsystem. At present, the available option for an etalon with extremely low thermal drift is the gas (usually air or nitrogen) cavity etalon

### Uncooled and fixed $\lambda$ laser

The stringent requirements for frequency stability in dense wavelength division multiplexing (DWDM) systems has brought about a demand for passive optical telecommunications components with display a high thermal stability. The key requirements for any proposed tunable source is therefore market driven. The creation of a source which can be repeatedly tuned over significant range and display long term temperature independence with respect to both device aging and through thermal drift is highly desirable from an network operators stance. One important application for a simple, reliable source is an uncooled fixed wavelength laser system. The main component common to these systems is the etalon, which induces multiple beam interference between two reflecting surfaces. Practically the etalons are either based on the Fabry-Perot or Gires-Tournois configurations. The etalons find use as subcomponents in wavelength

filters (tunable and fixed), laser wavelength lockers, interleavers and chromatic dispersion compensators.

Such optical subassemblies typically operate in environments with thermal variations of several tens of degrees Celsius, which can result from ambient temperature fluctuations or thermal contact between the etalon and a device such as a thermally tunable laser diode. A uncooled fixed  $\lambda$  source would therefore be a ideal solution to these problems.

### 1.3.2 Optical Networking

While employing tunable lasers in the roles of channel sparing and inventory reduction, are certainly important, the real “killer applications” for widely tunable lasers lie with their use in optical networks. The need for high bandwidth in today and tomorrow’s IP-based internet, and the promise of WDM to provide this high capacity, (while stunted by the market conditions of a few years ago,) have prompted the need for IP-over-WDM networks.

Hailed as the next step in the development of network architectures, the upgrading of communication systems from using conventional connection-orientated or circuit-switched networks to photonic packet-switched data networks will be a key requirement. Photonic packet switching appears to be a strong candidate because of the high speed, data rate/format transparency, and configurability it offers. The concept of wavelength division multiplexing provides the opportunity for multiplying the available network capacity. Adopting an optical approach to the problem of bandwidth shortage is a swift response. The optical wavelength based infrastructure provides only the ‘raw capacity’ in solving the problem, the maintenance and operations of the bandwidth still requires the implementation of all optical devices.

#### Optical Packet-Switching

One challenge to optical networking is how to switch light signals. When a signal arrives at its destination, it must be separated from the rest of the channels. To drop one signal at an intermediate point, an optical filter separates the proper wavelength from the rest. Equipment at that point may also add

a new signal to the now unoccupied wavelength.

Optical switches may operate on a single wavelength, or on all the wavelengths transmitted through a fiber. A fixed filter, like the one described above, could be replaced by a switch that selects one of several filters to divert the desired wavelength to the intermediate point. A third kind of switch separates the wavelengths into separate beams, and a moving mirror directs one or more of the wavelengths in a different direction. Other optical switches simultaneously switch all wavelengths passing through a fiber; one example is a mirror at the fiber output that could tilt between two different positions to reroute all optical channels in case of a fiber break.

The examples listed thus far are loosely termed "all-optical" switches because they operate on light signals. A different class of switches convert optical signals into an electronic form which can be switched electronically; the resulting electronic signal then feeds into an optical transmitter to generate a new optical signal. These are known as opto-electro-optical (OEO) switches, emphasising that the switching 'fabric' is based on electronics.

As switching technology continues to develop, all optical networks will be required to convert signals operating at one wavelength to a different wavelength. This reconfigurability of a network is currently achieved using the opto-electro-optical wavelength converters (that convert the input optical signal into electronic form to drive a transmitter at the second wavelength). All-optical wavelength converters, where the switching 'fabric' operates in the optical domain, have been demonstrated in the laboratory, but at this time have not seen use in practical systems. Laser sources that can address the many different wavelengths also will be needed; several types have been demonstrated, while commercialisation of a few has been achieved[53].

## **Optical Routing**

As telecommunications and computer networking continue to converge, data traffic has gradually exceeded voice traffic [54]. This means that many of the existing connection-oriented or circuit-switched networks will need to be upgraded to support packet-switched data traffic. Two types of optical wave-

length switches will be available, optical-electrical-optical (OEO) switches and all-optical, optical-optical-optical (OOO) switches. The decision of which switch to deploy is purely a commercial one. Therefore the use of all optical networking and switching to support the new multimedia applications seems inevitable.

Signal contention has a great impact on network performance in terms of packet-loss ratio, packet delivery delay and average hop distance and ultimately network throughput. In an optical WDM packet-switched network a combination of wavelength conversion (wavelength reassignment), path deflection (route reassignment) and optical delays-lines (optical storage) may be employed in order to resolve the contention.

Each of the above schemes has its own advantages and disadvantages: wavelength conversion is very efficient and able to resolve contention without introducing extra delay to the packet, but the expense of implementing full-range wavelength conversion is prohibitive and none are available today. Path deflection has the lowest cost since it shifts the burden of resolving contention to the whole network while lowering network overall throughput. Optical delay-lines (time buffering) has medium cost. It might introduce nonnegligible delay to the packet, depending on the packet length. The first choice (wavelength conversion) achieves the same propagation delay and number of hops as the optimal case, and eliminates the difficulties in sequencing multiple packets. From this perspective, wavelength conversion is a very attractive solution compared to path deflection or time-buffering.

The viability of efficient wavelength routing of signals across a wide area optical network (WAoN) depends upon the availability of adequate wavelength agile sources.

## 1.4 Aims and Motivation for Work

### Review

The multi-section laser approach to developing tunable lasers has led to the creation of a entire range of wavelength agile sources[55, 56]. The initial dual

cavity device, investigated throughout the 1980's demonstrated the usefulness of the coupled cavity concept as a means of creating a single-mode and wavelength agile source.

From this initial configuration the introduction of a phase 'control' section [57, 58] provided a mechanism for obtaining continuous single mode tuning, at the expense of the increased device complexity and associated electronic controlling circuitry. The incorporation of the phase-shift section was an attempt to simultaneously move the mode comb in conjunction with the grating reflector.

Further developments to the two and three cavity devices focused on employing multi-element mirrors and vernier-effect tuning enhancement structures such as grating assisted co-directional couplers. These developments led to the creation of the four section sampled-grating DBR design and eventually the superstructure-grating DBR lasers mentioned briefly in Section 1.2.4.

### **Simplistic Design**

While addressable wavelength ranges have improved and material pairings have been developed to suit the 1.3  $\mu\text{m}$  and 1.55  $\mu\text{m}$  operational windows, one motivation for returning to the coupled-cavity device lies in its simplicity. The wavelength tuning mechanism of the dual cavity device is relatively well understood and the unwarranted need for complex control circuitry and absence of look-up tables offer the use of a set relatively simple design parameters. The key aim of this project with regard to the device design is to determine the feasibility of a obtaining a highly monochromatic laser simply by selecting appropriate cavity length ratios. The range over which tuning can take place and the value of the side mode suppression over this range are also important factors.

### **Material Development**

Material technologies have developed since the fabrication of the first coupled cavity devices. Advances in knowledge pertaining to quality of grown material, the control over the impurities and the understanding of the quantum

structures offer better materials with which to begin fabrication. In addition to the wafer development, the introduction of new materials such as SU-8 and inorganic polymers such as FOx flowable oxide films offer the fabricator the ability to produce useful devices with a relatively quick turn around.

### **Fabrication Advances**

A third motivation for this work is the development of procedures using modern fabrication technology. During the initial conception of coupled cavity devices, the majority of devices were cleaved and remounted before experiments conducted. During the intervening time frame the cost of ownership for high quality electron beam lithographic equipment has fallen, to the extent that the creation of high resolution patterns have become prevalent. In combination with dry etching techniques developed for work in the field of photonic bandgap structures, structures with dimensions smaller than the laser's operational wavelength are routinely fabricated. Passive reflectors capable of matching the Bragg conditions and inter-cavity slots were fabricated and implemented in the designs.

Advances in the fields of fabrication techniques, material technologies in conjunction with the emergence of the WDM market prompted the decision to revisit the subject of multi-section lasers. The key motivation being the creation of a inexpensive tunable source, disposable tunable source, which could exploit the simplicity of design and fabrication techniques available.

# Chapter 2

## Material

### 2.1 Introduction

In this chapter, a brief review of semiconductor physics is presented. Particular emphasis is placed on the material characteristics pertaining to opto-electronic device applications. We begin by describing the creation of the semiconductor junctions and how the doping modifies the material bandgap and lattice parameter. The introduction of quantum sized effects on the density of states through the incorporation of quantum wells is discussed; leading to the description of the gain mechanism. Broad area laser analysis provides the method for characterising the material. We conclude with a discussion on the material design and the process for determining the optimum material structure for a semiconductor laser.

### 2.2 Semiconductor Overview

Materials are usually categorised into conductors, insulators and semiconductors, by their ability to conduct electricity. The resistivity of a material is a measure of how difficult it is for a current to flow. As an approximation semiconductors have a resistivity,  $\rho$  ranging from  $10^{-5}$  to  $10^8$   $\Omega\text{m}$ , while typical resistivity values for metals and insulators lie below and above this range respectively.

The term semiconductor, most commonly associated with the elements Silicon and Germanium, refers to a much larger group of ‘near perfect’ crystalline materials for which the inherent atomic periodicity has a profound influence on the electronic properties of the material and devices produced from the material. The electronic and optical properties of a semiconductor are determined by the band structure, which itself defines the permissible energy levels an electron can reside in the semiconductor.

### 2.2.1 Band Structure

The concept of the energy bands for a specific material is normally explained by the Bohr model. If one considers an atom in complete isolation, electrons pertaining to the atom are only permitted to exist in discrete orbits or energy levels. For the case of two similar atoms isolated from each other, the allowed energy levels associated with each principle quantum number are identical. As these two atoms are brought into close proximity, the doubly degenerate energy level will split into two due to the interaction between the atoms. With  $N$  atoms brought together, the  $N$  discrete energy levels form a closely spaced band of allowable energies. As an example Figure 2.1 is a schematic of the band creation process for lithium ions [59].

As the spacing of the atoms is reduced further to the point where the distance is approximately equivalent to that of the interatomic spacing of the lattice (typically the interatomic spacing  $r_0 \approx 4 - 6 \text{ \AA}$ ), the single band is found to split again, forming two distinct bands. The distribution of electrons amongst these newly formed bands is guided by the fact that the electrons will fill all the permissible states from the lowest available energies upwards. In the event that a particular band becomes completely full, while the next higher allowed band, separated by a forbidden gap, lies completely empty, the material is in principle either an insulator or a semiconductor. It is common to refer to the lower of these two bands as the *Valence band* and the upper as the *Conduction band*. Materials with partially filled conduction or overlapping bands, (i.e. without a bandgap) define a conductor.

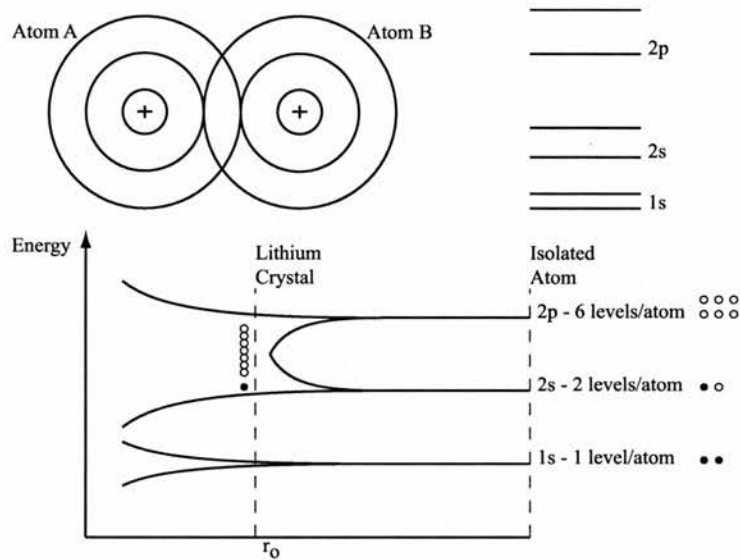


**Figure 2.1:** A schematic of how allowed and forbidden bands form. When the spacing between atoms is large, the allowed levels are discrete. As atoms come closer, the electron energy levels interact with each other forming complicated bands. The deep core levels are relatively unaffected, but the higher levels broaden into bands. Adopted from [60].

The magnitude of the forbidden band or *Bandgap* is typically around 1-2 eV for semiconductors, while values of around 9-12 eV are typical for insulators. Table 2.1 lists the key parameters for some of the most common elemental and compound semiconductors of interest. If the bandgap is sufficiently small, thermal agitation can result in the excitation of electrons from the valence band across the bandgap into the conduction band, leaving vacancies, or holes in the valence band.

### Direct And Indirect Bandgaps

The energy band diagram presented in Figure 2.1 is a simplified representation of a more complex energy band structure. In reality the periodic nature of the nuclei potential acts to modify the energy-momentum relationship of conduction band electrons and valence band holes. This leads to the use of an *effective mass* approach [61, 62], which requires a modified or “effective”

**Table 2.1:** Table of common semiconductor parameters

Material	Band Gap (eV)	Electron Affinity (eV)	Lattice Constant (Å)
Si	1.12	4.01	5.431
Ge	0.66	4.13	5.658
GaAs	1.424	4.07	5.65325
AlAs	2.16	2.62	5.6605
GaP	2.26	4.3	5.45117
InAs	0.36	4.9	6.0585
InP	1.351	4.35	5.86875
ZnSe	2.67	3.9	5.667

mass  $m_n$  and crystal momentum  $\bar{p}^2$  when considering the kinetic energy of an electron in a crystal.

$$E = \frac{p^2}{2m_0} \longrightarrow \frac{\bar{p}_c^2}{2m_n} \quad (2.1)$$

The crystal momentum is analogous to the particle momentum. Figure 2.2 shows the realistic energy band diagrams for both silicon and gallium arsenide. The variation of the bandgap is seen to be different for different direction ([100] and [111]) through the crystal. For silicon, from Figure 2.2(a), the maximum in the valence band occurs at  $\bar{p} = 0$ ; however the minimum in the conduction band occurs along the [100] direction at  $p = \bar{p}_c$ . This situation shows the main difference between the particle momentum and the crystal momentum. The particle momentum for a free electron is zero when the kinetic energy is zero. However, an electron at the conduction band minimum with zero kinetic energy can have a crystal momentum different from zero.

The main implication is that in silicon, for an electron to make a transition from the valence band to the conduction band, requires not only a change in energy ( $\geq E_g$ ) but also a change in the crystal momentum. Silicon is an indirect bandgap semiconductor. For gallium arsenide, Figure 2.2(b), the maximum in the valence band and the minimum in the conduction band occur at the same crystal momentum ( $\bar{p} = 0$ ). Thus, an electron making the transition from the valence to conduction bands requires no change in momentum. GaAs is an example of a direct bandgap semiconductor.

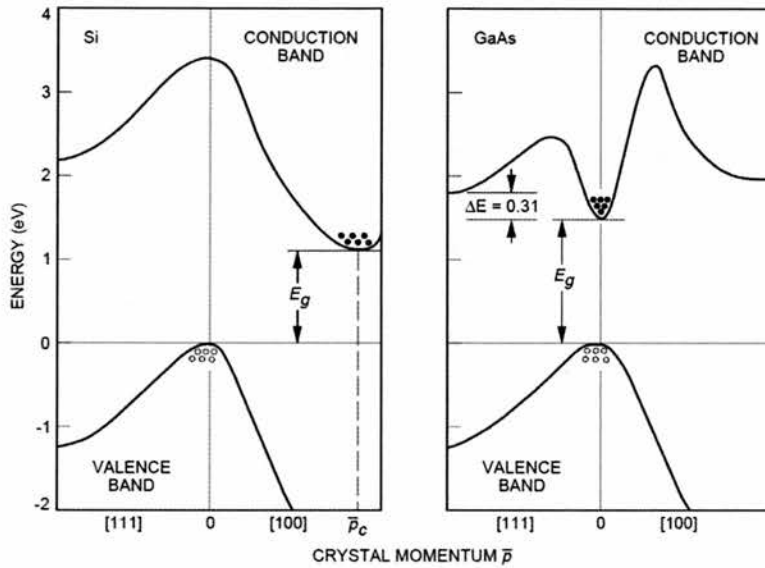


**Figure 2.2:** A schematic of the energy versus wave number real band structures for (a) Silicon and (b) Gallium Arsenide. Courtesy of [63]

This difference between bandgap structures is very important for light emitting diodes and semiconductor lasers. These devices require direct semiconductors for efficient photon generation. The band diagrams presented in Figure 2.2 are somewhat simplistic in their interpretation of the valence band. There is in fact two valence which have a degeneracy at the  $\Gamma$ -point. The preferred nomenclature for these bands is heavy and light hole.

### 2.2.2 Doping Semiconductors

The existence of donor and acceptor impurities in the semiconductor acts to change the electrical characteristics of the material. For a material where donors provide an excess of electrons through thermal ionisation, the nomenclature *n-type* is adopted and for the case of acceptors, the term *p-type* is used to describe an excess of holes. The presence of additional carriers acts to modify the material's electrical characteristics and is demonstrated in the location of the Fermi-level. The Fermi-level is defined as the energy level of

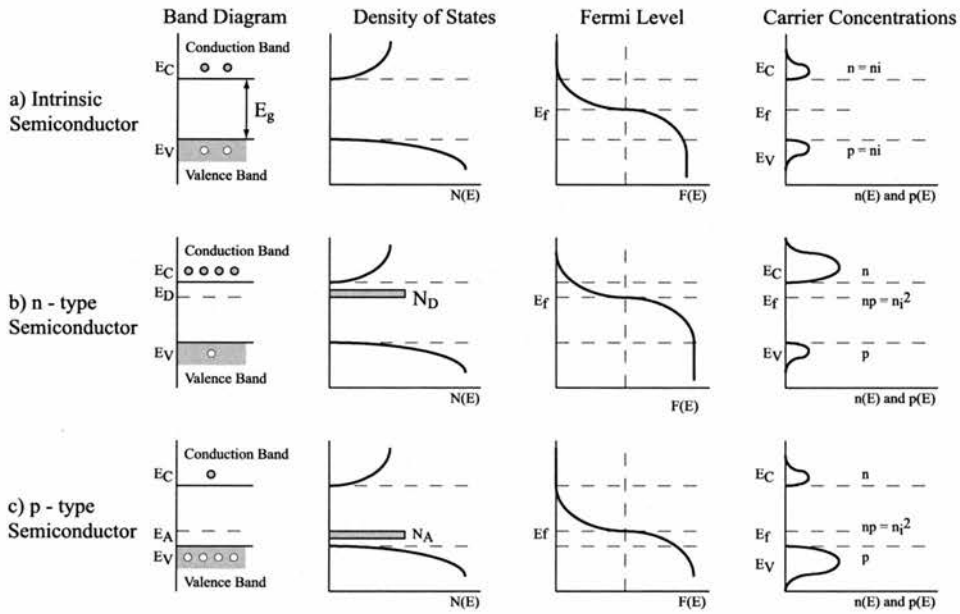


**Figure 2.3:** Schematic of the band diagram, density of states, fermi distribution function and carrier concentration for (a) intrinsic, (b) n-type and (c) p-type semiconductors

a state for which the probability of occupation is exactly one half. In the case of a pure semiconductor the ‘intrinsic’ Fermi energy level lies exactly half way across the bandgap. If the semiconductor is doped, modification of the Fermi energy level occurs. For material doped with acceptor (donor) species, the modified Fermi energy level lies between the valence band top (conduction band bottom) and the dopant energy level. Figure 2.3 demonstrates the location of the Fermi-level and carrier concentrations for intrinsic, n-type and p-type materials.

### 2.2.3 The p-n Junction

A p-n junction is created when adjacent regions of p and n-type material are formed. Traditionally this is described as bringing two sections of oppositely doped bulk material into direct contact, creating an *abrupt* junction, but practically, these junctions are formed using material process techniques such as

epitaxy, diffusion and ion implantation. Typically, acceptor and donor doping levels of between  $10^{17}$  and  $10^{18}$   $\text{cm}^{-3}$  are used in the regions either side of the p-n junction.

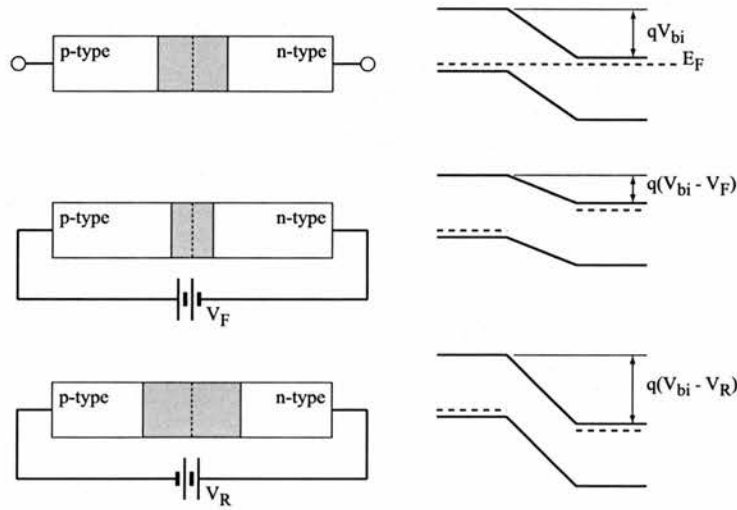


**Figure 2.4:** Schematic of a p-n junction. (a) without an applied bias, (b) under a reverse bias and (c) under a forward bias

## Heterojunction

The first semiconductor lasers were a simple p-n junction formed from the one material, and hence termed a homojunction lasers. The lack of confinement for carriers at the junction led to very low operational efficiency. Superior carrier confinement is achieved using a heterojunction, a junction formed from two dissimilar semiconductor materials. The double heterostructure junction acts to trap carriers at a region the junction. A typical heterostructure junction is formed in the GaAs/AlGaAs material system.

## Bandgap Engineering

For the GaAs/AlGaAs material base it is possible to adjust the compositional fraction of the aluminium during growth. In doing so, this permits the modification of the bandgap belonging to the ternary compound  $\text{Al}_x\text{Ga}_{1-x}\text{As}$ . A

second material characteristic which experiences change as a result of manipulating the aluminium's compositional fraction is the lattice constant. It is important to maintain the lattice mismatch of sequentially grown layers to within acceptable values. During heterostructure growth, a lattice mismatch between the epi-layer and the substrate acts to induce stress or strain into the structure. While the effect of this can in some instances be beneficial to the operation of the device, excessive stress can lead to the creation of dislocations as the structure acts to release the stress. The resulting dislocations act as recombination centers and reduce device efficiency. Figure 2.5 graphically illustrates the lattice constants, the energy gaps for commonly used binary compounds. The figure further demonstrates the dependence of these on compositional fraction for ternary and quaternary compounds.

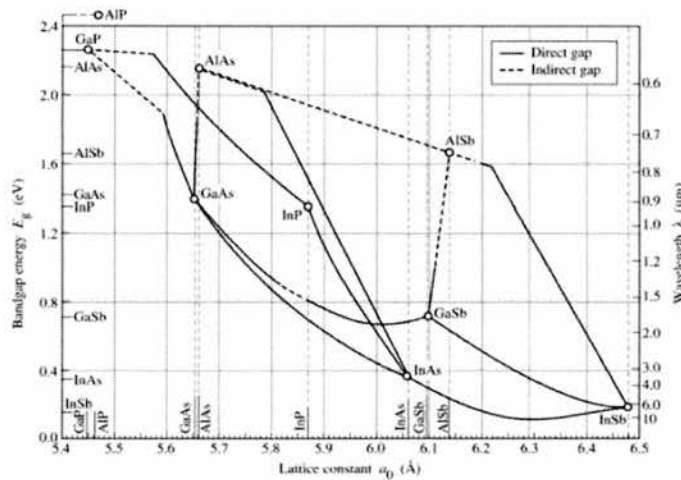
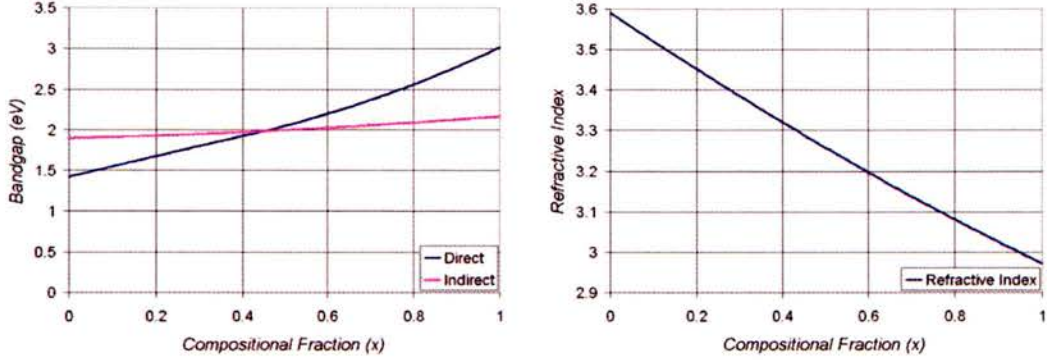


**Figure 2.5:** Lattice constant versus emission wavelength for the most significant semiconductor material bases. Individual binary compounds are represented by single points, while details of ternary compounds are represented by lines connecting the constituent binaries. Solid lines represent the regions where the ternary compounds possess a direct bandgap, while dashed lines indicate indirect bandgaps. Encapsulated areas represent the lattice constant and energies attainable using suitable quaternary alloys. Courtesy of [62]

For the  $\text{Al}_x\text{Ga}_{1-x}\text{As}$  material system, the bandgap variation as a function of Al compositional fraction,  $x$ , follows Equation 2.2 for a compositional frac-



(a) Bandgap for  $\text{Ga}_{1-x}\text{Al}_x\text{As}$  as a function of the compositional fraction (b) Refractive index of  $\text{Ga}_{1-x}\text{Al}_x\text{As}$  as a function of compositional fraction

**Figure 2.6:** Dependence of the bandgap and index of refraction on the fraction,  $x$ , of the aluminium composition. These graphs are plots of the analytical expressions for  $E_g$  and index given by Equations 2.2, 2.3 and 2.4

tion less than 45 % and Equation 2.3 once the compositional fraction becomes greater than 45 % [64].

$$E_g = 1.424 + 1.247x \quad (2.2)$$

$$E_g = 1.985 + 1.147(x - 0.45)^2 \quad (2.3)$$

While GaAs is a direct bandgap semiconductor, AlAs has an indirect bandgap. In a binary compound formed from both GaAs and AlAs, the material  $\text{Al}_x\text{Ga}_{1-x}\text{As}$  experiences a transition from a direct to an indirect bandgap semiconductor when  $x = 0.45$ .

A second material property which varies with compositional fraction is the dielectric constant,  $\epsilon$  for which a linear interpolation between the  $13.1 \epsilon_0$  for GaAs and  $10.1 \epsilon_0$  for AlAs is adopted.

$$\epsilon = (13.1 - 3.0x)\epsilon_0 \quad (2.4)$$

From Equation 2.2, it is obvious that there exists a discontinuity in the bandgap between the GaAs and  $\text{Al}_x\text{Ga}_{1-x}\text{As}$  which establishes a potential

well for carriers on the side of the smaller bandgap material. The refractive index ( $n = \sqrt{\epsilon/\epsilon_0}$ ) discontinuity creates an optical waveguide.

### 2.2.4 Quantum Wells

One of the most important considerations for a semiconductor laser is the number of carriers occupying the available states in the various bands. This is determined by various factors including the pumping rate, the Fermi functions and the density of states. For the case of bulk material, the density of states, often referred to as the 3D density of states, is given as

$$\rho_{c,v}(E)d(E) = \frac{1}{2\pi^2} \left( \frac{2m^*}{\hbar^2} \right)^{3/2} E^{1/2} dE \quad (2.5)$$

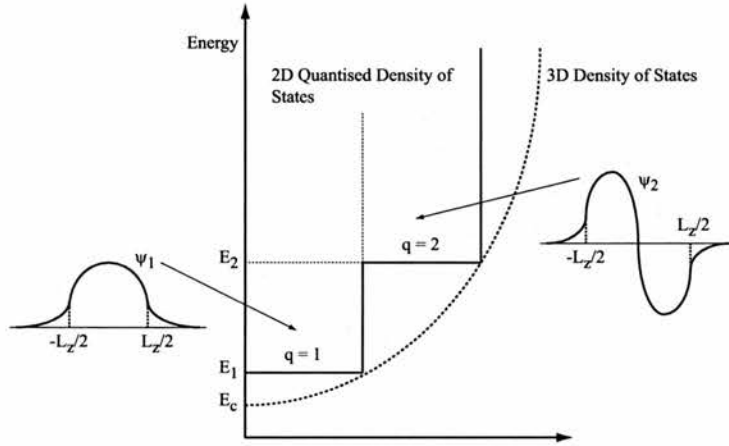
Where  $E$  is measured from the band edge, that is, up into the conduction band or down into the valence band, and  $m^*$  is the effective mass for each of the carriers in these bands. The ability to grow very thin layers ( $L_z \approx 40 - 100 \text{ \AA}$ ) of semiconductor materials has brought about a revolution in lasers. When the layer thicknesses are sufficiently small to be comparable to the de Broglie wavelength, quantum size effects become readily observable. The growing of thin films of different semiconductors on such a small scale allows the creation of artificial materials with tailored device characteristics.

The introduction of ultrathin layers of different semiconductor materials during the growth of heterojunction lasers acts to create abrupt changes which lead to wells being formed in the energy band structure. The quantisation of the density of states in the material growth direction ( $z$  perpendicular to the layer) leads to a modification of the 3D density of states function given in Equation 2.5. The density of states in the quantum well is defined as

$$\rho_{c,v}(E)d(E) = \frac{1}{2\pi^2} \left\{ \frac{2m^*}{\hbar^2} \right\} dE \quad (2.6)$$

This modified density of states is constant, independent of energy, provided  $E$  is larger than the first allowed energy state  $E_1$ , which in turn must be larger than the normal band edge  $E_c$ . By manipulating the width of the well, through  $L_z$  we can design the energy state and thus engineer the band gap. The thinner

the layer, the greater the increase in the energy  $E_1$ .



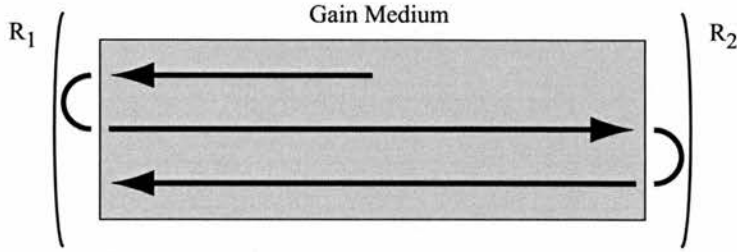
**Figure 2.7:** Density of states in a quantum well of thickness  $L_z$ . The light dashed curve is the normal density of states given by Equation 2.5. The sketch indicates dependence of the wave function along  $z$  for the two subbands shown.

Figure 2.7 demonstrates the step-like density of states for a quantum confined structure within the density of states for a bulk semiconductor. The consequence on a laser is to restrict the allowable energies the electrons can take. This leads to an increase in the efficiency with which the laser operates. This is due to the effectiveness of the stimulation emission which takes place at these restricted energies, because the density of states for the lasing transition is much higher.

## 2.3 Semiconductor Lasers

### 2.3.1 Laser Prerequisites

Two of the fundamental prerequisites for a semiconductor laser are an efficient gain medium and the existence of an optical feedback mechanism. Figure 2.8 shows the simplest case of an optical resonator.



**Figure 2.8:** Basic optical cavity comprising of a gain medium surrounded by mirrors providing the feedback. At low pumping, the gain medium produces loss which acts to decrease the field amplitude. As the pumping is increased, the loss diminishes and oscillation the optical mode along the length occurs.

### Resonant Optical Cavities/Feedback Mechanism

The feedback mechanism is probably the more important component of a laser system. The simplest case consists of two partially reflecting parallel mirrors, with the gain medium located between them. As the field traverses the length of the optical cavity it experiences loss through various mechanisms in the gain medium such as diffraction, scattering, free carrier absorption. This loss is compounded by the optical power emitted from the mirror facets. In order to produce sustained oscillation, the losses are compensated for through a pumping mechanism in the form of carrier injection. In the semiconductor laser, stimulated recombination of these injected carriers provides optical gain as electrons and holes are prompted to recombine by the passing travelling field.

Assuming that the optical gain is approximately constant over the entire length of the laser, the light has an exponential distribution with position  $z$  along the axis of the form

$$F_{\pm}(z) = F_{0\pm} \exp \pm (g - \alpha)z \quad (2.7)$$

where  $F$  is the optical flux density,  $\alpha$  is the optical loss per cm and  $g$  is the optical gain per cm provided by the stimulated emission process. The  $\pm$  and subscripts refer to the forward and reverse components of the wave. For a single round trip, the optical distribution must satisfy the condition that all

the losses incurred are compensated for by the material gain

$$\exp 2(g - \alpha)L = \frac{1}{R_1 R_2} \quad (2.8)$$

where  $R_1$  and  $R_2$  are the power reflection coefficients at the two ends of the resonator and  $L$  is the resonator length. From this one can find the nominal threshold gain  $g_{th}$ , which is constant over the whole length of the laser, in terms of  $R_1$ ,  $R_2$  and  $L$

$$g_{th} = \alpha + \frac{1}{2L} \ln \left( \frac{1}{R_1 R_2} \right) \quad (2.9)$$

### 2.3.2 Material Structure Optimisation

If the relationship between the gain and the current density is known then a threshold current density can be derived. For a single quantum well (SQW) laser the peak gain-current density relation for lasing from only the first quantised electron and hole subband, is given by [65, 66, 67, 68]

$$g_w = g_0 \left[ \ln \left( \frac{J_w}{J_0} \right) + 1 \right] \quad (2.10)$$

where  $J_w$  and  $g_w$  are the injected current density and the peak gain coefficient for a single quantum well and  $J_0$  and  $g_0$  are taken from the point of operation on the gain versus current density relation. Figure 2.9 demonstrates the general form of this relationship, based on the theoretical values of McIlroy *et al.* [69].

For a multiple quantum well (MQW) structure with  $n_w$  quantum wells and a cavity length  $L$ , the required modal gain  $G_{th}$  at threshold condition is

$$G_{th} = n_w \Gamma_w g_w = \alpha + \frac{1}{2L} \ln \frac{1}{R_1 R_2} \quad (2.11)$$

where  $\alpha$  is the internal optical loss,  $\Gamma_w$  is the optical confinement factor per well defined in Equation 3.6,  $R_1$  and  $R_2$  are the optical power reflection coefficients.

For the case of a laser with  $n_w$  quantum wells, the modal gain is approximately  $n_w \Gamma_w g_w$ . The threshold current density  $J_{th}$  for such a laser is then

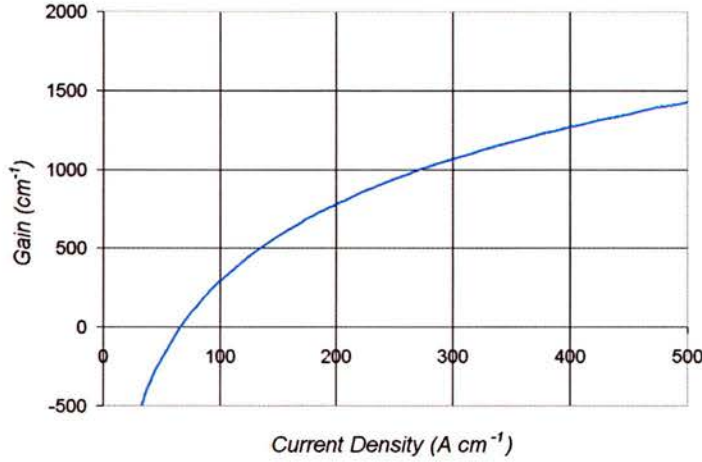


**Figure 2.9:** Calculated gain curve for a single 75 Å wide quantum well. Theoretical values of 1195 cm<sup>-1</sup> and 180 A/cm<sup>2</sup> have been predicted for the optimum gain and current density [69].

$$J_{th} = \frac{n_w J_w}{\eta_{int}} \quad (2.12)$$

where  $\eta_{int}$  is the internal quantum efficiency of the injection current. The relationship between the gain and the current density for a multiple quantum well structure comes from [69]

$$n_w g_w = n_w g_0 \left[ \ln \left( \frac{n_w J_w}{n_w J_0} \right) + 1 \right] \quad (2.13)$$

Figure 2.10 demonstrates this relationship. For the case of a material with one quantum well, the intersection with the horizontal axis occurs when  $J_w = J_0/e$  and  $g_0 = 0$ . For a material with an additional quantum well, the horizontal intersection of the injection current density is shifted to a value close to twice that of a single quantum well material. The relationship can also be seen to increase by a factor of two faster than the case of a single quantum well material.

The key prerequisite for determining the optimum number of quantum wells to be incorporated into the material structure, is the use for which the

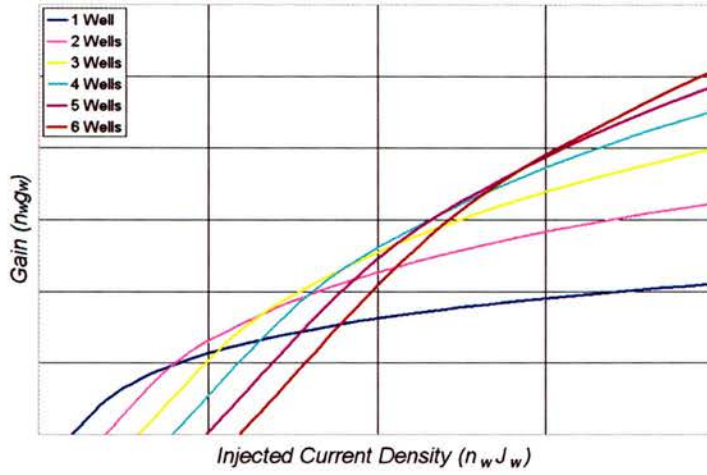


**Figure 2.10:** Gain vs. current density for different numbers of quantum wells.

material is envisaged. The use of a single quantum well material for especially lossy devices, could demand unreasonably high drive currents because the gain goes into saturation. The use of a double or triple quantum well material could achieve the required gain at a lower drive current at the expense of a higher transparency current.

### Optimum Number of Quantum Wells

For real device measurements, a value for the threshold current is routinely measured. The optimum number of quantum wells is inversely proportional to  $G_0$ . Knowledge of the laser's physical dimensions permits the derivation of the threshold current density  $J_{th}(= I_{th}/wL)$ , where  $w$  and  $L$  are the width and length of the laser ridge. The expression for the threshold current is given by

$$I_{th} = \frac{wLn_w J_0}{\eta} \exp \left[ \frac{1}{n_w \Gamma_w g_0} \left( \alpha + \frac{1}{2L} \ln \frac{1}{R_1 R_2} \right) - 1 \right] \quad (2.14)$$

From the expression for  $I_{th}$ , a prefactor which increases linearly with cavity length  $L$ , and an argument in the exponential function that decreases with  $L$ , results in a minimum value for the threshold current. This point, occurs at  $L = L_{opt}$  and defines the optimum length of cavity for minimising the threshold

current. The optimum cavity length parameter

$$L_{opt} \equiv \ln \left( \frac{1}{R_1 R_2} \right) \frac{1}{(n_w \Gamma_w g_0)} \quad (2.15)$$

The associated  $I_{th}^{min}$  is given by

$$I_{th}^{min} = \frac{1}{2} \left( \frac{w J_0}{\eta \Gamma_w g_0} \right) \ln \left( \frac{1}{R_1 R_2} \right) \exp \left( \frac{\alpha}{n_w \Gamma_w g_0} \right) \quad (2.16)$$

If we assume that the loss coefficient  $\alpha$  and other parameters such as  $\Gamma_w$ ,  $J_0$ ,  $\eta$  and  $g_0$  are independent of the number of wells, the optimum number of quantum wells,  $n_{opt}$ , may be determined such that  $I_{th}$  is minimised.

$$n_{opt} = \frac{1}{\Gamma_w g_0} \left[ \alpha + \frac{1}{2L} \ln \left( \frac{1}{R_1 R_2} \right) \right] \quad (2.17)$$

The methods for characterising a typical wafer are discussed in Section 2.4. In order to determine the optimum number of quantum wells we draw upon the values for  $g_0$  and  $\Gamma_w$  (Section 3.2.1). For a laser with 75 Å wells,  $g_0 = 704 \text{ cm}^{-1}$ ,  $\Gamma_w = 0.056$ ,  $\alpha = 13.1$ ,  $R = 0.3$  and a presumed length  $L = 300 \text{ } \mu\text{m}$ , the optimum number of quantum wells is found to be 1.34. Rounding this value up to 2 wells provides the necessary gain performance, a larger value of  $\alpha$ , a shorter cavity or lower reflectivity require that this number be increased.

### Note on Material

The choice of material pairing used for the quantum well and the effects of growth induced stress/strain all act on the operating wavelength and performance of the laser, the value of  $704 \text{ cm}^{-1}$  for the  $g_0$  compares favourably with other research on this material [70].

In the material system investigated, the ternary alloy  $\text{In}_x\text{Ga}_{1-x}\text{As}$  was used for the creation of the quantum wells. The lattice constant of the  $\text{In}_x\text{Ga}_{1-x}\text{As}$  is larger (6.0584 Å) than that of the GaAs substrate (5.6532 Å). This mismatch induces a biaxial strain in the plane of the layers and a uniaxial tensile strain perpendicular to the plane of the layer. The thickness of the of the  $\text{In}_x\text{Ga}_{1-x}\text{As}$  layer is limited by the critical thickness where the strain energy is released

through the generation of dislocations. The biaxial compressive strain removes the degeneracy at the  $\Gamma$ -point in the valence band, leaving the heavy hole band at the highest energy position. Heavy holes therefore determine the bandgap of the material.

### Quantum Well Confinement Barrier Thickness

A barrier thickness of 100 Å is used to ensure sufficient separation of the quantum states from adjacent quantum wells. This avoids the degeneration of individually well-defined energy states into allowable energy bands [71]. Consequently, the design of a multiple quantum well structure is a compromise between the need for quantum state isolation and maximisation overlap between optical mode and quantum well. The threshold current density for a quantum well laser is given by

$$J_{th} = J_{tr} + \left( \frac{1}{\Gamma A} \right) \alpha + \frac{\ln \left( \frac{1}{R_1 R_2} \right)}{2L} \quad (2.18)$$

where  $\Gamma$  represents the confinement factor to allow for spreading of the optical mode outside the active region,  $J_{tr}$  is the transparency current density and  $A$  is the area over which the current is injected.

### 2.3.3 Material Gain

For the semiconductor laser, the interaction between electrons and holes in the gain medium follow one of two possible routes. The first is the emission process, where electrons in the conduction band recombine with holes in the valence band. The recombination of carriers can either occur spontaneously through ‘random’ events or be stimulated by the influence of a third particle, the photon. The material gain is a measure of how efficient this stimulated process can convert the electron-hole pairs into photons. The second process is where a photon is absorbed, in which absorbed photons release their energy into the medium causing the creation of electron-hole pairs. Absorption in this fashion is the reverse of emission.

The overall material gain as a function of frequency, assuming single level contribution, can be approximated by the expression [72, 73]

$$g_m(\omega) = K[f_c(\omega) - f_v(\omega)] \left[ \frac{1}{2} + \frac{1}{\pi} \arctan \left( \frac{\hbar\omega - E_{tr}}{\hbar/\tau_{in}} \right) \right] \quad (2.19)$$

where  $f_c(\omega)$  and  $f_v(\omega)$  are the Fermi-Dirac probabilities of states in the conduction and valence bands are occupied,  $E_{tr}$  is the transparency energy,  $\tau_{in}$  is an intra-band scattering time representing Lorentzian broadening.  $K$  is defined as

$$K = \left( \frac{2 |M|^2}{m_0} \right) \left( \frac{m_r e^2}{4m_0 \nu_g \hbar^2 W \omega \epsilon_0 n_g^2} \right) \quad (2.20)$$

where  $|M|$  is the momentum matrix element,  $W$  is the well width and  $m_r$  is a reduced effective mass.

The evaluation of the this expression over the wavelength range of interest for different injection currents is shown in Figure 2.11. From this graph, the peak gain can be seen to increase with increasing injection current density. The point where gain generated by the medium is equal to the intrinsic losses, referred to as the point of transparency, requires an injected current density of approximately  $1.7 \times 10^{18}$ .

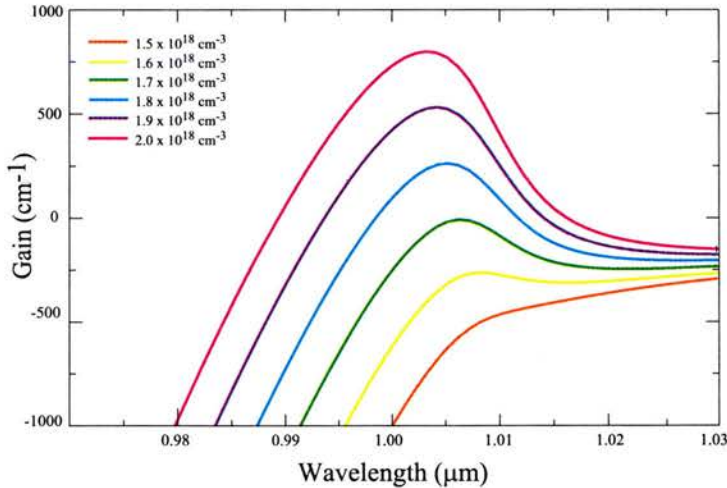


**Figure 2.11:** Theoretical plots of quantum well gain spectra. The well width is 70 Å  $\text{In}_{0.18}\text{Ga}_{0.82}\text{As}$  with GaAs barriers. Adapted from [74]

## 2.4 Material Characterisation

The material quality is commonly characterised by means of fabricating and testing broad area lasers. This allows evaluation of the optoelectronic properties, such as device efficiency  $\eta$  and the threshold current for a cavity of infinite length  $J_\infty$ . The electrical characteristics, especially the contact resistance are obtained separately. Due to the simplicity of fabrication, broad area lasers can be created with relative ease.

### 2.4.1 Broad Area Lasers

The broad area laser is, as the name describes, a laser for which the requirements of single transverse mode operation have been relaxed. Fabrication of these lasers may be achieved by simply defining the metal contacts on the relevant material surface, or by opening adequately sized windows in an insulating layer and blanket metallisation. The devices fabricated for the characterisation of materials used in this project were formed using contacts and ridges measuring 30  $\mu\text{m}$  or 50  $\mu\text{m}$  in width.

### 2.4.2 Broad Area Analysis Theory

The threshold current density of a quantum well laser under forward bias can be approximated by the expression [65]

$$J_{th} = J_\infty \exp\left(\frac{L_0}{L}\right) \quad (2.21)$$

where  $J_\infty$  is the threshold current density for a laser with infinity cavity length. The expressions for  $J_\infty$  and  $L_0$  is given by [64] as

$$J_\infty = \frac{n_w J_{tr}}{\eta_{inj}} \exp\left(\frac{\alpha}{n_w \Gamma_w G_0}\right) \quad (2.22)$$

and

$$L_0 = \frac{\ln\left(\frac{1}{R}\right)}{n_w \Gamma_w G_0} \quad (2.23)$$

where  $n_w$  is the number of quantum wells,  $\eta_{inj}$ , is defined as the injection efficiency, i.e. the fraction of the total carriers injected into the laser which recombine in the active layer.  $\Gamma_w$  is the optical confinement factor per well and  $J_{tr}$  is the transparency current density per well.  $G_0$  is the quantum well gain parameter [69], and  $\alpha$  is the internal optical loss coefficient.

Taking the natural logarithm of the Equation 2.21 for the threshold current density of a broad area laser, we obtain the expression

$$\ln J_{th} = \frac{L_0}{L} + \ln J_\infty \quad (2.24)$$

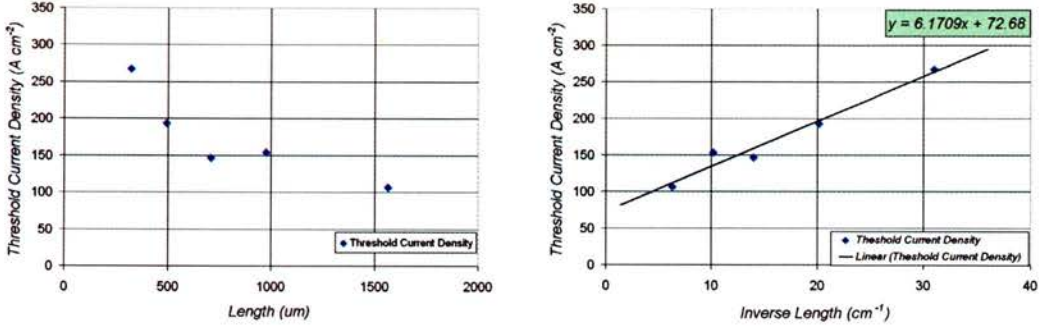
From the assumption [65] that all carriers recombining in the active region do so radiatively, values for  $L_0$  (and therefore  $G_0$ ) and  $J_\infty$  can be determined by plotting the relationship given in Equation 2.24. The form of this equation is that of a straight line, where  $G_0$  and  $\ln(J_\infty)$  are derived from the gradient and intercept point respectively.

### Determining values for $G_0$ and $\ln J_\infty$

The fabrication of broad area lasers and then subsequent cleaving into devices with varying lengths provides a series of results. Figure 2.12 is a plot of the measured threshold current as a function of the cleaved cavity lengths. For the purpose of testing materials in my work, a standard procedure of creating a 2 cm long laser bar containing upwards of 20 individual broad area lasers was adopted. After cleaving and careful inspection, selection and testing of between 5 and 10 lasers was conducted. The data presented in Figure 2.12(b) is a plot of the averaged threshold current density as a function of the inverse cavity length ( $1/L$ ). The intersection of the line of best fit with the vertical axis ( $X = 0$ ) gives a characteristic value for the wafer.

### Deriving Values for $\eta_{inj}$ and $\alpha$

Following on from the experimental determination of the  $G_0$  and  $\ln J_\infty$  parameters, theoretical values for the injection efficiency  $\eta_{inj}$  and material loss  $\alpha$  can be derived from the gradient of the optical power-current curve above the



(a) Plot of threshold current density as a function of cavity length. (b) Plot of threshold current density as a function of inverse cavity length.

**Figure 2.12:** Plot of threshold current density ( $J_{th}$ ) as a function of length (left) and inverse length (right). From the graphs, the effect of the mirror losses can be seen to grow relative to the waveguide loss, as the cavity length is decreased. The overall effect is an increase in the threshold current density. The gain parameter may be determined from the slope of the natural logarithm of the  $J_{th}$  as a function of inverse length.

threshold. The gradient of the optical power-current curves for different cavity lengths provide values for  $\eta_{ext}(L)$ . The expression for the external quantum efficiency is given by

$$\eta_{ext} = \eta_{inj} \frac{\frac{1}{L} \ln\left(\frac{1}{R}\right)}{\frac{1}{L} \ln\left(\frac{1}{R}\right) + \alpha} \tag{2.25}$$

which if re-arranged

$$\frac{1}{\eta_{ext}} = \frac{\alpha}{\eta_{inj} \ln\left(\frac{1}{R}\right)} L + \frac{1}{\eta_{inj}} \tag{2.26}$$

Equation 2.26 provides a means of determining  $\eta_{inj}$  and  $\alpha$  from the gradient and intercept point from the plot of  $1/\eta_{ext}$  as a function of  $L$ . The values for  $\eta_{inj}$  and  $\alpha$  can further be used to predict the value for the transparency current density  $\ln J_{tr}$  of the material using Equation 2.18. Typical key values for the material wafers used are presented in Table 2.2.

In practice, the measured values for  $J_{th}$  and  $\eta_{ext}$  for any individual cavity are subject to a statistical spread. Variations in the  $\eta_{ext}$  values measured for a given device length can arise from difficulties associated with collecting and

**Table 2.2:** Key parameters for various material wafers used to fabricate the coupled cavity lasers.

Material	$J_\infty$	$G_0$	$\alpha \text{ cm}^{-1}$	Confinement Factor
QT 1600	120	540	8	0.03
QT 1841	180	920	6.7	0.05
QT 1719	146	1294	3.7	0.05
QT 1719R	121	706	13.1	0.056

measuring all the optical power from a given laser facet. As an example, the effect of exchanging a  $\times 10$  microscope objective for a  $\times 20$ , alters the captured power by 20 %. This significantly alters the predicted values for the optical power-current curves, and as such a degree of scepticism should be exercised when considering values derived from these graphs. For future measurements, the use of an integrating sphere would capture almost all the light and provide greater accuracy in the measurements.

For this reason little merit is placed on the values for  $\eta_{inj}$  and  $\alpha$  results derived from the plots of  $1/\eta_{ext}$  as a function of  $L$ . Values for the threshold current density,  $\ln J_{th}$ , tend not to suffer from such experimental errors; rather variations in the  $\ln J_{th}$  values may be attributed to non-uniform current injection along the device due to localised imperfections in the device contacts, and to imperfections of the cleaved facets. Any localised reduction in the current density can result in a large decrease of the localised gain due to the logarithmic form of the QW gain curve. This, in turn, can manifest itself as a significant increase in the laser threshold current.

# Chapter 3

## C3 Laser Design

### 3.1 Introduction

The design of the semiconductor wafers is presented along with the modelling results describing their waveguiding properties. Evaluation of the device design with regards to determining the physical structure of the laser required to obtain single mode operation is discussed. The proposed monolithic integration of a Bragg grating to act as a surrogate mirror is investigated, and the design criteria presented. The tuning mechanism is presented and the effect of individual device components on the tuning is discussed. This chapter concludes with a comparison of theoretically predicted results and those measured experimentally.

### 3.2 Material Design

The construction of material through metal organic chemical vapour deposition (MOCVD) growth methods permits the formation of heterojunctions and ultra thin films forming potential barriers and quantum wells. In this section we explore the development of laser ridges through the creation of optical waveguides, and the implications for the final device.

### 3.2.1 Semiconductor Slab Waveguide

Optical waveguides guide light in guided-wave devices and integrated optical circuits. In their most basic form, optical waveguides consist of a thin film of dielectric material possessing a high refractive index, sandwiched between two layers of dielectric materials of lower refractive index. Figure 3.1 demonstrates the basic layout of such a slab waveguide.

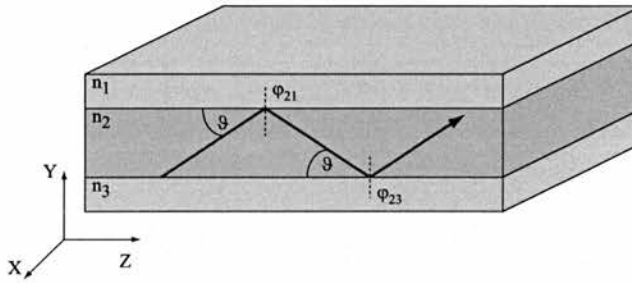


**Figure 3.1:** Schematic of a dielectric optical slab waveguide.

Light can propagate within the thin high refractive index layer by a series of total internal reflections at the material interfaces. During propagation, waves guided by a dielectric slab experience shifts in phase due to both transit through the guiding material and from reflections at the interfaces. These phase shifts, known as Goos-Hänchen shifts [75, 76], are important in determining the condition for supported modes, the criteria for a supported mode is given by

$$2dkn_1 \sin \vartheta + \varphi_{2,1} + \varphi_{2,3} = 2N\pi \quad (3.1)$$

that is to say, the sum of the phase shifts experienced from the two interface reflections in addition to two traverses must be equal to an integer number of  $2\pi$  for constructive interference and therefore guiding to take place.

#### Vertical Optical Confinement

For specific combinations of refractive indices, the optical waveguide may support several optical modes. These modes may propagate along the guide, and

will possess individual propagation constants, reflection angles and effective refractive indices.

In determining the number of optical modes which can be sustained by the slab waveguide, the simplest approach is to examine the dispersion relation. Construction of the dispersion relation starts with determining the individual refractive indices for the constituent layers of the slab waveguide. Using Matlab, a numerical code was written to realise the model [77]. The predicted values, shown in Figure 3.2, are in good agreement with other work on the  $\text{Al}_x\text{Ga}_{1-x}\text{As}$  material base [78, 79].

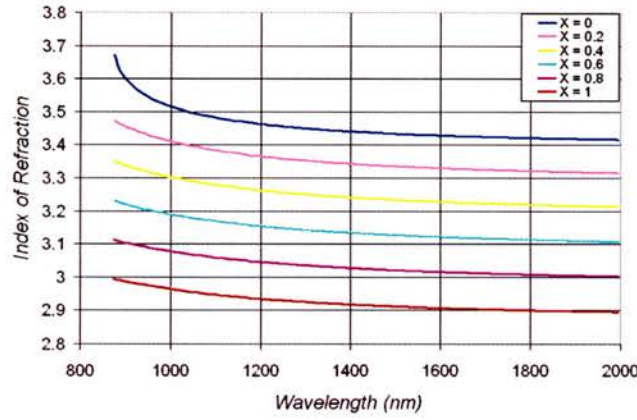


**Figure 3.2:**  $\text{Al}_x\text{Ga}_{1-x}\text{As}$  refractive index as a function of the compositional fraction.

Using the values for the refractive indices, the dispersion relation for waveguides can be solved numerically or graphically, using normalised parameters:

i) the normalised frequency parameter

$$V = k_0 d \sqrt{n_2^2 - n_3^2} = d \sqrt{\beta_2^2 - \beta_3^2} \quad (3.2)$$

ii) the normalised propagation parameter

$$b = \frac{n_{eff}^2 - n_3^2}{n_1^2 - n_3^2} = \frac{\beta^2 - \beta_3^2}{\beta_1^2 - \beta_3^2} \quad (3.3)$$

iii) the asymmetry parameter

$$a = \frac{n_3^2 - n_1^2}{n_2^2 - n_3^2} \quad (3.4)$$

where  $n_1, n_2$  and  $n_3$  represent the refractive indices of the upper cladding, waveguide core and lower cladding respectively (cf. Figure 3.1). The thickness of the waveguide is given as  $d$  and  $k_0$  is the wave vector. Using these generalised parameters, the dispersion relation for any planar waveguide configuration can be realised. Figure 3.3 demonstrated the relationship between the normalised parameters for various values of asymmetry parameter.

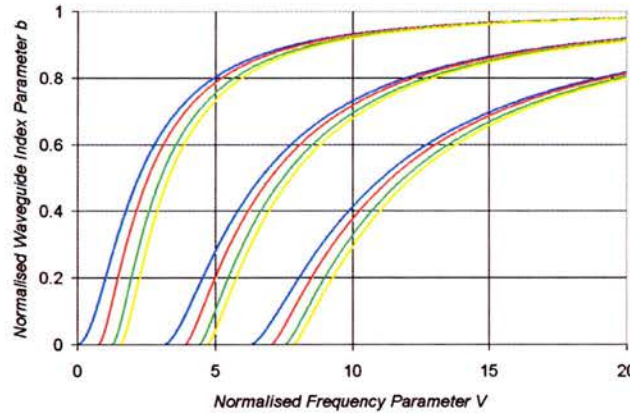


**Figure 3.3:** Normalised dispersion diagram for an arbitrary optical waveguide. The diagram shows the relationship between the normalised waveguide index parameter  $b$  and frequency parameter  $V$  for the first three modes of the waveguide. Each grouping demonstrates the effect of asymmetry of the cladding index, with  $a = 0$  indicated in blue to  $a = \infty$  indicated by the yellow trace.

It can be shown [52] that the number of modes supported in a symmetrical waveguide with thickness  $d$ , is given by

$$M = \frac{4d}{\lambda} \sqrt{(n_1^2 - n_2^2)} \quad (3.5)$$

The incorporation of InGaAs quantum wells during the wafer growth process usually occurs in the middle of the higher refractive index AlGaAs active

layer. As described in the theory chapter, carrier recombination and therefore optical gain occurs at these InGaAs layers. Although the refractive index may be substantially different, the InGaAs quantum wells themselves have virtually no effect on the waveguide confinement, a result of their very small thickness ( $\sim 6$  nm each).

### Waveguide Design

The desired goal of designing a slab waveguide is one of optimising the optical confinement to the waveguiding region. The degree of optical confinement is defined [64] as  $\Gamma_0$ , the fraction of the optical mode which resides within the waveguide to the total optical power carried by the optical mode. For a Quantum well laser, the optical confinement factor  $\Gamma_w$  for a single well takes into account the optical modal distribution and only that fraction of the photons inside the well providing gain. From [80], a simple approximation is, therefore

$$\Gamma_w = \Gamma_0 \frac{L_z}{W_{mode}} \quad (3.6)$$

where  $L_z$  is quantum well width and  $W_{mode}$  is the full width at half maximum of the intensity profile of the optical mode. Typical confinement factor values calculated for materials used here lie between  $1.5 \times 10^{-2}$  and  $7.5 \times 10^{-2}$  per well.

The optimum thickness of the active region is a trade-off between the need to maximise the current density in the active region and confinement of the optical mode mode to the waveguiding layer. Reduction in the thickness of the active layer, acts to increase the carrier density in the layer and hence increase the optical gain. As the thickness of the active layer is reduced, the proportion of the optical mode residing in the waveguide goes down. The loss of photon density results in a reduction of the gain. The optimum thickness of waveguide is given by [81]

$$t = \frac{0.227\lambda}{\sqrt{n_g^2 - n_c^2}} \quad (3.7)$$

where  $n_g$  and  $n_c$  are the refractive indices of the guide and cladding respec-

tively. Assuming that the effect of the  $\text{In}_{0.18}\text{GaAs}$  quantum wells on the GaAs/AlGaAs material base can be neglected. The optimal thickness according to equation (3.7) is 150 nm. In practice, the limitations of the one dimensional model used to obtain equation (3.7) is only partially valid and a more realistic value for the waveguide thickness is 250 nm.

### Lateral Optical Confinement

In the slab waveguide presented above, optical confinement occurs only in the vertical direction. For a practical laser, confinement in the lateral direction must also be achieved.

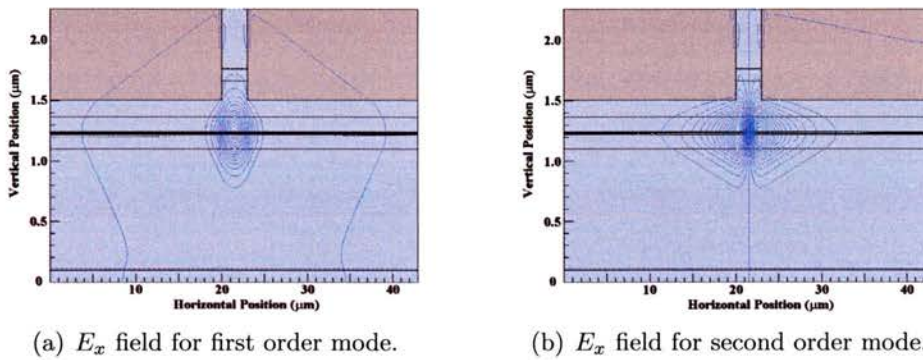


**Figure 3.4:** Simulation results for the electric field distribution for the first and second order modes of a 3  $\mu\text{m}$  wide ridge waveguide. An etch depth of 360 nm provides a ridge effective index great enough to sustain the second order mode. Confinement factors of 5.675 and 5.813 % are calculated for the modes respectively.

The refractive index difference required for guiding is commonly achieved by etching back areas of the semiconductor adjacent to the waveguide, forming a ridge structure. Figure 3.4 illustrates a 3  $\mu\text{m}$  wide ridge waveguide with the electric field distribution for the first (3.4(a)) and second modes (3.4(b)) super imposed. The degree to which lateral confinement takes place is a close function of the ridge width and height. In order to produce a laser which operates with a single fundamental mode, careful control over the physical dimensions of the ridge is required.

### 3.2.2 Single Mode Ridge Waveguide

Specific details of individual modes can be determined using two-dimensional mode solver software packages. Analysis of the modal losses using the Fimmwave software package was performed to determine how the lateral modal confinement of a  $3\ \mu\text{m}$  wide ridge waveguide varies with ridge height.

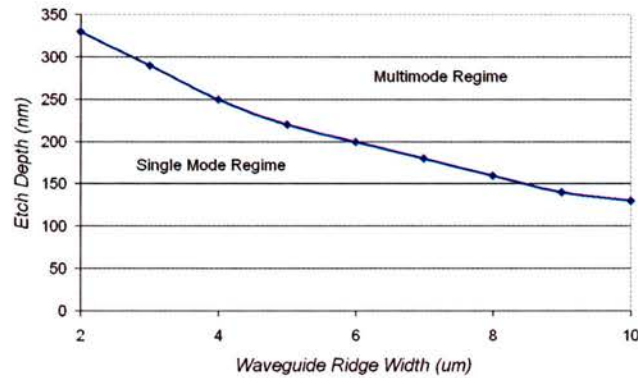


**Figure 3.5:** Plot of etch depth required to sustain the second order mode for a given ridge width.

Using the Fimmwave package, a model of the material structure given in Table 3.1 was constructed. Through modelling the influence of the etch depth on the modal confinement of the ridge, optimal etch depths for a variety of ridge widths were calculated. The depth at which the ridge ceased to remain single moded, was taken as the an limiting etch depth. Figure 3.5 plots this etch depth as a function of ridge width. For the  $3\ \mu\text{m}$  wide ridge width used in my lasers, an etch depth of 290 nm would be required for single mode operation. Etching deeper than this value would increase the effective refractive index of the material under the ridge. This increase in the effective index allows the waveguide to support higher order modes. The effective index is the refractive index optical mode.

**Table 3.1:** GaAs/AlGaAs DQW SCH material QT-1719 laser structure details. Refractive indices extracted from. [82, 83, 84, 85]

Material	Thickness	Doping	Specification	R.I. (980 nm)
GaAs	0.1 $\mu\text{m}$	p+	Capping layer	3.521
Al <sub>0.6</sub> GaAs	0.3 $\mu\text{m}$	8.10 <sup>17</sup>	Upper cladding	3.195
GaAs	0.12 $\mu\text{m}$	undoped	Upper Waveguide	3.521
In <sub>0.18</sub> GaAs	75 $\text{\AA}$	undoped	Quantum Well 1	r.i.
GaAs	100 $\text{\AA}$	undoped	Barrier	3.521
In <sub>0.18</sub> GaAs	75 $\text{\AA}$	undoped	Quantum Well 2	r.i.
GaAs	0.12 nm	undoped	Lower Waveguide	3.521
Al <sub>0.6</sub> GaAs	1 $\mu\text{m}$	8.10 <sup>17</sup>	Lower cladding	3.195
GaAs	-	n+	Substrate	3.521

### Material Description

GaAs/AlGaAs double quantum well (DQW) separate confinement heterostructure (SCH) material from three different wafer designs has been used within this project. Three wafers of the first type, known as QT-1719, QT-1792 and QT-1793 were used. The specific details of each material varied slightly as the project developed. Table 3.1 outlines the general material layer structure for the QT-17\*\* wafers. In addition, a second wafer, known as QT-1841, was investigated for its effectiveness as coupled cavity laser material. The material layer structure for this wafers are presented in Table 3.2.

**Table 3.2:** GaAs/AlGaAs DQW SCH material QT-1841 laser structure details.

Material	Thickness	Doping	Specification
GaAs	0.1 $\mu\text{m}$	p+	Capping layer
Al <sub>0.6</sub> GaAs	0.7 $\mu\text{m}$	8.10 <sup>17</sup>	Upper cladding
GaAs	0.12 $\mu\text{m}$	undoped	Upper Waveguide
In <sub>0.18</sub> GaAs	75 $\text{\AA}$	undoped	Quantum Well 1
GaAs	100 $\text{\AA}$	undoped	Barrier
In <sub>0.18</sub> GaAs	75 $\text{\AA}$	undoped	Quantum Well 2
GaAs	0.12 nm	undoped	Lower Waveguide
Al <sub>0.6</sub> GaAs	1 $\mu\text{m}$	8.10 <sup>17</sup>	Lower cladding
GaAs	-	n+	Substrate

This material design was adapted from a conventional design used extensively by the Optoelectronics Research Group at the University of Glasgow [86]. The material is designed to optimise the internal current-light conversion efficiency,  $\eta_{int}$  and the optical confinement factor per quantum well,  $\Gamma_w$ . The most significant difference between the general QT-17\*\* wafers and the QT-1841 wafer is the depth at which the waveguiding layer and quantum wells are located. The design of the initial wafers was to some extent limited by etch-depth attainable using reactive ion etching processes. Typically RIE etching restricted the depth of the waveguide and cladding layers to the upper 700 to 800 nm of the wafer. In this wafer design, the grating forming Bragg mirrors were subject to a trade-off between losses associated with the over-lap of the upper contact and scattering of the mode into the substrate by diffraction. In Section 3.3.3 the effect of the grating etch depth is examined.

Using CAIBE etching to create the Bragg mirrors demonstrated etch depths up to  $1.7 \mu\text{m}$ . The later wafer designs exploited this by locating the waveguiding layers deeper into the material. Increasing the thickness of the upper cladding decreases losses by reducing the overlap of the mode with the gold contacting layer, while the deeper etching creates gratings which minimises diffraction losses.

## 3.3 Cavity Mirrors

### 3.3.1 Cleaved Facet

The laws of electromagnetic theory specify that the tangential component of the electric and magnetic field vectors on one side of the interface must equal that on the other. The application of these boundary conditions to an electromagnetic wave at an interface leads to the definition of Fresnel's law of reflection, Snell's law of refraction and the definition of the Brewster angle.

For the special case of light-material interaction occurring at normal incidence, the power coefficients for the transmitted and reflected light at the interface is given by [87]

$$R = \frac{(n_1 - n_2)^2}{(n_1 + n_2)^2} \quad (3.8)$$

$$T = 1 - R = \frac{4n_2}{(n_1 + n_2)^2} \quad (3.9)$$

From Equation (3.8), the reflection coefficient is proportional to the square of the refractive index difference. For the AlGaAs system, the refractive index of 1 for air and approximately 3.4 for the semiconductor yields a 30 % reflection of incident light.

### 3.3.2 Multilayer Stack

The use of a cleaved facet provides the necessary feedback for the condition of lasing in an optical oscillator. The facet reflectivity can be enhanced by the application of single or multiple thin films. Figure 3.6 outlines the general case for an electromagnetic impinging on a dielectric thin film.

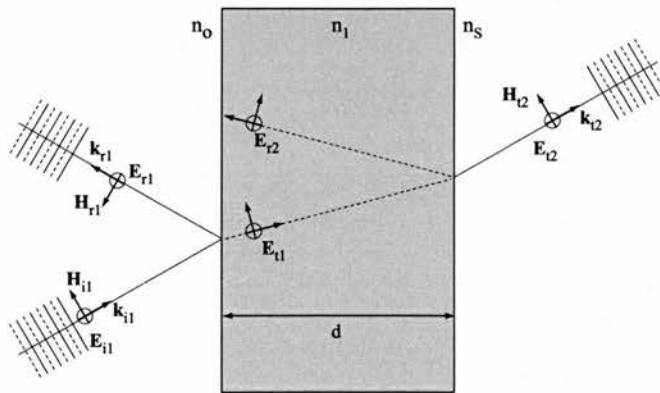


**Figure 3.6:** Schematic of the thin film structure indicating the electric fields.

The optical response of a multilayer stack can be derived as follows, if the assumption of normal incidence is maintained, the electric field ( $\mathbf{E}$ ) and magnetic field ( $\mathbf{H}$ ) are related through the refractive index and the unit propagation vector ( $\mathbf{k}$ ).

$$\mathbf{H} = \sqrt{\frac{\epsilon_0}{\mu_0}} n \mathbf{k} \times \mathbf{E} \quad (3.10)$$

The relationship between the incident and transmitted fields at the boundaries can be written as

$$E_1 = E_2 \cos(k_0 h_1) + H_2 (i \sin(k_0 h_1) / \Upsilon_1) \quad (3.11)$$

$$H_1 = E_2 \Upsilon_1 i \sin(k_0 h_1) + H_2 \cos(k_0 h_1) \quad (3.12)$$

where  $h_i$  represents the phase shift experienced by the wave as it traverses the film of thickness  $d_i$

$$h_i = \frac{(2n_i d_i) \cos \theta_{t2}}{2} \quad (3.13)$$

$$\Upsilon_i = \sqrt{\frac{\epsilon_0}{\mu_0}} n_i \quad (3.14)$$

Equations 3.11 and 3.12 can then be written in form of the characteristic matrix,  $M_i$ , which given a system of  $i$  layers, each with a particular value of  $n_i$  and  $h_i$  provides a general expression of the form 3.15 for each of the  $i + 1$  interfaces,

$$\begin{bmatrix} E_i \\ H_i \end{bmatrix} = \begin{bmatrix} \cos(k_0 h_i) & (i \sin(k_0 h_i) / \Upsilon_i) \\ \Upsilon_i i \sin(k_0 h_i) & \cos(k_0 h_i) \end{bmatrix} \begin{bmatrix} E_{i+1} \\ H_{i+1} \end{bmatrix} \quad (3.15)$$

so the optical properties of each additional layer can be described by a matrix,

$$\begin{bmatrix} m_{11} & im_{12} \\ im_{21} & m_{22} \end{bmatrix} \quad (3.16)$$

and the characteristic matrix of the complete system is the result of the product (in proper sequence) of the individual  $2 \times 2$  matrices.

$$M = \prod_{j=1}^N M_j = M_1 M_2 \dots M_j = \begin{bmatrix} m_{11} & im_{12} \\ im_{21} & m_{22} \end{bmatrix} \quad (3.17)$$

The transmission and reflection coefficients for any configuration of dielectric layers (Figure 3.7) are derived from the matrix elements and the equations

$$r = \frac{\Upsilon_0 m_{11} + \Upsilon_0 \Upsilon_s m_{12} - m_{21} - \Upsilon_s m_{22}}{\Upsilon_0 m_{11} + \Upsilon_0 \Upsilon_s m_{12} + m_{21} + \Upsilon_s m_{22}} \quad (3.18)$$

$$t = \frac{2\Upsilon_0}{\Upsilon_0 m_{11} + \Upsilon_0 \Upsilon_s m_{12} + m_{021} + \Upsilon_s m_{22}} \quad (3.19)$$

The reflectance can be shown to be at a maximum when the conditions for the quarter-wave stack is met i.e. when the optical thickness of the dielectric layers making the stack are equal to a thickness of  $\lambda_0/4$ .

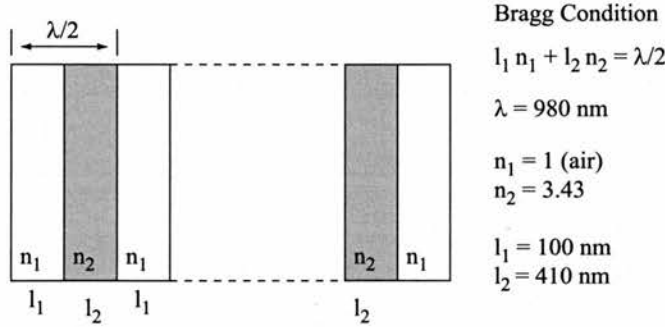


**Figure 3.7:** The periodic structure used for the dielectric mirror consisted of six bi-layers comprised of 100 nm slots spaced with a period of 510 nm. The theoretical response of which is given in Figure 3.9

### Dielectric Mirrors

The main feature of dielectric mirrors is that in comparison to ordinary metallic mirrors, they have extremely low losses at the wavelengths of interest. A dielectric mirror (also known as a Bragg reflector) consists of identical alternating layers of high and low refractive indices, as shown in Figure 3.7. For the development of mirrors operating around the lasing wavelength of GaAs/AlGaAs based lasers (980 nm), a third order quarter-wave stack was used, where the summation of the high and low index layer forming one period of the reflector were selected to be equal to  $3\lambda_0/4$ .

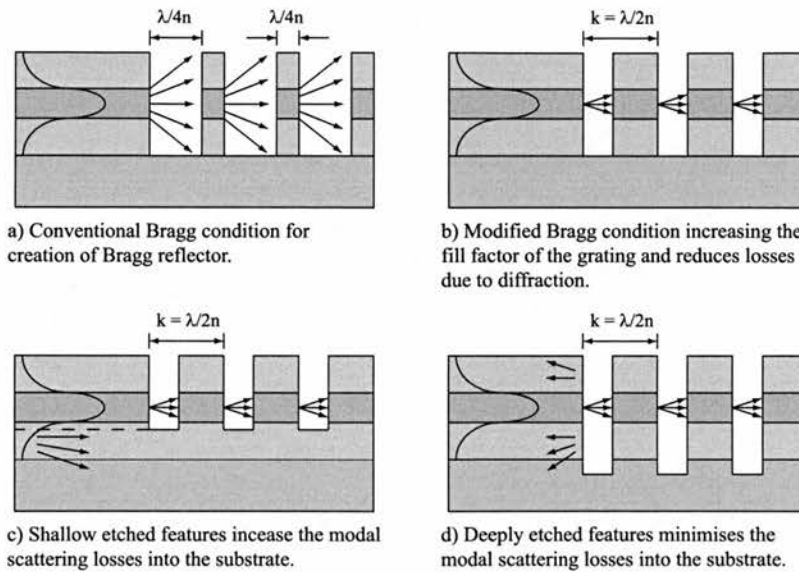


**Figure 3.8:** The effect of grating geometry on the scattering of the optical mode into the substrate. Subfigure a) shows the traditional Bragg reflector conforming to the Bragg condition, while b) demonstrated the effect of the modified Bragg condition. The effects of grating depth on the optical mode is demonstrated in c) and d), where intuitively the deeper etching acts to reduce the amount of scattering into the substrate.

Figure 3.8 illustrates the different factors which influence the efficient operation of the Bragg reflector. When creating the reflector using air slots, the traditional  $\lambda/4$  method of defining the reflector dimensions leads to thickness of the dielectric layers which are approximately  $1/n_{\text{material}}$  the thickness of the air slots. Figure 3.8(a) demonstrates a Bragg reflector constructed following  $\lambda/4$  method. The result of such large slots is a high diffraction and associated loss of the optical mode at the interface. This diffraction can be minimised by reducing the dimension of the air slot, such that a larger proportion of the optical mode can be coupled into the subsequent element of the Bragg reflector. Figures 3.8(c) and 3.8(d) illustrate the effect of the grating etch depth on the optical mode. This is discussed further in Section 3.3.3

The standard arrangement is to have an odd number of layers, with the high index layer being the first and last layer. The condition for creation of

an  $N^{\text{th}}$  order quarter-wave stack is

$$l_1 n_1 + l_2 n_2 = \frac{N \lambda_f}{2} \quad (3.20)$$

where  $N$  is the the order of the mirror,  $n_{1,2}$  are the refractive indices of the two materials forming the mirror and the product  $l_j n_j$  is the optical length of the mirror elements. The desired wavelength for which the mirror is to operate is given by  $\lambda_f$ .

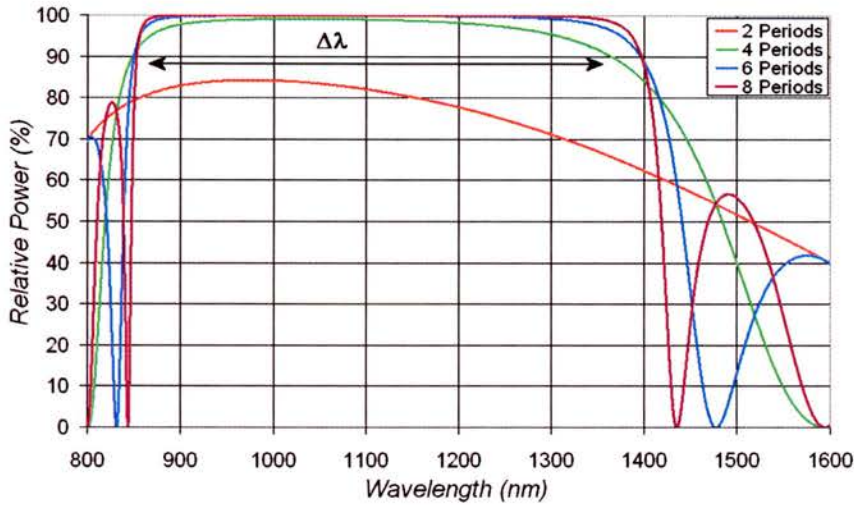


**Figure 3.9:** Theoretical traces of the reflection spectra around 980 nm for multiple periods of Bragg mirrors.

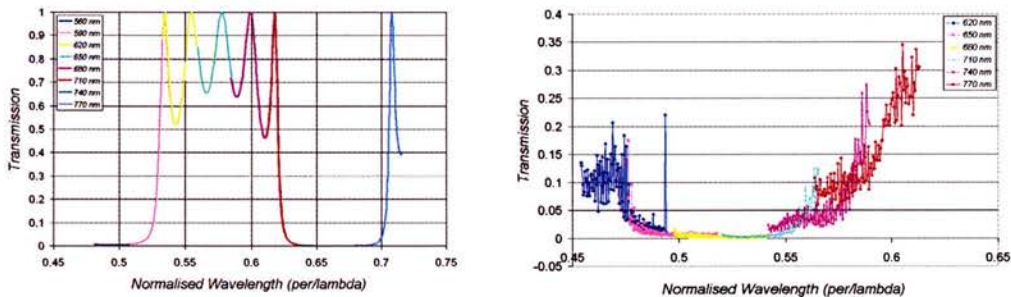
Considering the practicability of fabrication, the physical width of 100 nm for the air slot is selected. Assuming a refractive index of 1 for air, a third order mirror has a period of approximately 560 nm. The reflection response for the dielectric mirror with third order quarter-wavelength layers is presented in Figure 3.9. From the graph, as the number bilayers  $N$  increases, the reflection response becomes flatter within the bandwidth  $\Delta\lambda$ , and has sharper edges and tends to 100%. The bandwidth  $\Delta\lambda$  represents the width of the reflecting band.

### 3.3.3 Investigating the Grating Design

In an effort to examine the operation of the gratings and their effectiveness as a cleaved facet substitute, transmission measurements for the devices with various grating parameters was conducted.

#### Lithographic Tuning

In order to characterise the grating, the optical transmission through the grating as a function of wavelength was measured. The lack of available tunable sources with large scanning ranges around the 980 nm operating point prompted the use of a Hewlett Packard 8167B tunable laser operating with  $\approx 100$  nm scanning range operating over the range 1265 - 1365 nm. This laser was used in conjunction with the technique of lithographic tuning to examine the grating response. The technique of lithographic tuning is based on adjusting the dimension of the structure being characterised with reference to the wavelength range of the laser source used for characterisation. In this way lithographic tuning allows the actual tuning range of a source to be extended, offering an effective characterisation range significantly greater than that of the laser.



(a) Theoretical response of a Bragg mirror calculated using the 1D method discussed in the previous section. (b) Measured response for gratings fabricated to the same dimensions.

**Figure 3.10:** The response from a series of one dimensional Bragg reflectors designed to utilise the 100 nm tuning range from a HP-8167B tunable laser. Comparison between the measured and predicted grating response shows good agreement.

Lithographic tuning of a grating can be achieved by normalising the di-

mensions of the grating to the wavelength range of the laser used for the characterisation. The spectral response from a series of slightly differing gratings can be stitched together to offer the response of a single grating for which the details are known. Figure 3.10(a) demonstrates the one-dimensional theoretical response for a series of gratings. The trace consists of eight individual wavelength traces taken over the operating range of the 8167B tunable laser and stitched together. Figure 3.10(b) is the actual measured response for the same series of gratings. The ratio of slot-to-material has been fixed at  $\approx 20\%$ , while the grating period varies from 620 nm to 770 nm in steps of 30 nm. One can see that while the measured response follows quite closely that of the theoretical response, there is noticeable shift on the measured response and a widening of the band gap of the grating. This demonstrates the inadequacies of using the simple one-dimensional model to predict the response of a complex three-dimensional structure.

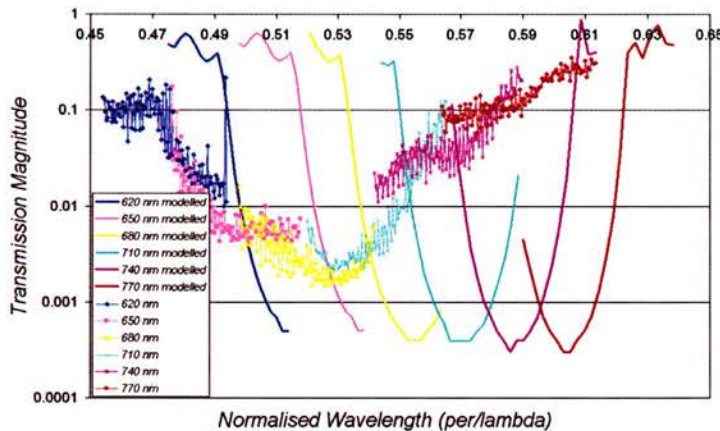


**Figure 3.11:** Theoretical traces of the reflection spectra around 980 nm for multiple periods of Bragg mirrors.

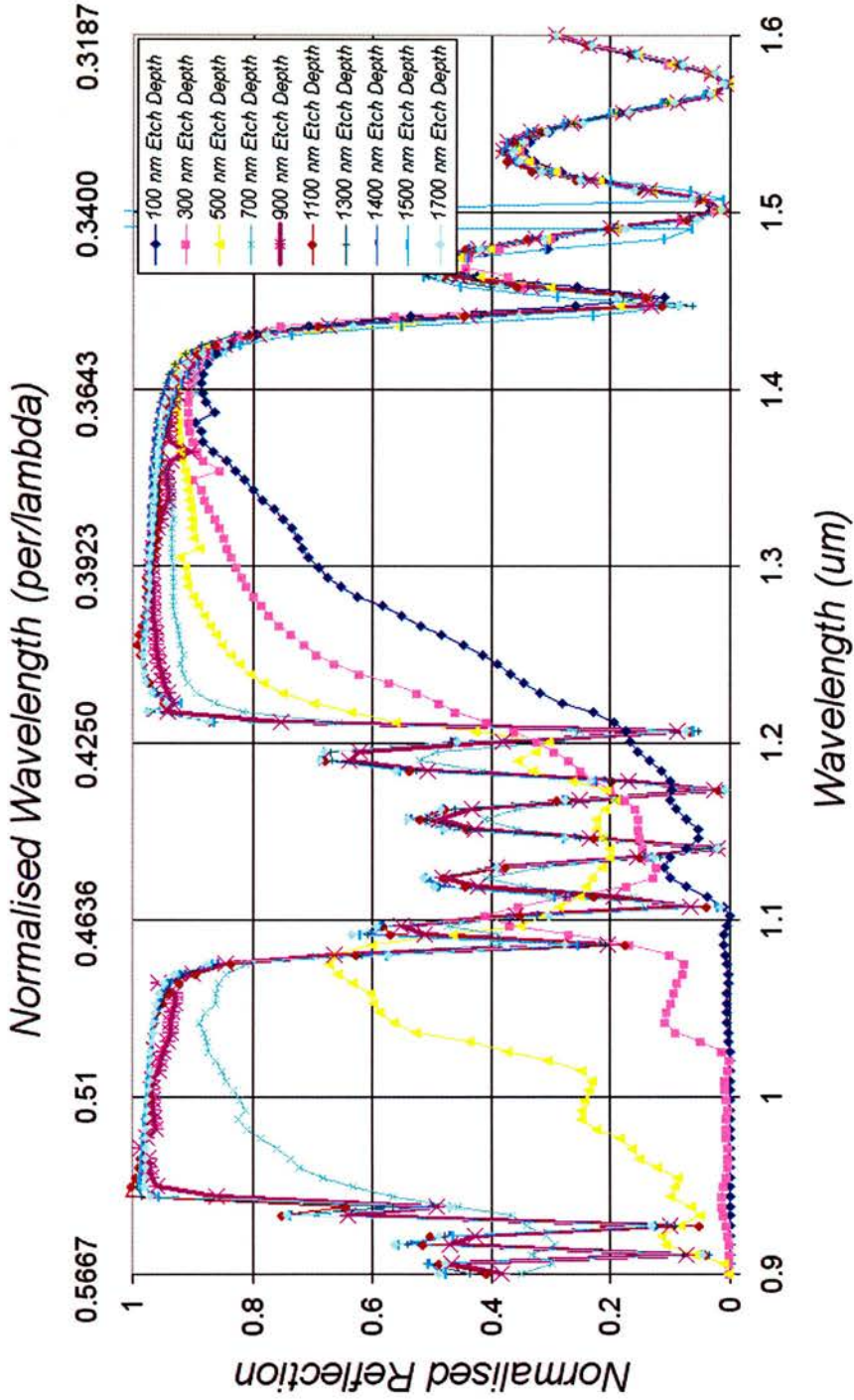
Figure 3.11 illustrates the overlay of a theoretical and the measured wavelength response for the set of gratings already mentioned (cf. Figure 3.10(b)). In this plot a two-dimensional mode solver package was used to predict the theoretical response of the gratings. Concentrating on the solid marker-less lines of the theoretical response one can see that there is a distinct feature illustrat-

ing the drop in the transmission of the grating. The lengths of the curves are representative of the tuning range of the laser (approx. 100 nm), while the colours of the plots represent the period of the grating. The most significant feature of the plot is the shift to higher normalised wavelengths experiences by the feature. This shift is attributed to the dimensions of the gratings. In the two-dimensional model used the grating structure in the direction of propagation are increased for each grating examined while the structure remains constant in the waveguide direction. The shifting of the spectra accounts for the apparent broadening of the grating's bandgap. This effect is unavoidable and illustrates a limitation for using the lithographic tuning method of characterising gratings.

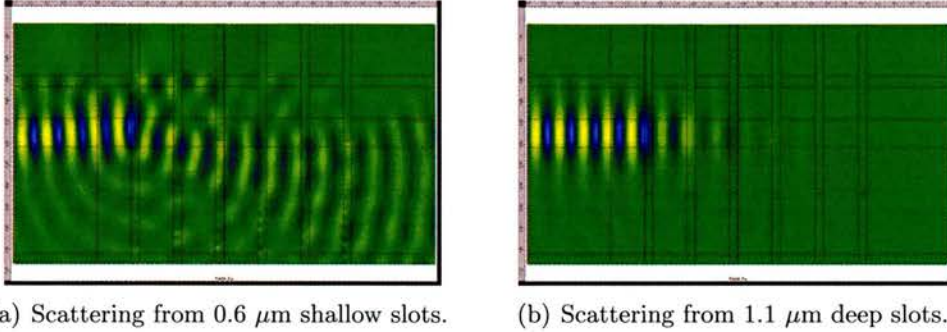
In Section 3.2.2 the effect of the slot dimensions on the grating performance was briefly discussed. The 2D mode solver package was used to model the 6 period grating structure based on the dimensions for a Bragg reflector operating at 980 nm. The precise details of the material structure used in the model are given in Table 3.1. For the mode solver computations the left and right hand side boundary conditions are set to react as magnetic walls, while perfectly matched layers (PML) of 50 nm thickness were added to reduce interference from reflections of the upper and lower boundaries of the computation window.

Figure 3.12 demonstrates the normalised theoretical transmission versus wavelength response from the model. It can be clearly seen from the model that the reflection band starts to form with only the slightest variation in the refractive index. Incremental depths, spaced with a difference of 200 nm were calculated and the results presented together on the same graph.

The main loss mechanism for this kind of structure is the scattering of the mode into the substrate. Figure 3.13 demonstrates the effect of the slot etch depth. For the shallow etched grating (left) the scattering into the substrate reduces the reflected power to  $\approx 19\%$  and the transmitted power to  $\approx 9.1\%$ , while values of  $\approx 95.6\%$  and  $\approx 0.0276$  are obtained for the reflection and transmission coefficients respectively by the deeply etched grating of the same dimensions.



**Figure 3.12:** Theoretical prediction of the reflection power coefficient modelled using FimmWave 2D mode solver package. From the graph one can see the reflection approaches unity as the etch depth becomes deeper. The wavelength range around 900 - 1100  $\mu\text{m}$  demonstrates the development of the reflection band as the slot etch depth increases.



**Figure 3.13:** Graphical outputs from the 2D mode solver program. The material structure simulated is the QT-1719 material, which possesses a waveguiding layer buried 400 nm under the surface. Figure 3.13(a) demonstrates the interaction of the forwards and reverse travelling wave for the case of shallow slots which only penetrate the waveguide by 200 nm. Values of  $\approx 19\%$  and  $\approx 9.1\%$  are obtained for the reflected and transmitted power coefficients. Figure 3.13(b) demonstrates the effect of deep etching through the waveguiding layer. Values of  $\approx 95.6\%$  and  $\approx 0.0276\%$  are obtained for the reflection and transmission power coefficients.

### 3.4 Tunable Coupled Cavity Lasers

The generic layout of a coupled cavity semiconductor laser is shown in figure 3.14. The device comprises two individually pumped cavities of dissimilar lengths, separated by an Inter-Cavity Reflector (ICR). Although 2-D photonic crystals have been reported [88, 89, 90], in this work a simple single slot is used as an ICR. Also a multi-layered mirror replaces the more standard cleaved facet [91].

#### 3.4.1 Principles of Operation

The operation of a coupled cavity system is based on the spectral coincidence of the longitudinal cavity modes. Under normal operation, each laser cavity possesses an independent mode structure. The mode selection mechanism is governed by several effects, the most important being the coupling between the cavities which contributes to the mode selectivity of the overall device. If the width of the gap is chosen correctly, the ICR introduces a strong spectral filtering effect.

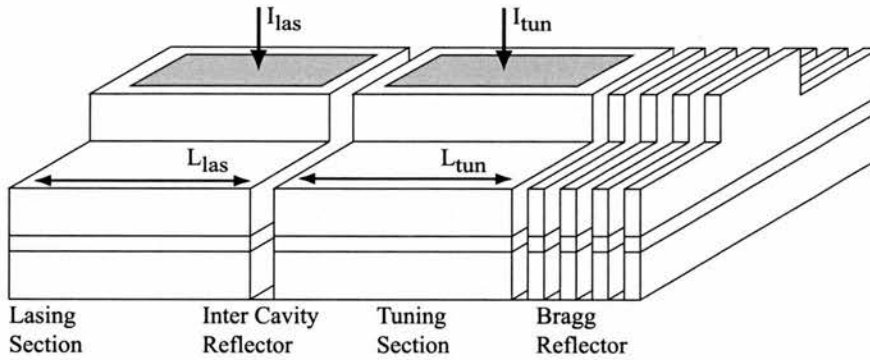


**Figure 3.14:** Schematic of a coupled cavity semiconductor laser incorporating a multi-layer mirror.

A second mechanism relies on the tuning section acting as a spectrally dependant resonant reflector. Longitudinal modes that do not coincide with reflectivity peaks within the tuning section will experience greater losses and hence have a larger gain threshold than modes that do. The reflectivity peaks can be shifted through carrier induced refractive index changes. This allows for a very simple method of changing the wavelength of the laser by varying the current to the tuning section.

### 3.4.2 Cavity Length Ratios

The ratio between the lengths of the cavities has a very dramatic effect on the tuning behaviour of the device. A long lasing section and a tuning section of significantly shorter length offers good mode stability against pumping current and temperature. Alternatively, if both sections are similar in length then a much broader tuning range can be obtained. By considering the mode spacing between two cavities [92] we can determine how much of a wavelength shift must occur before a mode-hop takes place. In the case of a longer lasing section and shorter tuning section mode-hops occur due to a wavelength shift of

$$\lambda_{shift} = \frac{\lambda^2}{2nL_{las}} \quad (3.21)$$

for a lasing wavelength  $\lambda$  and a wavelength refractive index  $n$ . For sections of similar length this wavelength shift is given by

$$\lambda_{shift} = \frac{\lambda^2}{2nL_{las}} \left( \frac{L_{las} - L_{tun}}{L_{tun}} \right) \quad (3.22)$$

This indicates that if significant discontinuous wavelength tunability is to be obtained, we should choose very similar lengths, as even a small shift of the Fabry-Perot mode can lead to mode hopping. However, care should be taken to ensure that there is enough of a length difference between the cavities to ensure sufficient difference in gain between adjacent modes. This can be estimated [93], where we assume that the gain varies quadratically with wavelength

$$g(\lambda) = g_N(N - N_0) - g_\lambda(\lambda_{peak} - \lambda)^2 \quad (3.23)$$

To ensure the existence of a  $5 \text{ cm}^{-1}$  difference between adjacent modes this implies that we require a modal spacing of  $\Delta\lambda \geq 5 \text{ cm}^{-1}/g_\lambda$  [94, 95]. This can be satisfied using the following expressions:

$$\Delta\lambda = \frac{\lambda^2}{2(n_{las}L_{las} - n_{tun}L_{tun})} \quad (3.24)$$

$$\Delta\lambda = \frac{\lambda^2}{2n_{tun}L_{tun}} \quad (3.25)$$

for similar and dissimilar cavity lengths respectively.

For devices of differing length a shift of approximately one mode spacing is required in order to achieve mode hopping, which offers increased stability. This does mean that the wavelength tuning range is decreased. We also note that there is a maximum cavity length difference [93] that should be maintained to ensure that there are not too many modes within the loss ripple of the tuning section to hinder mode selection.

We therefore wish to examine wide range tunability and therefore focus on cavities of comparable length. From typical gain spectra associated with an InGaAs active region emitting near  $1 \mu\text{m}$ , it can be determined a minimum cavity difference of approximately  $15 \mu\text{m}$  should be maintained.

### 3.4.3 Inter Cavity Reflector

The ICR plays an essential role in the spectral behaviour of a coupled cavity laser. A suitable air gap that is etched to the required accuracy is vital to ensure good performance. Two apparently contradicting results were presented by Coldren [96] and Marcuse and Lee [97]. Coldren asserted that air gaps with an integral number of half wavelengths in length gave a much better mode selectivity. However, Marcuse et al suggested that half wavelength gaps provided the least mode selectivity. This initially confusing difference of opinion was explained by Buus et. al. [98] who showed that the gap loss plays a significant factor on which the gap width should be selected.

For a low loss ICR, if the gap length coincides with an integer wavelength of a particular mode resonant in both cavities, interference effects reduce the transmission of the mode into the gap. This lowers its gain threshold substantially compared to adjacent modes. This mode will then be the naturally preferred wavelength of operation. For a high loss ICR, diffraction is the predominant loss mechanism. This loss becomes more significant as the width of the gap is increased.

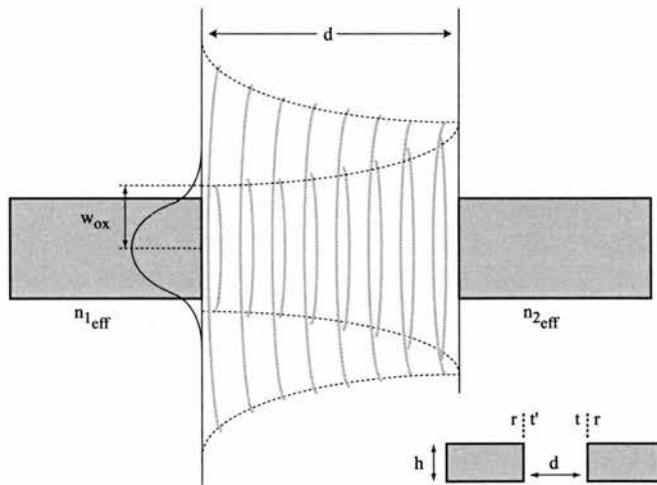


**Figure 3.15:** Schematic of the intercavity reflector. Diffraction losses are the dominant loss mechanism at the ICR, using Gaussian diffraction the effective coupling coefficients can be determined. Adapted from [99]

The criteria for strong cavity coupling requires that the air gap length should be maintained at less than one half wavelength. This does not necessarily lend itself to good mode selectivity. A length that will provide a gain difference of at least  $5 \text{ cm}^{-1}$  between the lasing mode and next adjacent mode should be selected. This should be sufficient to give approximately 25 dB side mode suppression [99]. As an example, we calculate the power transmission, reflection and loss through an air gap of 1 micron emitted from an active layer waveguide of  $25 \mu\text{m}$  using the method presented in [100]. This calculates the losses due to diffraction of a Gaussian beam within the gap. Figure 3.15 illustrates the two dimensional diffraction which occurs within the air gap between two waveguides, note the phase front curvature [101]. Figure 3.16 demonstrates the theoretical power transmission, reflection and loss as a function of the ICR width. The active layer This calculates the losses due to diffraction of a gaussian beam within the gap. Strong peaks are exhibited at integral half wavelengths as expected, in addition to substantial losses due to diffraction.

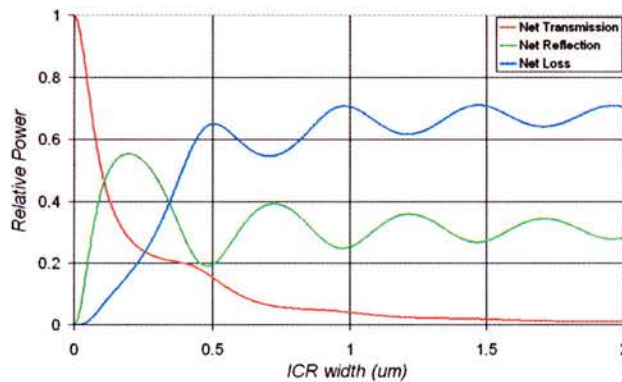


**Figure 3.16:** Plot of the ICR transmission and reflection response as a function of the gap width. Losses due to diffraction are represented by the green line. Adapted from [100]

This method assumes that the ICR is a plane-parallel groove of width  $L$ , with a single facet reflectivity for the guided mode of  $\pm r$  and amplitude transmission factors of  $t$  and  $t'$  that account for diffraction and mode re-excitation loss for a single pass or round trip in the groove, respectively. With reference

to Figure 3.15, the net reflection  $R_{net}$  and net transmission  $T_{net}$  are given by:

$$R_{net} = r - \frac{rt'(1-r^2)}{1-r^2t'} \quad (3.26)$$

$$T_{net} = \frac{t(1-r^2)}{1-r^2t'} \quad (3.27)$$

The transmission factors  $t$  and  $t'$ , for propagation lengths  $L$  and  $2L$ , respectively were calculated neglecting diffraction in the substrate plane. Using Gaussian diffraction perpendicular to the plane for a propagation constant  $\beta = 2\pi/\lambda$  in the groove. These approximations lead to an expression for the transmission coefficient as a function of the inter-cavity reflector length:

$$t(L) = \sqrt{\frac{2w_0w_L}{[w^2(L) + w_0^2]}} e^{-i\beta L} \quad (3.28)$$

where the individual components

$$t = t(L) \quad (3.29)$$

$$t' = t(2L) \quad (3.30)$$

$$w(L)^2 = w_0[1 + (\lambda L/\pi w_0^2)^2] \quad (3.31)$$

$$w_0 \simeq 0.5d \quad (3.32)$$

### Effective Reflector

Combining the multi-layer mirror, inter cavity reflector, and tuning cavity into a single *effective reflector*  $R(\lambda)$ , the analysis of the coupled cavity laser system may be simplified to that of a single cavity possessing an equivalent wavelength-dependant mirror. The mirror loss of such a system is given by

$$\alpha_m = \frac{1}{2(L_{las} + L_{eff})} \log \frac{1}{|r_{las}| |R(\lambda)|} \quad (3.33)$$

where  $r_{las}$  is the facet reflectivity at the lasing end of the device and  $L_{eff}$  is the effective length of the mirror. The gain threshold  $g_{th}$  of the laser can then be determined from

$$\Gamma g_{th} = \alpha_s + \alpha_m \quad (3.34)$$

For an active layer confinement factor  $\Gamma$  equal to 0.02 and internal scattering losses  $\alpha_s$  equal to  $2.5 \text{ cm}^{-1}$  Figure 3.17 illustrates the effective reflectivity for several combinations of tuning cavity section and inter-cavity reflector lengths. The corresponding gain thresholds for devices with a lasing cavity length of  $300 \text{ }\mu\text{m}$  and ICR lengths of 250 nm, 375 nm and 500 nm are illustrated in Figure 3.18.

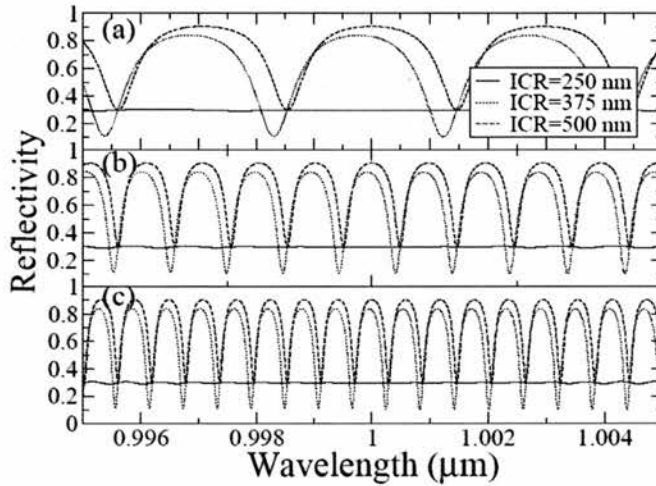


**Figure 3.17:** The effective reflectivity for various lengths of the tuning cavity, a)  $50 \text{ }\mu\text{m}$ , b)  $150 \text{ }\mu\text{m}$  and c)  $250 \text{ }\mu\text{m}$ . Each graph contains traces for different inter-cavity reflectors corresponding to  $\lambda/2$ ,  $\lambda/4$  and  $3\lambda/8$ . Courtesy of [74]

The air gap of 500 nm offers the highest reflectivity at  $1 \text{ }\mu\text{m}$  and hence the highest finesse. This presents itself as the best wavelength filter with the highest gain threshold variation. A quarter wavelength ICR offers approximately half the gain threshold difference but with a much broader selectivity peak. The air gap of 375 nm  $3\lambda/8$  offers little advantage as an ICR.

Modes at wavelengths with high equivalent mirror reflectivity naturally have lower thresholds. The addition of the Bragg reflector results in a significant improvement of the finesse of the effective reflectivity peaks. This leads to an improvement in the side mode suppression ratio.

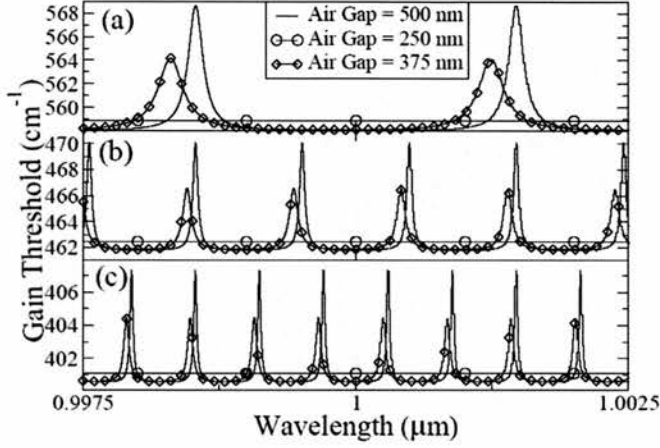


**Figure 3.18:** The gain threshold spectra for various lengths of the tuning cavity, a) 50  $\mu\text{m}$ , b) 150  $\mu\text{m}$  and c) 250  $\mu\text{m}$ . Each graph contains traces for different inter-cavity reflectors corresponding to  $\lambda/2$ ,  $\lambda/4$  and  $3\lambda/8$ . Courtesy of [74]

### 3.4.4 Current Tuning

The dielectric function,  $\epsilon(\omega) = \epsilon_1(\omega) + i\epsilon_2(\omega)$ , is known to describe the optical response of the medium at all photon energies  $E = \hbar\omega$  [102, 103]. The real and imaginary parts of this dielectric function are related to each other by the Kramers-Kronig relations [104]

$$\epsilon_2 = -\frac{2}{\pi} \int_0^{\infty} \frac{\epsilon_1(\omega')}{(\omega')^2 - \omega^2} d\omega' \quad (3.35)$$

$$\epsilon_1 - 1 = -\frac{2}{\pi} \int_0^{\infty} \frac{\omega' \epsilon_2(\omega')}{(\omega')^2 - \omega^2} d\omega' \quad (3.36)$$

The dielectric function is strongly connected with the electronic energy band structures of the material [105]

#### Carrier induced refractive index change

The three significant carrier effects of band filling, bandgap shrinkage and free carrier absorption contribute in significantly different ways to the change in the material band structure. The relationship between the refractive index  $n$

and the absorption coefficient  $\alpha$  is

$$n(E) = 1 + \frac{2c\hbar}{e^2} P \int_0^\infty \frac{\alpha(E')}{(E'^2 - E^2)} dE' \quad (3.37)$$

where  $P$  is the principle value of the integral,  $e$  the electron charge and  $c$  is the speed of light and  $E = \hbar\omega$  the photon energy. By measuring the absorption coefficient one may determine the real part of the refractive index.

### Band-filling Effect

Also known as the *Burstein-Moss effect*, this contribution to the overall change in refractive index due to the band-filling mechanism is a direct result of the injection of carriers. The increase in carrier density and associated filling of the relevant energy band causes a reduction in the absorption, as electrons require an additional (and increased) amount of energy to attain transition in to the conduction band. Although the degree to which band-filling occurs differs with the effective mass, the overall result has contributions from both electrons and holes.

Following the assumption that the energy bands can be approximated by the parabolic band model, the optical absorption at the band edge exhibiting a square-root dependance. The absorption coefficient for an injected semiconductor is

$$\alpha(N, P, E) = \alpha_0(E)[f_v(E_a) - f_c(E_b)] \quad (3.38)$$

where  $N$  and  $P$  are the concentrations of free electrons and holes, respectively,  $\alpha_0$  represents the absorption of pure materials in the absence of any injection.  $f_c(E_b)$  and  $f_v(E_a)$  are the probabilities of occupation of a conduction and valence band states at energies  $E_b$   $E_a$ . The change of absorption as a result of the band-filling effect is given by

$$\Delta\alpha(N, P, E) = \frac{C_{hh}}{E} \sqrt{E - E_g} [f_v(E_{ah}) - f_c(E_{bh}) - 1] + (3.39)$$

$$+ \frac{C_{lh}}{E} \sqrt{E - E_g} [f_v(E_{al}) - f_c(E_{bl}) - 1] \quad (3.40)$$

$$(3.41)$$

where  $C_{lh}$  and  $C_{hh}$  are fitting constants based on the reduced effective masses of the electron-hole pairs. The change in index is then given by

$$\Delta n(N, P, E) = \frac{2c\hbar}{e^2} P \int_0^\infty \frac{\Delta\alpha(N, P, E')}{(E'^2 - E^2)} dE' \quad (3.42)$$

### Bandgap Shrinkage

There is a second effect which influences the absorption coefficient. At high injection current densities there is an effective reduction in the size of the energy bandgap. As carriers fill the band, the wave functions describing individual electrons begin to overlap and through Coulomb forces are forced to repel one another. Additionally, through fermion statistics, electrons with the same spin will similarly avoid one another. The overall result is a decrease in their energy, and an associated lowering/raising in the energy of the conduction/valence band edges. From [106] the bandgap shrinkage is

$$\Delta E_g = - \left( \frac{e}{2\pi\epsilon_0\epsilon_s} \right) \left( \frac{3}{\pi} \right)^{1/3} \chi^{1/3} \quad (3.43)$$

The estimated shrinkage is proportional to the cube-root of the carrier concentration, denoted by  $\chi^{1/3}$ . The effect becomes significant when the carrier concentration forces the inter-electron (hole) spacing in the conduction (valence) bands to become comparable to the effective Bohr radius of the electrons (holes). The positive change in absorption, due to shrinkage is predicted to be

$$\Delta\alpha(\chi, E) = \frac{C}{E} \sqrt{E - E_g - \Delta E_g(\chi)} - \frac{C}{E} \sqrt{E - E_g} \quad (3.44)$$

In contrast to the index change experienced by the band-filling mechanism,

the shrinkage in band-gap causes a positive change in refractive index below the bandgap.

### Free-Carrier Absorption

The free carrier absorption is directly proportional to the concentration of electron and holes and to the square of the wavelength [102]. A corresponding change in the refractive index is given by

$$\Delta n = - \left( \frac{e^2 \lambda^2}{8\pi^2 c^2 \epsilon_0 n} \right) \left( \frac{N}{m_e} + \frac{P}{m_h} \right) = - \frac{6.9 \cdot 10^{-22}}{n E^2} \left\{ \frac{N}{m_e} + P \left( \frac{m_{hh}^{1/2} - m_{th}^{1/2}}{m_{hh}^{3/2} - m_{th}^{3/2}} \right) \right\} \quad (3.45)$$

The mechanisms behind Free-Carrier Absorption involve the promotion of free carriers to a higher energy state within the same band. This intra-band absorption also referred to as the *plasma effect*, always contributes negatively to any change in refractive index. The dependance of the refractive index change ( $\Delta n$ ) on the square of the wavelength ( $\lambda^2$ ), reveals the plasma effect increases as the photon energy is decreased below the bandgap. Conversely, the effects on refractive index of the band-filling and bandgap shrinkage effects on refractive index are greatest near the bandgap, decaying rapidly as the photon energy is reduced.

### Combined Contributions

The three carrier effects of band filling, bandgap shrinkage and free carrier absorption are assumed to be independent. This leads to the total change in refractive index being the sum of the individual effects [107]. For higher carrier concentrations, the band-filling and plasma effect dominate yielding a large negative  $\Delta n$ .

$$\Delta n_{total} = \Delta n_{Bandfilling} + \Delta n_{BandgapShrinkage} + \Delta n_{Free-Carrier} \quad (3.46)$$

### 3.4.5 Tunability

The relationship between the lasing wavelength  $\lambda$ , the cavity mode number  $m$ , the effective index of refraction  $n_{eff}$  and the effective cavity length  $L$  is given by [108]

$$\frac{m\lambda}{2} = n_{eff}L \quad (3.47)$$

If either the effective refractive index, the cavity length or perhaps a change in mode number occurs, a change in the lasing wavelength is experienced. A relative change in wavelength,  $\delta\lambda/\lambda$ , is given by

$$\frac{\delta\lambda}{\lambda} = \frac{\delta n}{n} + \frac{\delta L}{L} - \frac{\delta m}{m} \quad (3.48)$$

The relative change in wavelength is directly proportional to the relative change in either the length, refractive index or mode number. Changes can be brought about by inducing a net cavity index change through carrier injection, employing a mode-selection filter or by a physical change in the cavity length. Of these processes, the carrier induced refractive index change is the most the most effective. Injecting carriers in to the cavity effectively changes the optical path length. From [109] the expected change in refractive index  $\Delta n$  with carrier density  $N$  is given by

$$\Delta n = -\frac{Ne^2\hbar^2}{2m_0E^2\epsilon_0\epsilon} \quad (3.49)$$

where  $\epsilon_0$  is the free space permittivity,  $\epsilon$  is the free relative permittivity, and  $E$  the photon energy.

Considering the steady-state continuity equation for the carrier density  $N$ , we can obtain the following relationship with the current  $I$

$$N = \eta_{int} \frac{I\tau}{eV} \quad (3.50)$$

where  $\eta_{int}$  is the internal quantum efficiency,  $V$  is the volume of the active region and  $\tau$  is the carrier lifetime. We know that the change in refractive index due to free-carrier absorption is always negative and can cause a reduction in

the refractive index of up to 1 % in GaAs.

In terms of the Kramers-Kronig relations [110], changes in the gain/loss spectrum,  $\Delta g(E, N)$  will induce a change in the refractive index, given by

$$n(E, N) = \frac{2ch}{\pi e^2} P \int_0^\infty \frac{g(E)}{E^2 - E_0^2} dE \quad (3.51)$$

where P indicates that the principle value of the integral is taken. Combining these two effects together [111] and using a suitable  $\frac{\partial n}{\partial N}$  we can obtain

$$\Delta n = \frac{\partial n}{\partial N} \frac{\eta_{int} \tau I}{eV} \quad (3.52)$$

For the case of a GaAs/InGaAs active region, typical values of a 0.1 % change in the refractive index can be expected.

For typical values for these parameters in the case of a GaAs/InGaAs active region, a value of approximately 0.1% change in the refractive index is predicted.

The wavelength of longitudinal mode  $m$  is given by

$$\lambda = \frac{2}{m} (n_{las} L_{las} + n_{tun} L_{tun} + n_{bragg} L_{bragg}) \quad (3.53)$$

where  $n_*$  and  $L_*$  are the refractive index and physical lengths of the individual sections making up the coupled cavity laser. A value for the relative shift in resonant wavelength associated with the change in refractive index can be determined from

$$\frac{\Delta \lambda}{\lambda} = \frac{\Delta n_{tun} L_{tun}}{n_{las} L_{las} + n_{tun} L_{tun} + n_{bragg} L_{bragg}} \quad (3.54)$$

This relative wavelength shift neglects the effect of cavity mode-hops that may occur if the wavelength shift is of the order of the mode spacing. For a device possessing a cavity ratio of 300  $\mu m$  to 250  $\mu m$  operating at a wavelength of 1000 nm, a tuning range of approximately 5 nm is predicted [74]. Figure 3.19 illustrates the tuning mechanism which results from varying the below threshold tuning section current and hence the refractive index. This is commonly referred to as the Vernier effect. Fine-tuning of the wavelength can

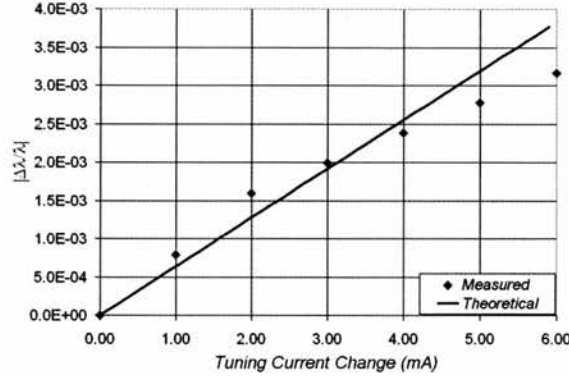


**Figure 3.19:** The theoretical and measured magnitude of the wavelength shift as a function of the tuning current. The graph represents tuning current range from 4 mA to 10 mA.

be achieved in practice through temperature tuning.

### Side-Mode Suppression Ratio

In addition to the tuning range, another key parameter used to characterise coupled cavity lasers is the side-Mode Suppression-Ratio (MSR). The MSR is defined as the ratio of the power in the main mode to that of the most intense side mode. The calculation of the MSR comes from the equation from Agrawal [95]

Figure 3.20 illustrates a generic schematic of loss and gain versus wavelength. The loss margin ( $\Delta\alpha = \alpha_m(\lambda_1) - \alpha_m(\lambda_0)$ ) is defined as the loss difference between the main lasing mode (mode 0) and its nearest neighbour (mode 1). In a similar fashion the gain margin ( $\Delta g = \Gamma g(\lambda_0) - \Gamma g(\lambda_1)$ ) is defined as the gain difference between the main lasing mode (mode 0) and its nearest neighbour (mode 1). The definitions for the gain and loss margins together with the net modal gain for the main mode ( $\delta_G = \alpha_m(\lambda_0) - [\Gamma g(\lambda_0) - \alpha_i]$ ) provide the expression for the mode suppression ratio. This expression is given as

$$MSR = 1 + \frac{\Delta\alpha + \Gamma\Delta g}{\delta_G} \simeq 1 + \frac{\Delta\alpha + \Gamma\Delta g}{(\alpha_1 + \alpha_1^{int})\delta} \quad (3.55)$$

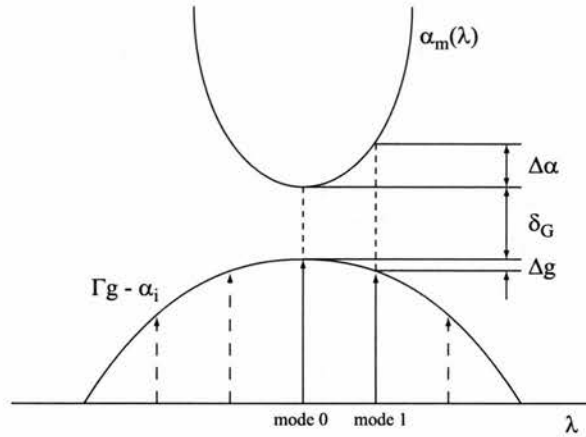


**Figure 3.20:** Definition of gain and loss margins for use in MSR calculations.

where  $\Delta\alpha$  is the threshold gain margin,  $\Gamma$  is the confinement factor,  $\Delta g$  is the gain roll-off from its peak value, and  $(\alpha_1 + \alpha_1^{\text{int}})$  is the total mode gain for the lowest-loss mode. The parameter  $\delta$  is a small dimensionless factor and decreases with an increase in the main-mode power. Typically  $\delta \approx 5 \cdot 10^{-5}$  at a power level of a few milliwatts.

Lasing will occur at the mode with lowest loss closest to the gain peak. The adjacent mode experiences very little gain roll-off  $\Delta g \approx 0$  as the longitudinal mode spacing is small compared to the gain bandwidth. The cavity loss discrimination can provide significant side-mode suppression. For a gain threshold discrimination of  $4\text{--}5 \text{ cm}^{-1}$  up to 30 dB side mode suppression is possible. Moving away from the lasing mode, the gain threshold discrimination increases. However, for the next possible lasing mode  $\Delta\alpha = 0$ . The mode suppression is then entirely due to gain roll-off. If the repeat mode is more than 4 or 5 mode spacings away from the peak gain then  $\Gamma\Delta g \approx 5 \text{ cm}^{-1}$ . Side modes remain suppressed by up to 30 dB even under transient conditions if  $\Delta\alpha \approx 8 - 10 \text{ cm}^{-1}$  [95].

### Switching Times

Carrier injection offers a relative index variation  $(\Delta n/n)$  of about 0.001 with a switching speed of just a few nsec. This is much faster than thermal tuning,

which has a similar index variation but occurs on a time scale of a few msec. Switching time in these types of devices has been studied extensively [112, 92] and is generally less than 10 nsec for transients to settle down between channel switching.

# Chapter 4

## Fabrication

### 4.1 Introduction

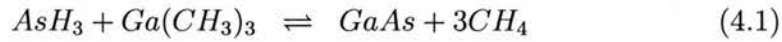
In this chapter, the development of procedures utilized in the fabrication of the coupled cavity structures is presented. Basic fabrication processes are discussed, and emphasis is placed on where the limitations of these procedures have called for the adoption of more advanced techniques. We then consider the factors that determine the limitations of structure definition, and highlight the fact that the proximity effect plays a dominant role in pattern definition. The proximity effect is defined and a procedure for determining correction parameters discussed. We continue by discussing the transfer of patterns from the masking material to form detailed laser structures - examining the dry etch procedures employed in this stage of fabrication. Finally, the stages of fabrication are presented before discussing contact deposition and electrical isolation.

### 4.2 Wafer Preparation

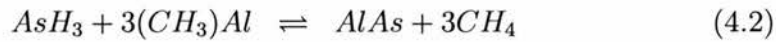
#### 4.2.1 Wafer Growth

The wafers used in my project were grown and supplied by the National Centre for III-V Technologies at the university of Sheffield. The laser structures used were created using Metal Organic Vapour Phase Epitaxy (MOVPE) methods.

The growth of GaAs using the MOVPE method of epitaxy is based on the chemistry of trimethylgallium (TMGa) and arsenic hydride  $\text{AsH}_3$ . The overall reaction leading to the epitaxial growth of gallium arsenide films is



The precursors are gaseous and decompose spontaneously at the heated surface of the growth wafer, forming GaAs. The growth of the  $\text{Al}_x\text{Ga}_{1-x}\text{As}$  is achieved by a very similar gas phase reaction:

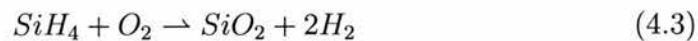


Typically the gallium arsenide seed wafers are heated to between 500 °C and 630 °C, but at such elevated temperatures, decomposition of the gallium arsenide through evaporation of the arsenic occurs. To prevent the thermal decomposition, growth takes place with an overpressure of arsenic in the reactor. Doping of gallium arsenide is achieved by the introduction of dopants to the reactor in vapour form. To obtain n-type material, hydrides of sulfur and selenium can be used. While diethylzinc or diethylcadmium is used to obtain p-type material. Chromyl chloride is used to introduce chromium onto gallium arsenide to form semi-insulating layers.

The addition of aluminium in the form of a precursor is used to create the ternary compound AlGaAs.

### 4.2.2 Silicon Dioxide Deposition

Next,  $\text{SiO}_2$  films are deposited that form the hard mask required for deep etching. In the early stages of the project this mask was a thin dielectric film of Silicon Dioxide ( $\text{SiO}_2$ ), deposited using Plasma Enhanced Chemical Vapour Deposition (PECVD). Layers deposited in this way are formed by reacting silane with oxygen.



Typically, the temperature at which the deposition of silica takes place is around 400 °C. In the later stages of the project, HSQ, a spin on glass was used instead, a gradual migration from the PECVD silica towards the use of Hydrogen Silsesquioxane (HSQ) as the intermediate layer has occurred.

Hydrogen Silsesquioxane ( $\text{HSiO}_{3/2}$ )<sub>8</sub> also known under the trade name of FOx-12, has been demonstrated [113] to behave as a high quality hard mask, possessing sufficient resilience to dry the etch methods, to permit 23 nm period gratings (11.5 nm 1:1 lines and spaces). HSQ has the additional advantage over PECVD in that during its application minimal surface modification takes place. This modification of the surface states/layer being thought to play a major role in the quality of the final contacts.

## 4.3 Device Patterning

Construction of the lasers required the use and development of techniques from many branches of cleanroom fabrication, including lithography, dry chemical etching and electrical contact deposition. The most crucial of these areas, with regard to the work carried out in this project, is that of lithography. Lithography is the process by which a pattern is generated on a sample surface. This either involves the use of a mask, as far as optical lithography, or the direct write method, where a pattern can be written directly onto the semiconductor surface using a focused beam of electrons. These two very different lithographic methods, tools and processes are presented.

### 4.3.1 Optical Lithography

The invention of the microprocessor, credited to Marcian 'Ted' Hoff at Intel (1969/70), could be regarded as the classic example of how advances in the technology of pattern replication shaped the development of the 'computer on a chip' microprocessor. Hoff and the Intel team developed the 4004 - 4 bit architecture, with just over 2300 transistors on an area of semiconductor only 3 to 4 millimeters square. Lithography of feature sizes around 10  $\mu\text{m}$  was required accomplish this feat. Today, with the advent of 64 bit micropro-

processors, typically 5.5 million processors (performing thousands of millions of calculations each second) can be situated on a similar sized area. This current state of play corresponds to minimum feature sizes which lie around 60 nm (a reduction in feature size of 200X), an achievement which is testament to the importance of optical lithographic techniques.

Optical lithography employs the use of a mask plate or reticle, which contains the pattern. The sample onto which the pattern is to be transferred is coated on the desired side with a photosensitive polymer based film, known as photoresist. Using a mask alignment tool, in our case a Karl Süss MJB 3, the reticle and the photoresist coated sample are held in close proximity and the sandwich is uniformly illuminated with ultraviolet light from the reticle side. The process is demonstrated in Figure 4.1. Optimum resolution is achieved when the sample and reticle are held under force such that no gap exists between surfaces, although this technique does risk damage to the sample, reticle or both.

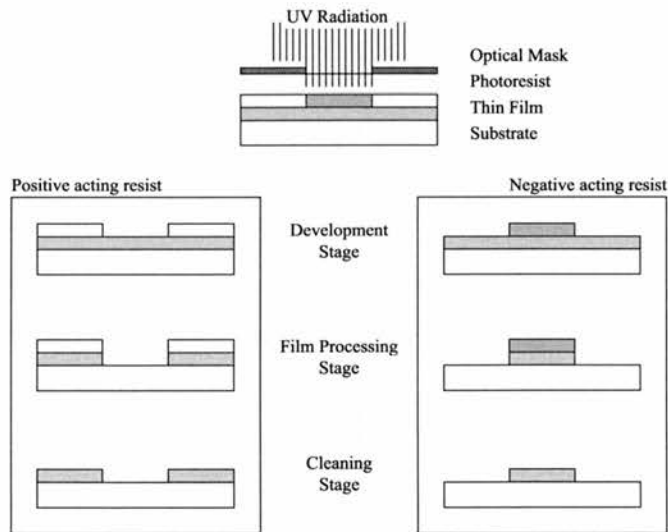


**Figure 4.1:** The basic optical lithographic process.

The photolithographic process is used to create large scale features from waveguides with dimensions of around  $3 \mu\text{m}$  to contact pads with dimensions around  $100 \mu\text{m}^2$ . The optical mask for these structures was produced using

electron beam lithography on a chrome mask plate. Two types of photoresists were typically used, S1818 or S1805, which have film thicknesses of around 1.6  $\mu\text{m}$  and 600 nm when spun at 4000 rpm and baked for 30 minutes at 90 °C. The exposure times for these layers was typically 12 sec and 3 sec, respectively. Development of the exposed areas was achieved by immersion of the samples in Microposit<sup>TM</sup> MF319 for between 25 to 35 seconds, followed by rinsing in RO water for a further 30 seconds. The purpose of the developer is to dissolve the areas of the resist which have been exposed to the UV radiation and thereby be rendered more soluble.

For the optical lithographic equipment used in this project, namely the Karl Süss MJB-3 operating at wavelengths of 405 nm (Hg H-line) and 365 nm (I-line), optical resolutions of better than approximately 1  $\mu\text{m}$  were unobtainable, while optical alignment to previously created features was found to be accurate to within 3 to 5  $\mu\text{m}$ . Given these challenges, a suitable alternative was sought in the use of Electron Beam Lithography.

### 4.3.2 Electron Beam Lithography

Electron Beam Lithography is the process by which a focused beam of electrons is used to expose the desired pattern in a layer of resist. The advantage of patterning samples using EBL lies in the ability to change elements of the pattern from run to run. This means that rapid prototyping and testing of small numbers of new devices can be achieved. In addition, EBL is the preferred technique for the creation of chrome-on-glass masks used in optical lithography. The main disadvantage is that unlike optical lithography, the exposure process takes place sequentially, each part of the design being broken down into geometries, approximately the size of the electron beam waist, and a pre-determined exposure dose conducted.

Figure 4.2 shows a schematic of an electron beam lithography system. At the heart of the system is the electron source. For the Raith/LEO hybrid-system used at St. Andrews, this is a zirconium-oxide coated tungsten filament emitter. An electrical current is passed through this filament until a beam of electrons with suitable current density is obtained. The tip is held under

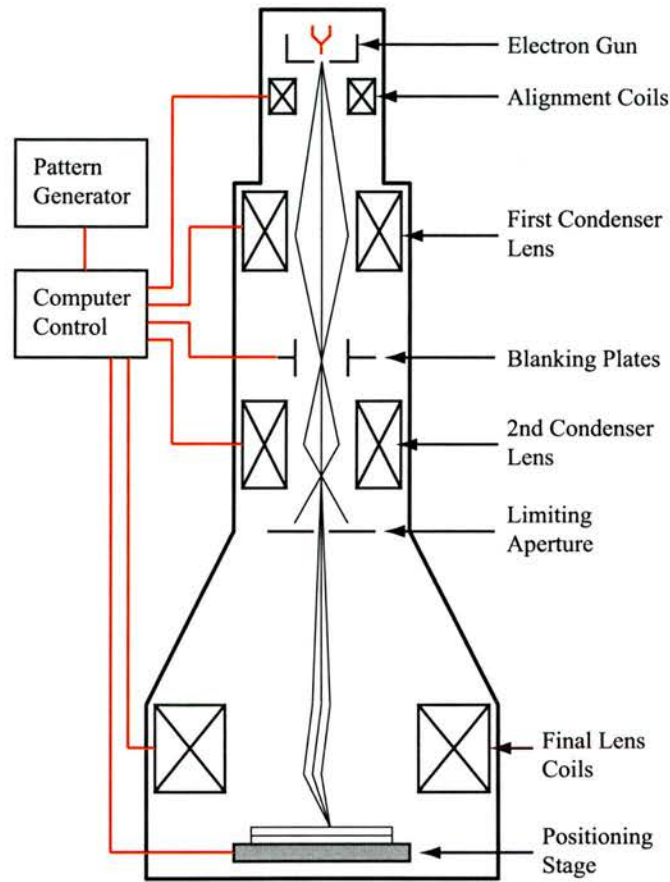


**Figure 4.2:** Schematic of a typical Electron Beam Lithography machine.

ultrahigh vacuum ( $10^{-9}$  mBarr) as the temperatures achieved for the emission process lie in the region of 1800 Kelvin. An Extra High Tension (EHT) power supply is used to extract a proportion of the beam of electrons from the electron source through a fixed aperture, while condenser lenses are used to focus the the electron beam to a spot size of approximately  $3 \text{ nm}^1$ . Modulation of the beam is achieved using beam deflection coils, being computer controlled, act to direct the electron beam to any location within a write field. The write field, defined by the operator, is an sample area which the electron beam is

<sup>1</sup>This value is quoted from Raith as being the best possible size for the LEO GEMINI column and is derived from the spot burning process used to set up the machine for pattern writing.

able to address before the deflection of the beam introduces alignment errors. Ordinarily the complete pattern is larger than the addressable write-field and an overall movement of the sample stage has to take place. In order to facilitate stage movement with high accuracy, the sample stage is equipped with laser interferometer position control.

### Electron Beam Exposure

The resist layer used for the EBL patterning does not contain any photoactive compound, instead the long chain polymer Poly Methyl MethAcrylate (PMMA) is used. The exposure mechanism in this type of lithography is to cut the polymer chains using the focused beam of electrons. Areas of the polymer film which have undergone exposure are more soluble. Figure 4.3(a) demonstrates the exposure mechanism of polymer chain scission. The Average molecular weight<sup>2</sup> for the PMMA used in Elvacite solution was 350,000, while the solutions made by myself have an average molecular weight of 950,000. Another difference between the polymers used is the solvents used to suspend the PMMA. The concentration of the PMMA (in % by weight) to some extent determines which solvent is used. For the 4 % Elvacite commonly used at Glasgow University *o*-xylene is the preferred solvent, while for higher concentrations of PMMA Chlorobenzene is used.

In a similar fashion to photoresist, there exists negative acting ebeam resists. Exposure of negative resist facilitates cross-linking of the polymer chains, which then become less soluble (Figure 4.3(b)). SU-8 is the trade name of one such resist from Dow Corning. This resist offers significant resilience to dry etching techniques, while requiring a very low exposure dose (less than 4 % of that for PMMA).

### Electron Beam Limitations

In optical lithography the limiting factor to the obtainable resolution is the diffraction of light. In electron beam lithography, the resolution is limited by

---

<sup>2</sup>The molecular weight is a measure of the average length of the polymer chain and is related to the sensitivity of the the final polymer film to electron beam exposure. Low molecular weights are more sensitive due to a shorter average chain length.

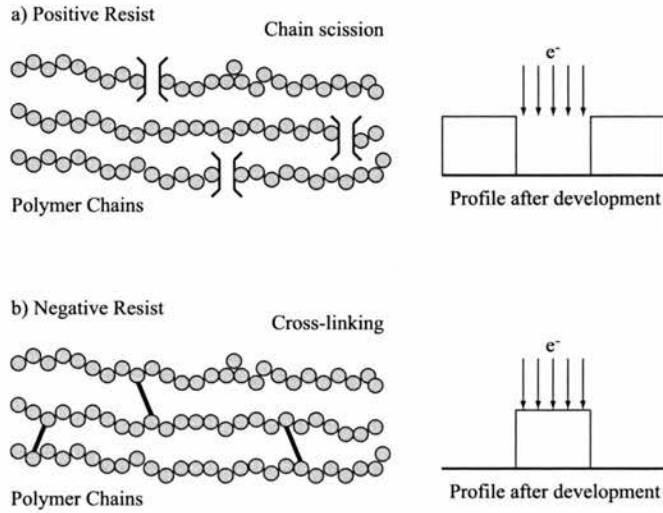


**Figure 4.3:** Exposure mechanisms in positive acting (eg PMMA) and negative acting (eg SU-8) electron beam resists. Electron bombardment causes either chain scission or cross-linking of polymer chains.

the scattering of the electrons. As the electrons penetrate the polymer film and underlying substrate, they undergo collisions, losing energy and changing their trajectory at each scattering event (Figure 4.4(a)). As a result of such interactions there are two significant scattering events, namely scattering in the forward and the backward directions.

Figure 4.4(b) demonstrates the energy distribution of the electrons for a typical exposure. The results presented are derived from a monte-carlo simulation<sup>3</sup> of 500,000 electron trajectories focused to a beam spot of 3 nm at the substrate surface. The substrate follows the material structures used in our experiments, namely GaAs with 200 nm layers of silica and PMMA. The energy of the incident electrons modelled was 20 KeV in accordance with the operating energy of the Raith ebeam machine.

Forward scattering results in the generation of ‘secondary’ electrons. It is these low (2 to 50 eV) energy ‘secondary’ electrons which are responsible for the exposure process. Typically the secondary electrons have a range of only a few

<sup>3</sup>The Monte-Carlo simulation was conducted using the CASINO package developed by Dominique Drouin et. al. at the Universite de Sherbrooke, Quebec, Canada.

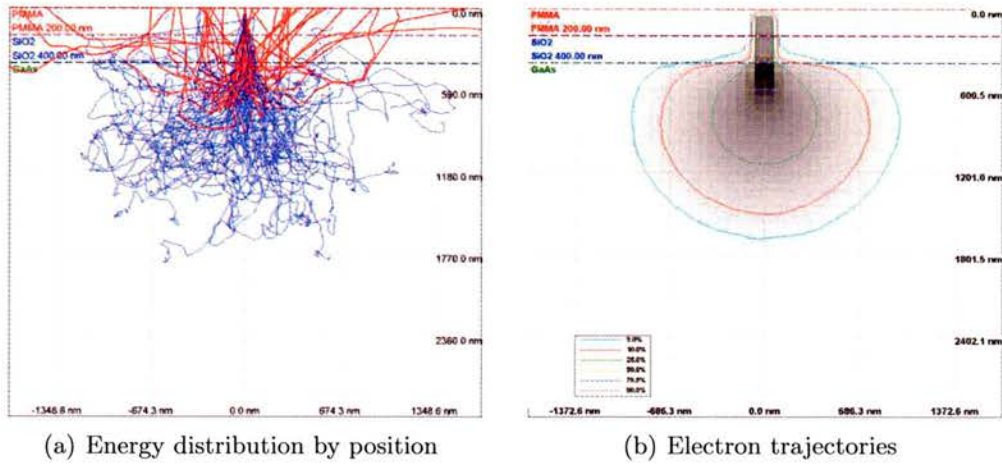


**Figure 4.4:** Monte-Carlo simulation of 20 KeV electron beam impinging on a substrate surface. A GaAs substrate with 200 nm of SiO<sub>2</sub> and a further 200 nm of PMMA is used in the simulation.

nanometers and so do not contribute significantly to the proximity exposure. Backward scattering events are generally associated with the interaction of the electrons after they have passed through the resist and reached the substrate. The incident electrons spread out as they travel through the material until either all the energy is lost or they leave the material due to backscattering. Because of backscattering, electrons can effectively expose material several micrometers away from the center of the exposure beam. This phenomenon is called the *proximity effect*. The proximity effect places a limit on the minimum spacings between pattern features.

### 4.3.3 Electron Beam Proximity Effect

As indicated, the proximity effect is most prominent when the pattern being exposed comprises features that lie in close proximity to each other, and most certainly when this distance is less than the range of the backscattering element of the exposure. Much work has been conducted into the prediction and characterisation of this effect for different substrate and resist materials [114, 115, 116]. Monte Carlo methods are used for the prediction of the dis-

tribution of electrons during the exposure processes. During my work at the USSL facility in Glasgow, a commercial Monte Carlo package by the name of Proxecco was used to generate the expected exposure from electron scattering, while a combination of the CASINO and Raith's own software was used at the facilities in St. Andrews. It is widely accepted that the general form of the electron distribution is provided by a 'double gaussian'. The general form of which is given in Equation 4.4.

$$p(r) = \frac{1}{\pi(1 + \eta)} \left[ \frac{1}{\alpha^2} e^{-\frac{r^2}{\alpha^2}} + \frac{\eta}{\beta^2} e^{-\frac{r^2}{\beta^2}} \right] \quad (4.4)$$

where  $\alpha$  is defined as the range of the forward scattering,  $\beta$  is the range of the backward scattering and  $\eta$  is the ratio of integrated proximity effect function of the backward scattered electrons to that of the forward scattered electrons. Figure 4.5 demonstrates the backscattered component this distribution. It is this backscattering component which is primarily responsible for the proximity effect.

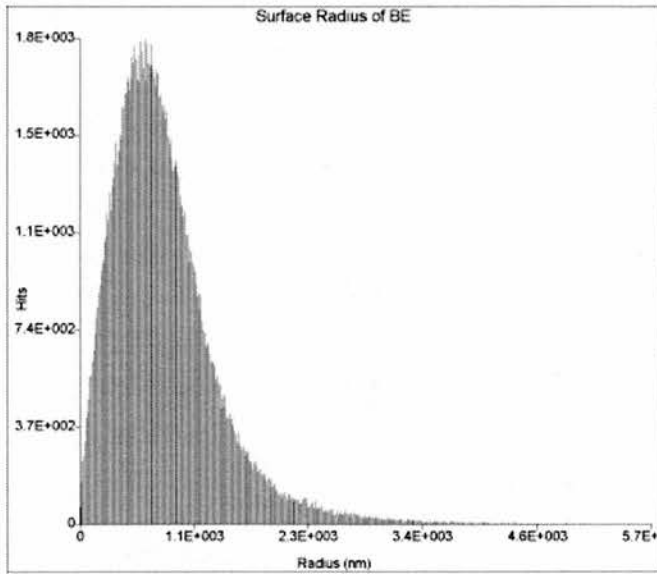


**Figure 4.5:** Lateral distribution of backscattered electrons from an 20 KeV electron beam. The distribution indicates that the range over which the proximity effect is evident.

Due to the fact that the back scattering mechanism is closely related to the density of the materials with which the electrons interact, the range over which the proximity effect is evident varies depending upon the acceleration voltage and material composition. For the material structures used for this project, the effects of proximity could be observed at ranges up to  $3 \mu\text{m}$  from the point of impact. The dose associated with this distribution is assumed to have the same form with respect to the radius  $r$ . The lateral range of backscattered electrons increases linearly with the acceleration voltage (EHT). Figure 4.6 plots the ranges of the peak density of the distribution and the maximum range scattering can be observed as a function of acceleration voltage. At 20 KeV exposure from the proximity effect has a peak at just under  $1 \mu\text{m}$ , but may contribute to exposure occurring at distances up to  $5 \mu\text{m}$  from the desired point of exposure.

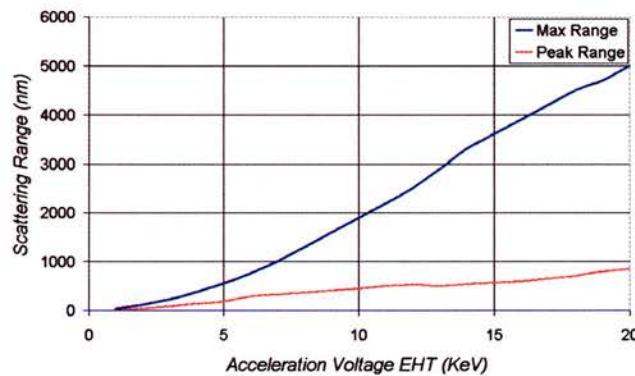


**Figure 4.6:** Plot of the peak (red) and maximum (blue) ranges of the backscattered electrons from an 20 KeV electron beam.

### Proximity Effect On Dense Structures

Possibly the most challenging aspect of my work was the creation of the 1-dimensional and 2-dimensional gratings, also known as 2-D Photonic Crystals. During the patterning of such tightly spaced ‘holes’, the proximity effect was found to be most evident. Figure 4.7 demonstrates the result of a typical exposure. The writing process can clearly be seen to fail after only four periods

of the crystal. This is a prime example of the proximity effect in operation. The summation of individual back-scattered contributions from up to 5  $\mu\text{m}$  away is enough to effectively destroy the pattern.

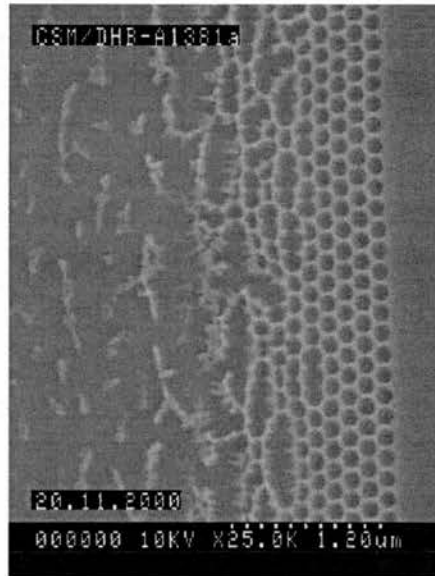


**Figure 4.7:** The proximity effect on photonic crystal structure. It is evident that after four periods of the crystal, the magnitude of the backscattering components and base exposure dose has grown large enough to exceed the PMMA exposure level.

The dose delivered/received at any given point is given as the base dose plus the summation of contributions from back-scattering events at every other point in the back-scattering range.

$$D(r_i) = \sum_{j=1}^m \int_{A_j} D_j p(r_{ij}) dA_j \quad (4.5)$$

where  $m$  is the index of the contributing area. Figure 4.8 highlights the effect of intra and inter pattern proximity effect. Clearly from Figure 4.7, back scattering from individual elements of the pattern are causing an inter-pattern proximity effect. The proximity effect is the combined result of inter-pattern proximity exposure and intra-pattern proximity effect.

While exposure due to the proximity effect tends not to play a significant

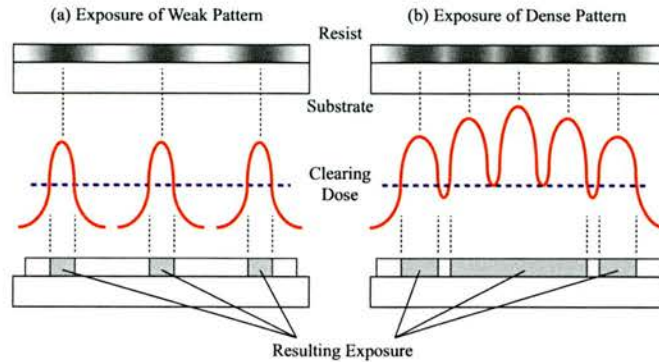


**Figure 4.8:** Depiction of the proximity effect and its influence on patterns containing densely packed features. On patterns with sparse features (a), the effect is slight. Over exposure is mainly an intra-proximity effect. While a dense pattern experiences inter-proximity between features of the pattern.

role in large features with feature-to-feature spacing of the order of 10's of  $\mu\text{m}$ , once the distance between adjacent features reaches 10's of nm, this proximity effect leads to the deterioration of the pattern definition.

Proximity Correction is important for two reasons, the first is that dimensions of the fabricated device must be equivalent to those of the pattern. This is especially critical in photonic crystal work, where slight changes in the structure of the holes can lead to shifting in the bandgaps. The proximity effect is not a constant factor operating equally on all pattern features, but a constantly varying factor. The proximity effect adheres to few rules, but intuitively one can expect the 'corrected' dose to increase at a) the pattern edges and b) where the density of pattern features increases. Towards the centre of patterns, dose falls to its minimum value. The second reason relates to the post-patterning stages of the work. Patterning of thin films is usually conducted as a single stage in a much longer process. In this work, the patterned resist was used as an etch mask for the selective removal of underlying film. If uncorrected, the proximity effect effectively opens larger windows towards the centre of a pattern. Any further processing by dry etch techniques results in features where a deeper etch depth can be obtained. When considering the proximity effect on a 1-D grating, if uncorrected, the depth of the gratings towards the edge of

the structure are generally shallower than those in the centre, a sure indication that the openings in the resist are largest at the centre of the pattern. This could lead to increased optical losses due to mode stripping into the substrate layers.

### **Proximity Correction Methods**

Correction for the effects of the back-scattered electrons has been attempted using various methods. The most successful of these are based around either manipulation of the pattern dimensions to compensate for envisioned problems in the exposed layer, alternatively the scaling of the exposure dose to ensure that the average dose per unit area experienced by the pattern is held constant.

### **Pattern Biasing**

Correction for the proximity effect can be achieved by direct manipulation of the exposure pattern. Biasing the pattern in such a fashion as to prevent or control the effects of proximity necessitates great knowledge of the overall design, exposure and development processes. Figure 4.9, taken from [117] demonstrates the result of employing effective pattern biasing. The figures on the left demonstrate the desired pattern (top) in the form of the mask design and the obtained result (bottom). Attention is drawn to the distance between the parallel paths of the resulting pattern which can be seen to almost merge.

Modifications to the mask design are illustrated in the upper right quadrant of Figure 4.9. Attention is drawn to the use of 'cut-outs' and 'fillets' which act on the paths and pads which make up the pattern. The resulting resist profile is presented in the lower right quadrant, clearly demonstrating the improvements achievable by correct biasing of the pattern.

### **Ghost Masking**

In the Ghost Masking method, correction for the proximity effect occurs before the desired pattern is written. Using the inverse field (also known as the clear-field or positive) of the desired pattern, the inverse pattern is exposed with a lower dose than the clearing dose. The clearing dose is specified as the

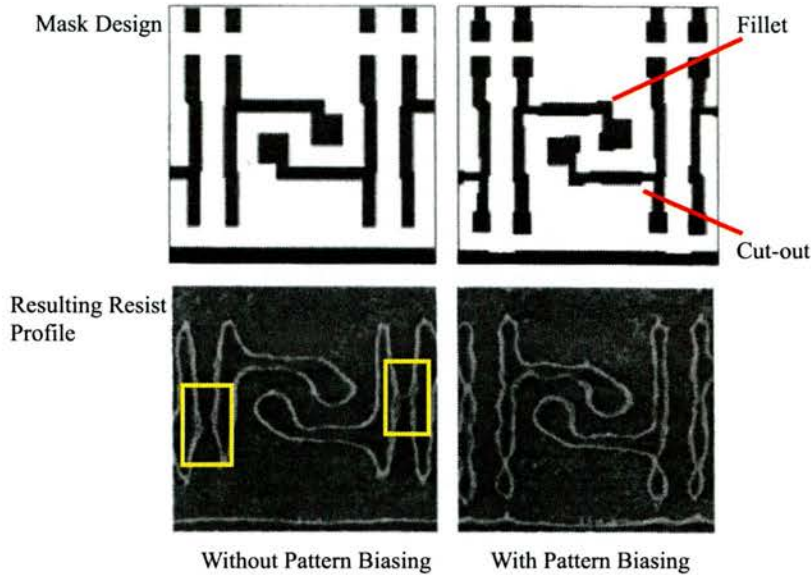


**Figure 4.9:** Proximity correction by means of physically modifying the desired pattern, such that the post exposure result more closely follows the original pattern. Courtesy of [117].

minimum dose required for complete exposure of the PMMA layer. Figure 4.10 illustrates the basic procedure for this method of proximity correction. The exposure profile (Figure 4.10(a)) contains the forward and back-scattered contributions to the proximity effect.

The exposure of complex patterns (Figure 4.10(b)) leads to an overall exposure profile (indicated in red) significantly greater than that of the desired pattern indicated by the black lines. Any exposure which exceeds the PMMA clearing dose threshold (indicated by a blue dashed line) leads to a deterioration in the pattern.

By pre-exposing the sample using the inverse of the pattern with a lower exposure dose than the clearing dose, the sample is provided with a corrected background exposure as illustrated in Figure 4.10(c). The desired pattern is then exposed with a much reduced dose which leads to an overall result indicated by the red line of Figure 4.10(d). Using this method over exposure and the proximity effect are minimised. The key advantage of this correction

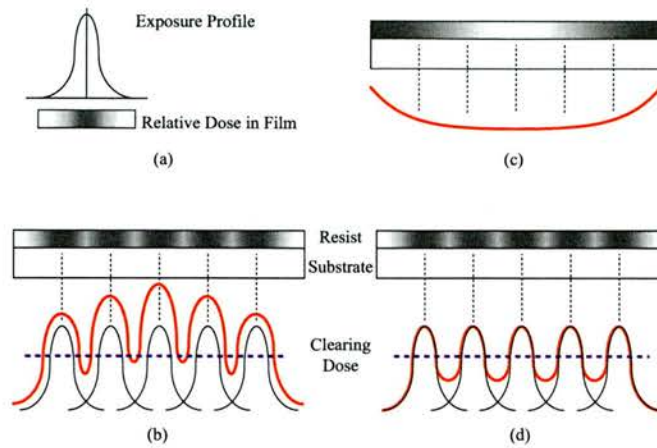


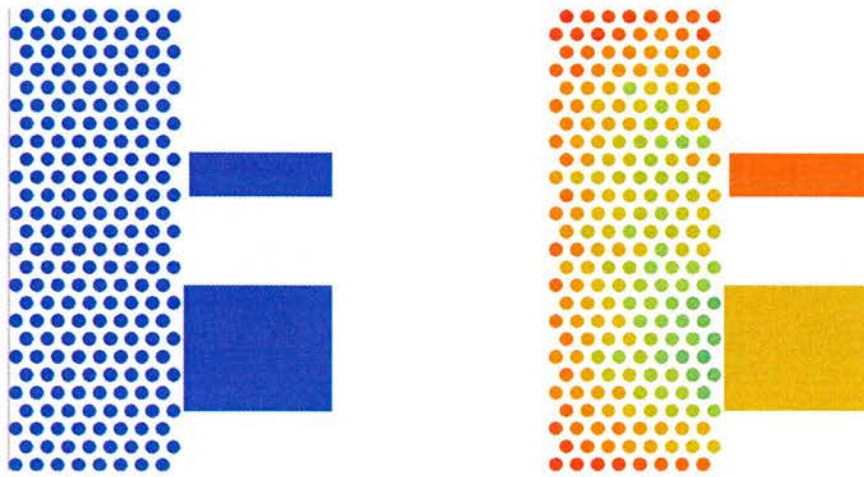
**Figure 4.10:** Mechanism behind the Ghost exposure approach to correcting for the proximity effect.

method is that no computation is required. Due to the fact that Ghost Masking does not require a significantly high accuracy, therefore exposure is usually conducted using a defocused beam.

### Dose Scaling

A third method, and the approach adopted by the majority of equipment manufacturers, is to vary the exposure dose received by the ebeam resist by adjusting the dwell time of the electron beam. Initially the desired pattern is broken up into small polygons (either trapezia or squares), each of these polygons becomes an element of the pattern requiring an individual dose. Next, the dose assigned to each of these polygons is calculated using an iterative method. The designated dose for each polygon comprises contributions from that polygon's own exposure in addition to the secondary back-scattering contributions from adjacent polygons. Figure 4.11 illustrates the result of the dose scaling method of correcting for the proximity effect. In general the dose is reduced in the central areas of the pattern while the area at the pattern extremities are allotted a higher dose.

In order for the dose scaling correction method to work, the exposure parameters, the ranges of the scattering mechanism and the operating parameters



(a) The basic pattern without any proximity correction. (b) Plot of Dose and Radius where inner resist remains

**Figure 4.11:** GDSII patterns with and without the application of dose scaling proximity correction. Blue/green indicates dose assignment from the lower part of the range, while orange/red indicates doses from the upper end of the range.

describing the beam must be described accurately. First approximations to the  $\alpha$ ,  $\beta$  and  $\eta$  parameters can be determined by using the Monte-Carlo techniques explained earlier as a starting point. Refining the parameters can be achieved by performing an exposure test on sample material.

Of these methods, that of scaling the dose to write the pattern with a dose sufficient to clear the resist layer is the most common, and was used extensively throughout my project. The main disadvantage of this method of correction is the amount of computing power required for the correction of large patterns.

### Determination Of Correction Parameters

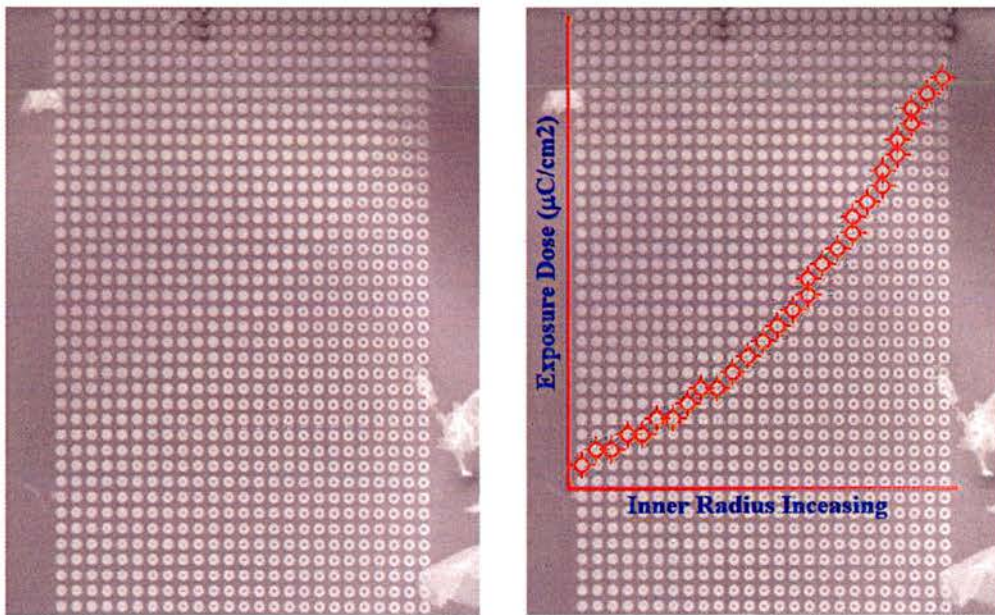
The method for determining the correction parameters involves the creation of an exposure test pattern. A simple ring pattern with fixed outer radius and varying internal radius is chosen as the pattern element. A large array of these doughnut are written on a test sample of the material to be patterned, with the internal radius of the ring increasing along the horizontal axis, and the applied dose increasing along the vertical axis. In such a pattern the magnitude of the dose experienced in the center of each ring is given by integrating the individual

contributions from around the ring. This value is described by Equation 4.6.

$$D_{center} = 2\pi D \int_{R_1}^{R_2} r \cdot p(r) dr \quad (4.6)$$

where  $R_1$  and  $R_2$  are the internal and external radii of the ring and  $D$  is the assigned dose.

The resulting pattern is shown in Figure 4.12(a). Observation of the exposure test after development reveals that as the internal radius is increased there is a point where the effect of back scattering ceases to cause the over exposure of the internal annulus. Naturally the radius at which this occurs is different for each dose tested. The next step in determining the correction values is to collate the combinations of dose  $D$  and internal radius  $R_1$  for which the above condition applies.



(a) The developed 'doughnut' pattern. (b) Plot of Dose and Radius where inner resist remains

**Figure 4.12:** Pictures of the 'doughnuts' pattern after development (left). Where the inner post of the doughnut remains, the combination of values for the exposure dose and inner radius indicate the extent of the proximity effect.

Figure 4.12(b) is a plot of the combinations of dose and internal radius for which the proximity effect is small enough to leave the centre of the doughnut intact. Using a data analysis package, the plot of  $D_0$  and  $R_1$  can be used to determine the  $\alpha$ ,  $\beta$ ,  $\eta$  and the optimal clearing dose by fitting Equation 4.7 to the curve of Figure 4.12(b) [118, 119].

$$D = \frac{D_0 \cdot (1 + \eta)}{e^{-\frac{R_1^2}{\alpha^2}} + \eta \cdot e^{-\frac{R_1^2}{\beta^2}}} \quad (4.7)$$

Table 4.1 presents the application of this method to typical pattern and material pairing gives the following output values for the proximity corrected results.

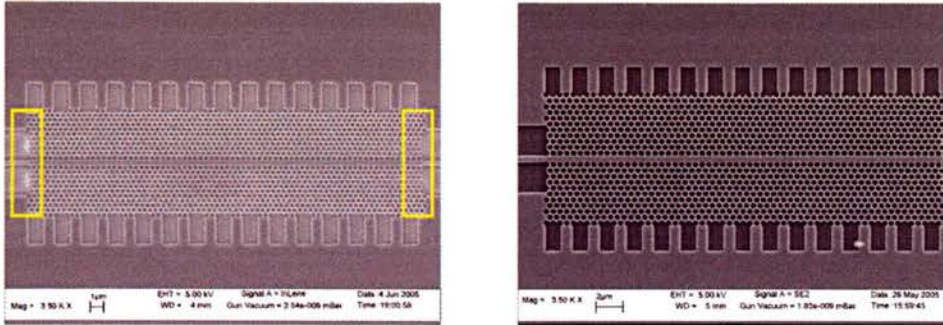
**Table 4.1:** Table of proximity correction parameters for stage 3 designs

Parameter	Coefficient	Description
$\alpha$	0.001	Forward scattering parameter
$\beta$	4.177	Backward scattering parameter
$\eta$	0.779	Ratio
$D_0$	132	Optimum base dose

#### 4.3.4 Development

The completed sample must be developed in order to remove the areas of the PMMA film which have been exposed to the high intensity electron beam. Two development processes were investigated. The standard process is based on the dilution of methyl-iso-butyl-ketone (MIBK) with iso-propyl alcohol (IPA) at different concentrations. Optimal results for the development stage were found to occur with an MIBK:IPA ratio of 1:2.5. For this developer the temperature of the solution is found to play a significant role on the development processes. The standard procedure was to maintain the temperature of the solution at 23 °C during the 30 second development time. This is the standard process at Glasgow University, from where it was adopted.

The second method of pattern development is based purely on the use of IPA and reverse osmoses (RO) water. A solution of 3:7 parts water:IPA was



(a) Photonic crystal waveguide without proximity correction applied. (b) Photonic crystal waveguide with the proximity effect corrected for..

**Figure 4.13:** Examples of proximity correction on the same pattern. On the left to interface between the standard waveguide and photonic crystal waveguide demonstrates that the crystal has experienced proximity effect. It has received over-exposure from the large blocks used to define the lead-in waveguide. On the right, the proximity effect has been corrected for and the crystal exists without deformation. SEM photos courtesy of Liam O’Faolain.

found to be sufficient to remove the exposed PMMA. The advantage of this method over the former lies with the need to accurately control the temperature of the solution. For the MIBK:IPA solution, increases in development rates of up to 5 nm per second per degree centigrade have been experienced<sup>4</sup>. It has been reported elsewhere [120] that the use of water:IPA, compared to the conventional MIBK:IPA, as the developer for PMMA resist has shown an order of magnitude reduction in roughness.

Proximity Correction is important for two reasons.

The first is that dimensions of the fabricated device must be equivalent to those of the pattern. This is especially critical in photonic crystal work, where slight changes in the structure of the holes can lead to shifting in the bandgaps. The proximity effect is not a constant factor operating equally on all pattern features, but a constantly varying factor. The proximity effect adheres to few rules, but intuitively one can expect the ‘corrected’ dose to increase at a) the pattern edges and b) where the density of pattern features increases. Towards the centre of patterns, dose falls to its minimum value.

<sup>4</sup>Private discussions with Steve Thoms, Glasgow

The second reason is related to the post-patterning stages of the work. Patterning of thin films is usually conducted as a single stage in a much longer process. In this work, the patterned resist was used as an etch mask for the selective removal of underlaying film. If uncorrected, the proximity effect effectively opens larger windows towards the centre of a pattern. Any further processing by dry etch techniques results in features where a deeper etch depth can be obtained. When considering the proximity effect on a 1-D grating, if uncorrected, the depth of the gratings towards the edge of the structure are generally shallower than those in the centre, a sure indication that the openings in the resist are largest at the centre of the pattern. This could lead to increased optical losses due to mode stripping into the substrate layers.

## 4.4 Pattern Transfer

While the patterning of the PMMA layer by electron beam lithography is relatively straightforward and widely used, the use of this polymer based layer as an etch mask is limited by the fact that the PMMA is not very resilient against the physical bombardment of the plasma based processes normally used to etch the underlying dielectrics. The introduction of an intermediate sacrificial layer between the patterned PMMA and laser substrate permits the desired pattern to be transferred on the provision that the etch selectivity of the intermediate layer over the PMMA is high enough.

### 4.4.1 Reactive Ion Etching

The procedure of transferring the pattern from the PMMA to the  $\text{SiO}_2$  hard mask is achieved using a Reactive Ion Etching (RIE) process. The process of removing  $\text{SiO}_2$  using fluorine based etch chemistry is well understood. Using  $\text{CHF}_3$  as the source gas, fluorine reacts readily with the silicon in the  $\text{SiO}_2$  intermediate layer, forming the volatile  $\text{SiF}_4$  gas.

The process of dry etching in this manner takes place under low pressure conditions, typically around  $2.8 \sim 3.4$  mBarr. The basic mechanisms involved are depicted in Figure 4.14.

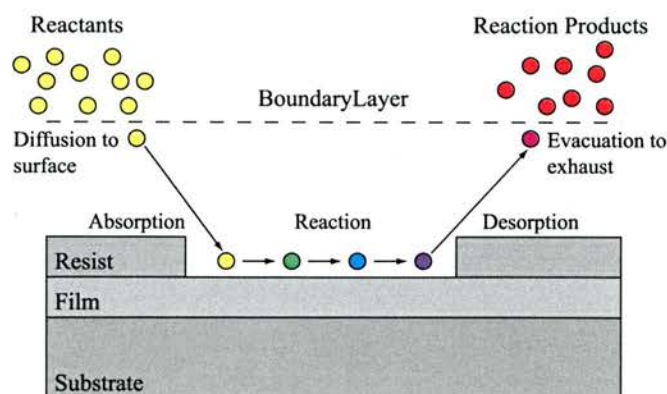
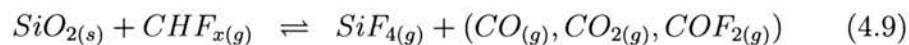
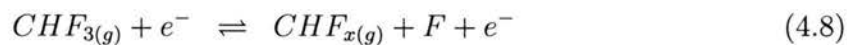


**Figure 4.14:** Schematic depicting the 5 stages of a dry chemical etching process.



Details of the calibration and characterisation of the chamber are presented in Table 4.2. The table lists the typical etch rates achieved during normal operation at various powers. The power used to remove the  $SiO_2$  is important to the quality of the final device contacts, as dry etch damage occurs due to the relatively high biases that need to be used.

**Table 4.2:** Operating parameters for the RIE process. Typical powers used, DC Bias values experienced and expected obtainable etch rates presented.

Power (W)	DC Bias (V)	Etch Rate (nm/min)
10	200	$\approx 10$
20	300	$\approx 16$
30	380	$\approx 22$
50	500	$\approx 40$
75	615	$\approx 65$

### 4.4.2 Chemically Assisted Ion Beam Etching

The etching of the GaAs/AlGaAs epitaxial multi-layers took place using an Ion Beam etching method. In the ion beam method, the plasma is generated in a separate chamber, known as a Kaufman ion source, and ions from this chamber are stripped and accelerated towards the sample using acceleration grids. Figure 4.15 shows the basic layout of the Ion Beam Etching plant used in my project.

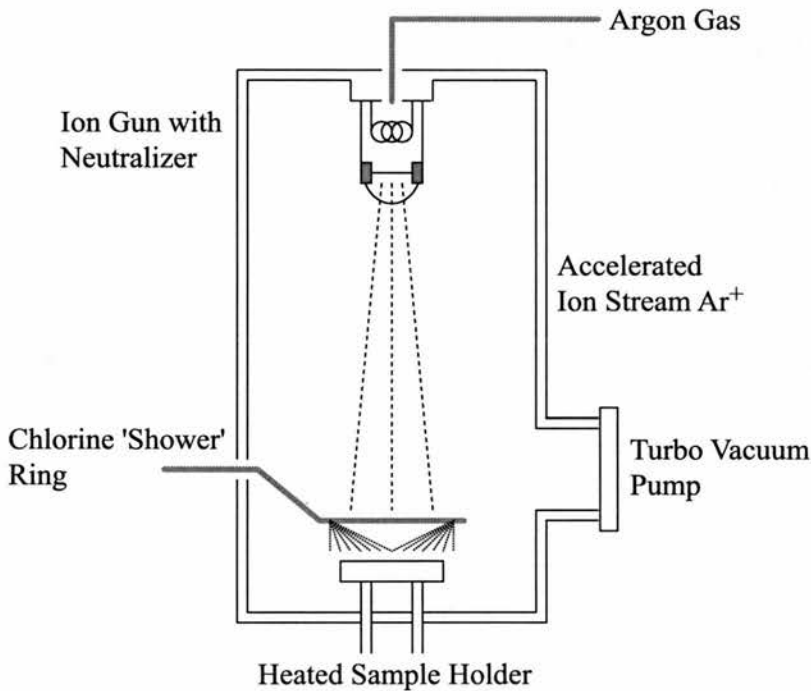
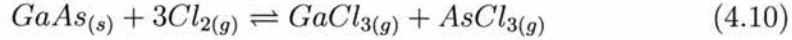
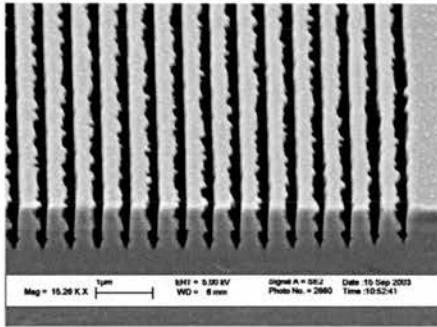


**Figure 4.15:** Schematic of the Chemically Assisted Ion Beam Etching equipment.

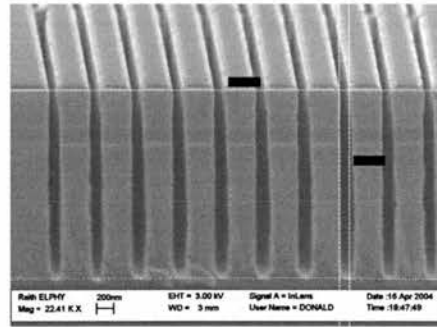
The gas used to generate the plasma is Argon, which constitutes the mechanical etching component of the process. The chemical assistance is offered by the introduction of a highly reactive gas, at or near the substrate surface. The choice of gas is primarily dependant on the dielectric material being etched. In the case of transferring a pattern from the Silica masking layer to the GaAs substrate high purity chlorine  $\text{Cl}_2$  is used.



Various factors influence the etch rates achievable with chemically assisted ion beam etching, the most important of which include the uniformity of the gas flow across the wafer. Initial trials with a simple pipe bleeding the chlorine into the chamber produced a variety of results, essentially the etch depth of samples was found to vary significantly over short distances from the pipe end. In an effort to improve the etch uniformity the pipe was replaced by a ring which ‘showered’ chlorine onto the sample holder in a more uniform fashion. A second factor which was found to influence the uniformity of the etch was the alignment of the Kauffmann ion source. During routine maintenance, the source is removed from the chamber and service performed. Upon replacement it was found that slight misalignment caused the movement in the ion beam profile and is strongly suspected to be responsible for the irregular etching of the side wall in grating etch runs.



(a) SEM of an irregular CAIBE etch. Notice that only right hand side of the slots demonstrates damage.



(b) Improved CAIBE etching results. The slight bowing of the slot into a cigar shape is the result of a slight over-chemical etching.

**Figure 4.16:** Examples of grating profiles from the same CAIBE equipment. It is strongly suspected that the problem was related to the gun alignment. High energy  $\text{Ar}^+$  ions ricochet from the mask may have caused the deterioration in the vertical facet of the slot. On the right, results from the same material, and equipment demonstrate the near perfect 114 nm slots, with depths of 2  $\mu\text{m}$ .

A third significant factor governing the etch rates and etch profiles of

CAIBE etching is the removal of non-volatile by-products from the sample surface. During etching argon ions from the ion beam source are accelerated to the sample surface, gaseous species from the plasma react with the surface atoms forming compounds or molecules. These species leave the surface as a direct result of the argon ion bombardment. The dislocation of the spent reactants can be assisted with the use of a heated sample holder. The application of heat to the sample during etching assists in the removal of the non-volatile chemical by-products of the reaction and prepares the exposed surface for fresh reactants. To this end the construction of a efficient heating stage was also conducted during the early trials of the CAIBE system.

Characteristically, there is a trade off between the Physical (argon ion) and Chemical (chlorine gas) etching components. While the chemical etching component acts as an isotropic etch mechanism, creating a balloon type etch profile, the physical etching component provides an element of anisotropy, imparting directionality for the etch mechanism. True vertical etching is achievable for a a very select etch conditions.

## 4.5 Coupled Cavity Laser Fabrication

The fabrication of coupled cavity lasers relies heavily on both e-beam lithography and dry etch technologies. The III-V material base chosen for this project was the GaAs/AlGaAs material pairing. Ultrathin layers formed from 75 Å strained InGaAs layers provides a high emission efficiency quantum wells operating around a wavelength of 980 nm. The emission efficiency of InGaAs quantum wells in conjunction with the wealth of information regarding the processing of the GaAs/AlGaAs material base are the two main reasons for the structure choice. In this section, the stage-by-stage fabrication of coupled cavity lasers is discussed.

### 4.5.1 High Resolution Electron Beam Lithography

The first stage of the fabrication process is the definition of the Inter Cavity Reflectors, the 1-dimensional Bragg reflector and all alignment and registration

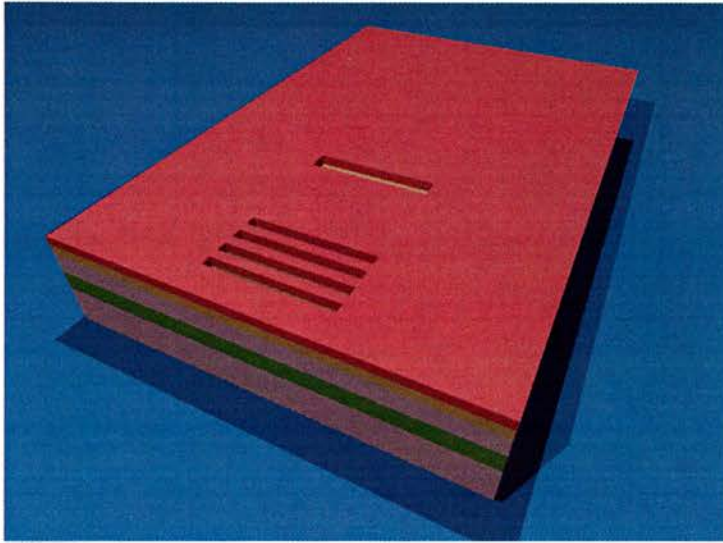


**Figure 4.17:** Stage 1: defining the high resolution features in PMMA layer.

markers. The sample with the  $\text{SiO}_2$  layer is spin-coated with Ebeam resist. Electron beam lithography is used to write the sub  $\mu\text{m}$  features into a 200 nm thick layer of either 4 % Elvacite or 4 % 950 K. The resist is spun on at 5,000 rpm in two stages with a 45 minute bake at 180 °C between each layer application. The exposure of features in the PMMA resist occurs with an electron beam dose of approximately  $140 \mu\text{C}/\text{cm}^2$ . Development of the exposed layers is achieved using either 7:3 IPA to RO water or 2.5:1 IPA to MIBK solutions. At this stage, careful examination of the sample surface reveals very small gratings and alignment markers, these have been exaggerated in the Figure 4.17 for effect.

#### 4.5.2 Deeply Etched Bragg Reflectors and ICR

The second stage of fabrication, depicted in Figure 4.18, represents the transfer of the pattern in the PMMA to the semiconductor. As previously explained, this is a two step process, the first step is the pattern transference from the PMMA to the silica intermediate layer.

To achieve this RIE is conducted using  $\text{CHF}_3$ . The flow rate of the  $\text{CHF}_3$

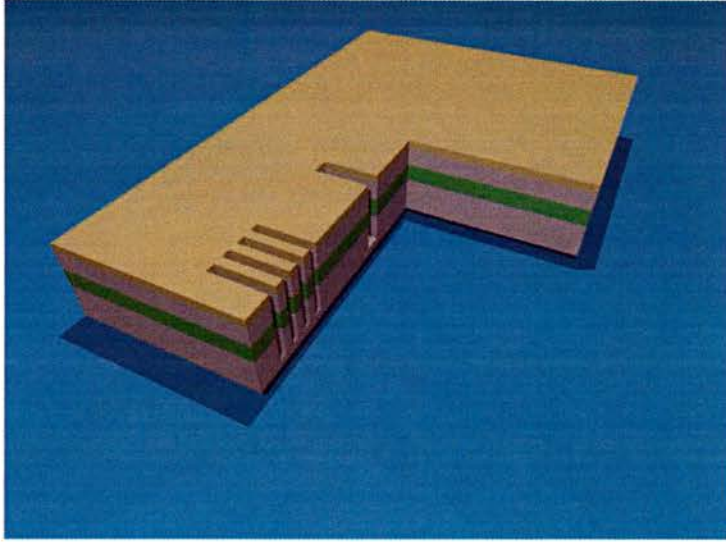


**Figure 4.18:** Stage 2: dry etching is used to create deep features in the substrate.

was set for 2 standard cubic centimeters (SCCM) and the power of the RF generator set for 33 Watts. Etching for 12 minutes is found to be sufficient to etch the 200 nm of  $\text{SiO}_2$  layer, while not completely removing the PMMA. The second step is to transfer the pattern from the silica into the GaAs. This is achieved using CAIBE etching with 10 SCCM of Argon and 4.7 SCCM of chlorine. The IBE controller settings used to achieve this deep etch are 1350 Volts accelerator voltage, 11.5 mA beam current and 35 Volts beam voltage. The cut-away view in the figure gives an indication of the structure on completing this stage.

### 4.5.3 Waveguide Ridge Definition

The third stage is the creation of the laser ridge, which employs the use of the negative acting SU-8 resist. The first step in defining the waveguide ridge is to remove any residual resist and  $\text{SiO}_2$  hard mask. The sample is spun with a layer of PMMA ebeam resist, following the usual recipe.

Using alignment markers etched during the previous stages of fabrication, a second layer alignment is performed and ridges in the SU-8 defined. Defin-

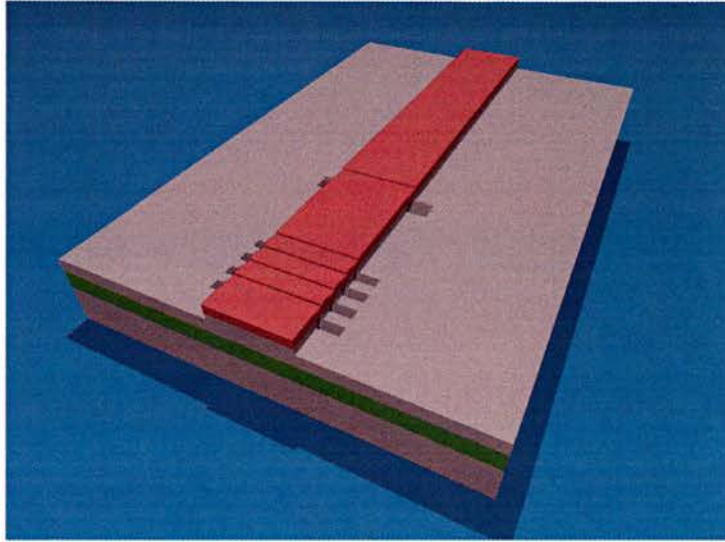


**Figure 4.19:** Stage 3: SU-8 used to define the waveguide ridge.

ing the ridges in this manner reduces the alignment errors experienced by the optical lithographic processes. The SU-8 layer functions as a negative acting, as discussed in Section 4.3.2, and has been found to provide an excellent etch mask against the dry etching processes used to obtain the 350 nm etch depth necessary for the ridge definition (cf. Figure 4.19). The ridge etching process was conducted using the CAIBE operating with settings of 350 Volts accelerator voltage, 7.5 mA beam current and 35 Volts beam voltage. Removal of this resist was conducted using an Oxygen plasma in the RIE.

#### 4.5.4 Electrical Contact Isolation

Electrical isolation of the laser ridge, the fourth stage in the fabrication process, can be achieved in a number of ways. Of the many methods investigated, two main methods provided very good results. The first method, illustrated in Figure 4.20, was to remove the remaining SU-8 layer from the previous stage using an oxygen plasma, re-spin the substrate with a thin fresh layer of SU-8 and then use a reflow method to reopen the ridge tops.

It was found that if the sample was heated to around the glass transition

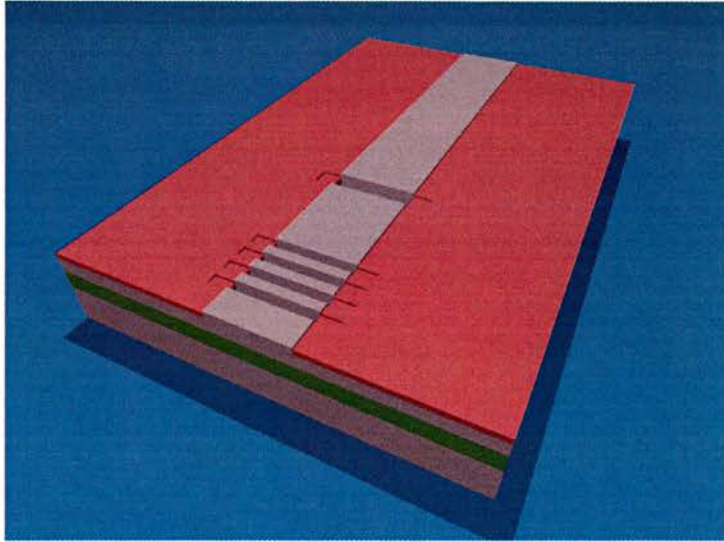


**Figure 4.20:** Stage 4: contact to the laser ridge is maintained while the surrounding areas are electrically insulated. The reflow method of clearing the laser ridge was found to be subject to irregular results.

temperature for SU-8, the surface tension of the SU-8 film caused to relatively small amount of SU-8 residing on top of the laser ridge to be ‘pulled’ into the body of SU-8 residing in the trenches, leaving the ridge surface clear for contact. A brief exposure to an oxygen plasma, ensures that the ridge top is free from SU-8, followed by a 10 minute bake at 200 °C to cure the layer.

In the second method, illustrated in Figure 4.21, a thick layer of photo resist was substituted of the SU-8 in the previous fabrication stage. The patterning of this photoresist to leave ridge strip was conducted using the standard photolithographic process. After etching the ridge, the residual resist was used as a mask for a lift-off process where Titanium Oxide was evaporated over the sample surface. The ability to create and subsequently back fill the areas adjacent to the ridge in this manner proved very useful with ensuring that current was directed through the laser. With the  $\text{TiO}_x$  ensuring electrical insulation to the ridge edge, the self alignment technique was completed by using a thick layer of SU-8 as a blanket insulator for the contact pads. Hard baking this layer to 200 °C ensures cross-linking occurs

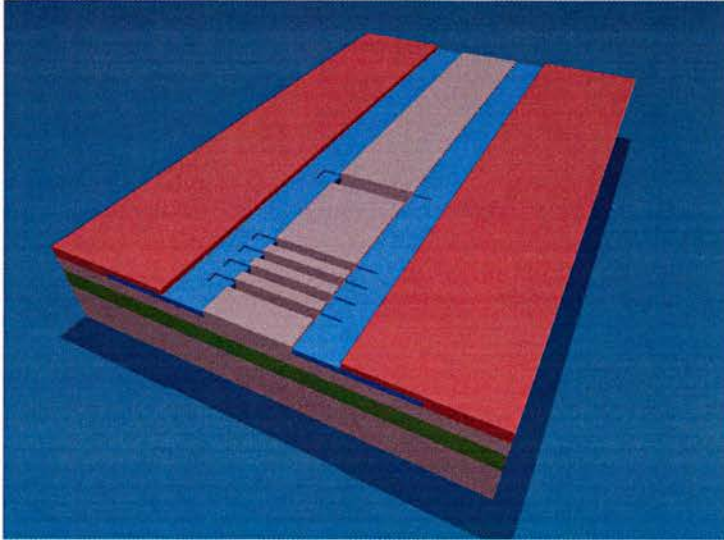


**Figure 4.21:** Stage 5: the second method utilised a self alignment technique for the ridge and insulator. The key modification with this method is that the polymer insulating layer (red) stops at a distance from the laser ridge (grey). This leads to a relaxation in the alignment tolerances of the multilayer masks used.

#### 4.5.5 Electrical Contact Deposition

The final stage of device fabrication is the creation of contacts. Contact deposition involves the use of a lift-off technique. First the sample is spun with LOR-7B at 6000 rpm for 60 seconds. The LOR material is one of a series of polymer based resins similar to normal photoresist, but has the photoactive compound removed. Given this, LOR-7B is impervious to either UV or Electron Beam exposure methods, but is however readily developed by the standard developer solutions used for normal develop. The rate of dissolution of LOR-7B can be controlled by the temperature and duration at which the samples is baked after spinning, typically this was for 2 hours at 180 °C. Subsequently a layer of Shipley S-1805 photoresist is applied at 5000 rpm and using optical lithography, contact windows are opened in the resist layer. During development the LOR-7B layer is found to dissolve in the developer, while the photoactive compound in the photoresist acts to maintain the exposed pattern. The result, shown in the figure, is an under-cut in the vertical profile of the



**Figure 4.22:** Stage 6: the side profile of LOR-7B layer and S1805 photoresist.

LOR/photoresist layers.

Deposition of the metal contact layers occurs using an electron beam evaporator. Once complete, the sample is submerged in acetone in order to remove the photoresist and hence the excess contact metallisation from the sample surface. Pre-processing the contact resist mask with a thin layer of LOR-7B eases the lift-off process by allowing the solvents direct access to the photoresist layer (cf. Figure 4.23). Without the sacrificial LOR layer, solvent penetration of the metal limits the process of lift-off. The LOR layer can be completely removed using either prolonged immersion in the solvents or alternatively a brief soak in standard developer solution.

## 4.6 Contact Characterisation

The operation of all electro-optic devices requires the efficient delivery of the carriers to the relevant active regions in the device geometry. Multiple thin layers of different metals are deposited through either evaporation or sputtering techniques. Generally, simply depositing a metal layer as a contact between

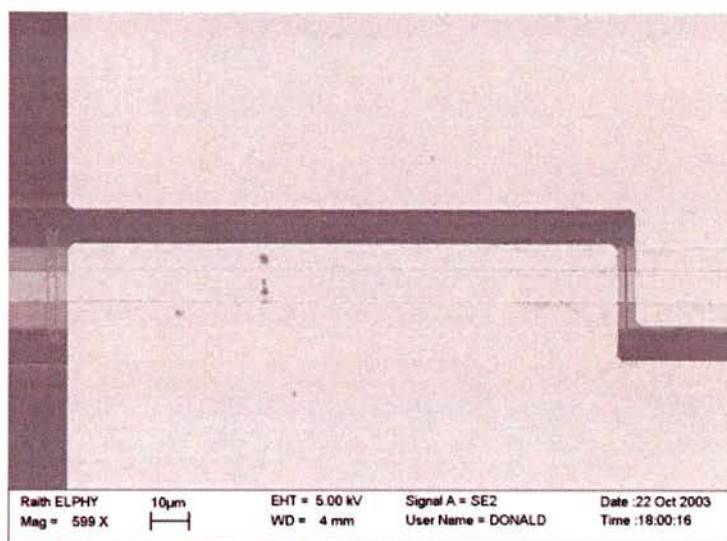


**Figure 4.23:** Stage 7: contact deposition and lift-off process leaves well shaped metal contacts over the laser ridge.

the metal and the semiconductor results in a rectifying (diode) junction rather than an ohmic (resistive) junction. The complexities of creating suitable low resistance ohmic contact junctions has been the focus of much research for many decades [121, 122, 123, 124].

The contact resistance, of the metal-semiconductor junction can be regarded as a parasitic voltage drop and should therefore be minimized. If conducted correctly, the deposition of thin metal contacts following the sequences outlined in Tables 4.3 and 4.4 offer contact resistances as low as  $0.1 \Omega \text{ mm}$  and  $0.2 \Omega \text{ mm}$  for n-type and p-type contacts respectively.

A potential barrier exists at the interface between the semiconductor and contacting metal. For the case of gold on n-type GaAs, the barrier height is 0.23 eV and for the p-type GaAs this height measures 1.19 eV. The existence of these barriers should effectively block the transit of carriers from the metal into the semiconductor. From quantum mechanics and the assertion of wave-particle duality, electrons can be described as possessing a wave-like nature. When the wave of the electron interacts with the barrier the electron is partially transmitted and partially reflected. This “tunnelling” of the electron through

the barrier is a statistical process and the probability of tunneling becomes high for extremely thin barriers where typical thicknesses are in the tens of nanometers. We make the barrier very narrow by doping it very heavily, typically  $1 * 10^{19}$  dopant atoms/cm<sup>3</sup> or higher.

Selection of materials for which these heights are small is the first stage on minimising the effect that these barriers have on the electrical characteristics of the contact. Annealing the contacts at temperatures up to 400 °C for a short period can create an alloy between the semiconductor and metal at the junction interface, which acts to lower the lower the magnitude of the potential barrier.

**Table 4.3:** Recipe for contacts evaporated onto a 100 nm layer of n-GaAs (doping  $10^{18}$  Si).

Material	Thickness	Deposition Rate	Crucible
Gold (Au)	11 nm	0.02	Graphite
Germanium (Ge)	11 nm	0.15 ~ 0.2	Al <sub>2</sub> O <sub>3</sub>
Gold (Au)	11 nm	0.02	Graphite
Nickel (Ni)	14 nm	0.1 ~ 0.12	Al <sub>2</sub> O <sub>3</sub>
Gold (Au)	150 nm	0.02	Graphite

**Table 4.4:** Recipe for contacts evaporated onto a 100 nm layer of n-GaAs (doping  $10^{19}$  Zn).

Material	Thickness	Deposition Rate	Crucible
Gold (Au)	11 nm	0.02	Graphite
Nickel (Ni)	11 nm	0.1 ~ 0.12	Al <sub>2</sub> O <sub>3</sub>
Gold (Au)	150 nm	0.02	Graphite

#### 4.6.1 Transmission Line Measurements

Measurement of the contact resistances are routinely determined using a process adopted from the field of millimeter waves [125]. The process of depositing contacts or performing transmission line measurements (TLM) on any given

wafer begins with the surface preparation. After thorough cleaning and de-oxidisation, the lift-off procedure is used to place several rectangular pads, the gap separation between adjacent pads increasing incrementally. Figure 4.24 demonstrates the pad arrangement and equivalent electrical circuit. The total resistance  $R_{tot}$  between adjacent pads is the culmination of the sheet resistance  $R_{S^*}$  and the total resistance incurred through making contact  $R_C$  with the substrate twice.

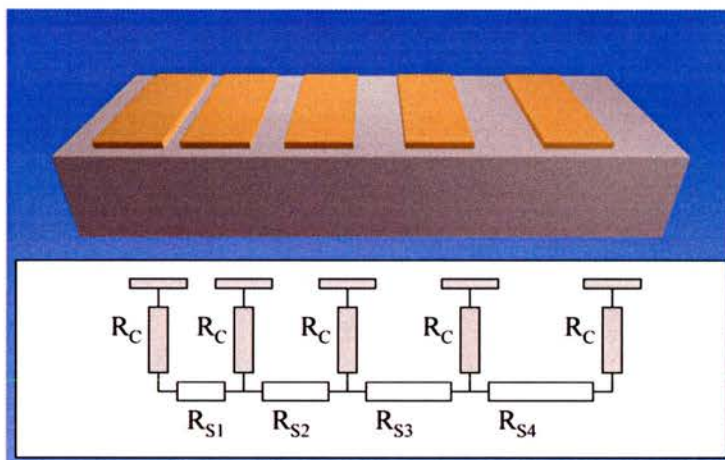


**Figure 4.24:** Schematic of a standard transmission line measurement contact pattern.

$$R_{tot} = \frac{R_{S^*}}{W} L_{gap} + 2R_C \quad (4.11)$$

where  $R_{S^*}$  is the sheet resistance of the semiconductor, which is assumed to be constant throughout the whole of the highly doped contact layer.  $W$  and  $L_{gap}$  are the contact width and gap length associated with the contact pads.

In determining the value of the contact resistance, two methods are available, the two-probe or the four-probe measurement techniques. The standard two-probe measurement technique is generally inaccurate for evaluating resistances of low values. The reason for this inaccuracy lies with the resistance between the probe tip and the contact pad being excessively high. The preferred four-probe technique, as illustrated in Figure 4.25, eliminates this uncertainty.

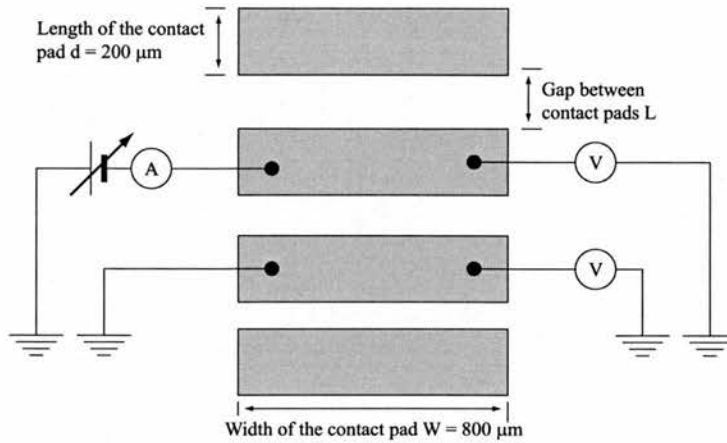


**Figure 4.25:** Four-probe measurement of the total resistance across the gap between 2 adjacent metal contact pads.

When the total resistance  $R_{tot}$  as a function of the gap separation  $L$  is plotted, the contact resistance  $R_C$  can be measured from the slope's intercept point with the vertical axis ( $L = 0$ ). The resistance value in ohms can be derived from the  $R_C$  is the resistance of the contact in ohms.

$$R_{tot} = 2R_c + R_s \quad (4.12)$$

#### 4.6.2 2 Probe and 4 probe Setups

Figure 4.26 demonstrates a typical result from this 4 probe measurement setup. As the name suggests, this method of measuring an unknown resistance uses four test leads. The first pair is used for the injection current, in this case across two adjacent pads, while the second pair is used for sensing the voltage across the resistor. This method results in more accurate measurements than the 2-wire resistance method and is recommended for measuring resistance below  $20 \Omega$ . The improved accuracy is achieved because the test leads that inject the current in the resistor cause a voltage drop, and this voltage is removed from the measurement path.

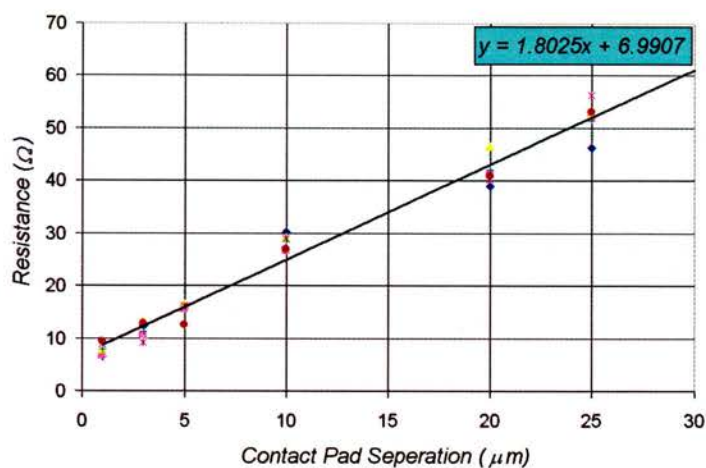


Figure 4.26: TLM results for the QT1719 sample.

### 4.6.3 Cleaving and Testing

The sample is cleaved by firstly scribing a small mark at the edge of the sample. The scribe mark provides a starting point for the cleavage line. Once initiated, the cleave occurs instantaneously along one of the planes of the crystal lattice. After cleaving the sample into laser chips, the chips are mounted on brass mounts using silver conductive paint.

# Chapter 5

## Device Evolution

### 5.1 Introduction

This chapter provides a brief account of the design aspects and realisation of the coupled cavity devices fabricated throughout the project. During the course of the project a variety of materials and fabrication techniques were employed and developed in the creation of the final device. Three main design iterations were conducted during the work, these are discussed in the following section where the key developments in the design iterations, advances in the fabrication techniques and the tangible results are discussed.

### 5.2 Coupled Cavity Laser Device Design

The overall design and key parameters of various aspects of the coupled cavity laser devices fabricated have been discussed in detail throughout the preceding chapters. The basic design with a view to the material and the device structure is presented in Figure 5.1.

During the course of the project, the design and fabrication of the coupled cavity lasers progressed through three major revisions. These design iterations were conducted in response to various difficulties and technical input from various sources. The overall design concept was based on making possible the future integration of a multi-cavity laser with passive functions.

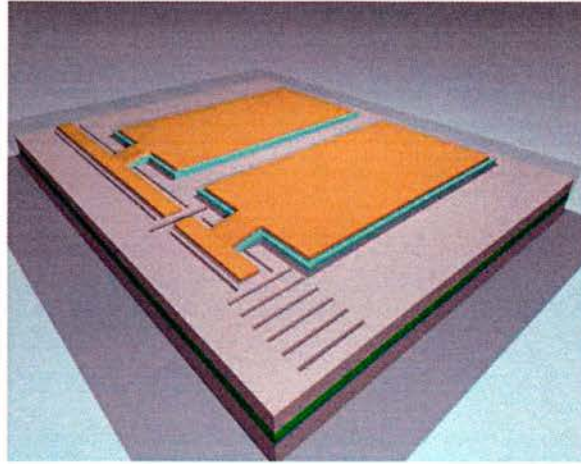


**Figure 5.1:** Conceptual schematic depicting the design for a monolithic coupled cavity laser. Key features of the design are the contact pads and bridges used to supply current to the individual cavities.

### 5.2.1 Towards Integration

The coupled-cavity laser configuration is essentially based upon the sub-division of a ridge waveguide into two or more shorter length laser cavities, separated by inter-cavity gaps. Traditionally, this division takes place by cleaving the ridge and re-mounting the individual segments onto a motherboard or recipient surface. Great care concerning individual segment alignment was required to ensure the desired separation was achieved. In this manner the creation of devices for which both cavities are electrically isolated, while optically coupled is achieved.

With a view towards integration, the process of forming and re-mounting the individual laser cavities onto a substrate of different material would be a laborious task, if achievable at all. Instead, the formation of the inter-cavity gap-lengths through dry-etching techniques was chosen. The monolithic integration of a coupled cavity device was achieved by dry-etching through the active region into the substrate to provide the electrical isolation. Electrical isolation of the driving currents,  $I_{\text{tun}}$  and  $I_{\text{las}}$  allows fine tuning of the optical path lengths of the cavities through differential pumping. While optical cou-

pling of the waveguide modes using deeply etched inter-cavity gap minimises the loss of the optical power through scattering of the mode into the substrate as discussed in Section 3.3.3.

The feedback mechanism for the cavities is provided by a standard cleaved facet for the lasing section of the device, while a short, deeply etched 6 period Bragg reflector was employed to provide feedback for the tuning section of the device.

## 5.3 Design Iterations

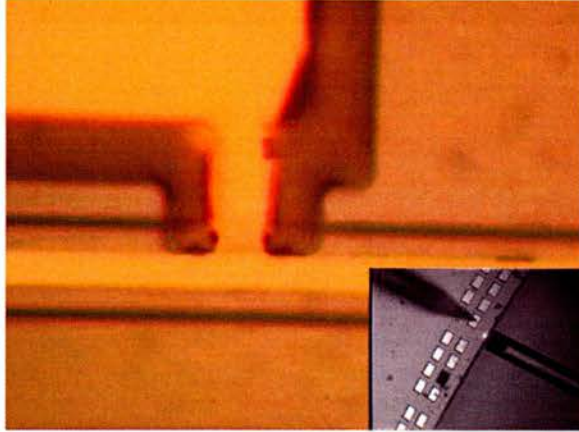
### 5.3.1 Design Stage 1

Figure 5.1 demonstrates a conceptual schematic of the initial design for the coupled cavity laser. Clearly visible are the two cavities of the laser, the shorter of the two defined by the Bragg mirror in the foreground and the ICR slot, is the tuning cavity while the other, longer of the two is the lasing cavity. Both cavities are pumped individually by probing the associated contact pad.

#### From Conception to Realisation

In formulating the initial design for the laser, the works of [126, 127, 128] were used as a starting point. Yuan *et.al.* reported threshold current values ranging from 4.5 mA for 100  $\mu\text{m}$  long lasers to 7.8 mA for 300  $\mu\text{m}$  long devices [128]. Modelled reflectivities of 93 % for a 2-period  $\lambda/4$  DBR to 0.66 for a 2-period  $5\lambda/4$  DBR were also reported. Höfling *et.al.* [126] investigated cavities with lengths down to 40  $\mu\text{m}$  and widths of 20  $\mu\text{m}$ . Here third order gratings (220 nm semiconductor, 740 nm air slot) proved to possess an effective reflectivities of 75 %. In this initial design the focus was on the creation of coupled cavity lasers following a long-short configuration. With this in mind, standardisation of the design by fixing the shorter cavity length to 20  $\mu\text{m}$  removed one of the variables from the initial layout.

The method of defining the laser ridge used in this initial design followed that of Krauss *et.al.* [127]. Here two parallel slots spaced at the ridge width



**Figure 5.2:** Photograph of the contact pad and insulator layer showing the sloping edge of the insulating layer. The interference pattern around the layer gives a measure of the slope gradient. *Insert:* Picture of the device under test, lasing is clearly visible at the cleaved interface.

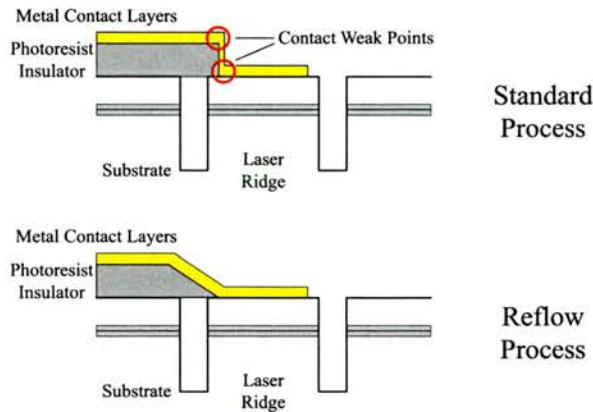
defines the waveguide ridge. Defining the waveguide ridge in this fashion permits the simultaneous creation of the inter-cavity gap, Bragg reflector elements and laser ridge definition in one processing stage. The waveguide width was chosen to be either  $3\ \mu\text{m}$  or  $5\ \mu\text{m}$ , while the width of the slots used to define the ridge were chosen to be  $1\ \mu\text{m}$ .

Figure 5.2 demonstrates the realisation of this initial coupled cavity design. The main picture is that of the small photoresist based support ‘bridge’ used to form a continuous contact from the contact pad (above and right) to the ridge contact (across figure). Clearly seen in the insert is a typical device from this generation of devices being probed. At the edge of the cleaved facet is a cylindrically lensed fiber used for capturing the laser’s output. The bright spot is the out of plane scattering at the output facet.

### Bridging the Gap

During the fabrication repeated attempts to bridge the gap between the contact pads and the laser ridge proved unsuccessful due to step-like profile of the insulating resist. The elevated height of the contact sitting on the insulat-

ing pad with respect to the ridge played a significant role in these difficulties. Evaporation of the metallic contacts over this step-like function creates weaknesses at the corner points of the contacting layer. To overcome this weakness, a process of reflowing the was developed. A commercially available image reversal photoresist (MicroChem) was used as an insulator. When exposed to elevated temperatures over approximately 120 °C, the layer becomes permanent, removable only by plasma etching. If, however the temperature of the resist layer is elevated to around the glass transition temperature, re-flowing of the layer occurs. Figure 5.3 gives a physical interpretation of this process. Experimentation with this technique permitted the creation of a sloped insulating ramp/slope from the height of the contact down to ridge level.



**Figure 5.3:** Vertical profiles of the insulating layer and contact metals from the contact pad to the laser ridge. Weak points on the profile for the standard process are highlighted, while the reflow profile demonstrates a contact with smooth vertical transition.

### Device Performance

Only a few devices constructed to this design demonstrated the expected performance. Lasers operated between 10's of seconds to a few minutes. Figure 5.4 demonstrates a typical device of this design after being subjected to drive currents in the milliamperage range, which clearly highlights contact burn-out due to local hot spot.

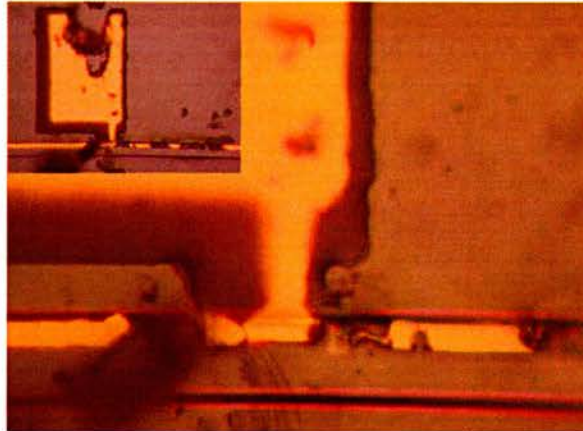


**Figure 5.4:** Photograph of device failure upon initial operation. Devices failed to operate for any significant period of time. *Insert:* Overview of the device depicting contact and insulating layer damage.

From the figure, while the structure of the contact bridge remains intact, contact failure is attributed to surface defects endured during the fabrication stages. One possible source of surface defects could occur due to mild etching of the surface through exposure to the developer solutions used in photolithography. Contact failure was the most common source of failure for this device design and was highlighted as the key point to address for this stage in the development.

### 5.3.2 Design Stage 2

For the second generation of the coupled-cavity lasers significant alterations of the initial design took place. Amongst the alterations, the use of narrow deeply etched trenches was abandoned in favour of a shallow widely etched design. The repercussions of this change on the design as a whole, prompted a complete re-design.

#### Shallow Trenches

Changing the method of ridge definition to a wide and shallow configuration reduces the effect of index guiding. For the overall design, the laser ridge width

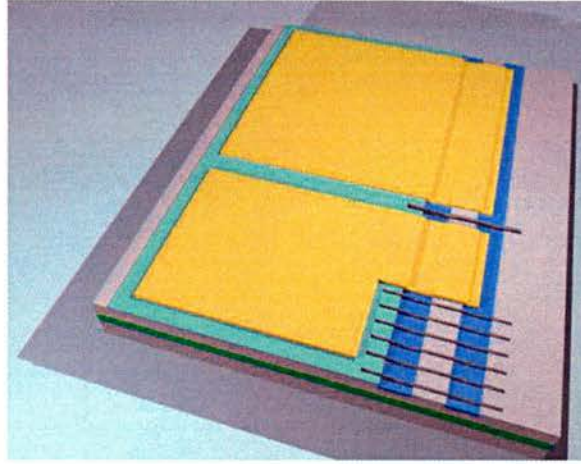


**Figure 5.5:** Conceptual schematic of the second design. Current revisions include the exchange of deep narrow slots for shallow wide trenches. Later revisions of the design incorporated the larger contact pads on either side of the ridge.

was maintained at  $3\ \mu\text{m}$ , while the width of the trenches was increased to  $20\ \mu\text{m}$  on either side of this waveguide ridge to maintain symmetry. The broader trenches were created in separate photolithographic and dry etch stages according to the principles of Section 3.2.2. As a consequence of this design change, the requirement of bridging deep trenches was no longer prevalent. The contact was designed to run almost the full length of the cavity. Figure 5.5 demonstrates the conceptual design of the second generation lasers incorporating the modifications.

The last significant change to the existing design was to reduce the density of the devices on the chip. In the initial design the contact placement was the defining factor for the placement of devices. The precedence was to reduce the contact area, while maintaining the ability to probe the device with relative ease. In changing the design, the foot-print width of the individual devices was increased from  $200\ \mu\text{m}$  per device to  $500\ \mu\text{m}$  per device.

### Implementing the Design

While electron beam lithography was the predominant method for producing devices following the stage 1 design; for the second design, elements of the

patterning were changed for implementation using photolithographic processes. The alignment tolerances for using photolithography are somewhat greater than that for Ebeam lithography. Figure 5.6 demonstrates the second stage design, where the modified contacts (indicated in yellow) are seen to run the full length of the laser cavities and completely cross the laser ridge (defined by the green lines).

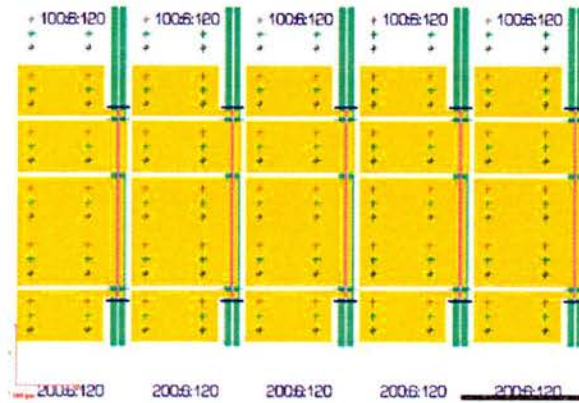


**Figure 5.6:** Design schematics for the second generation of devices. Small crosses indicate alignment markers used multilayer lithography. Source: Elphy32 design package.

In the second design a different polymer, SU-8, was introduced as material for the insulation layer. The SU-8 polymer can be exposed either optically or by using electron-beam lithography. The electron beam exposure dose required for this film is approximately 4 % of that for the standard positive acting PMMA resists, due to a higher sensitivity. The use of SU-8 in conjunction with photolithography results in the ability to expose large areas using short exposure times.

In addition to using SU-8 as a blanket insulating material a process of back-filling over etched trenches using titanium sub-oxides ( $\text{TiO}_x$ ) was conducted. With refractive index values of 2.2 being reported from similarly deposited films [129, 130], the effect of backfilling the trench proves advantageous in that the subsequent deposition of SU-8 or photoresist experiences a reduces step high from the insulating layer to the contact ridge. These features are

represented by the blue sections in Figures 5.5 and 5.8.

Figure 5.7 is an SEM image of the end facet from a laser constructed using in this design. The annotations indicate the laser ridge to the right of the image. The SU-8 contact insulation layer is clearly visible as the dark wedge like feature on the left side of the photograph. The  $\text{TiO}_x$  layer in addition to that of the various epitaxial layers making up the wafer are highlighted.

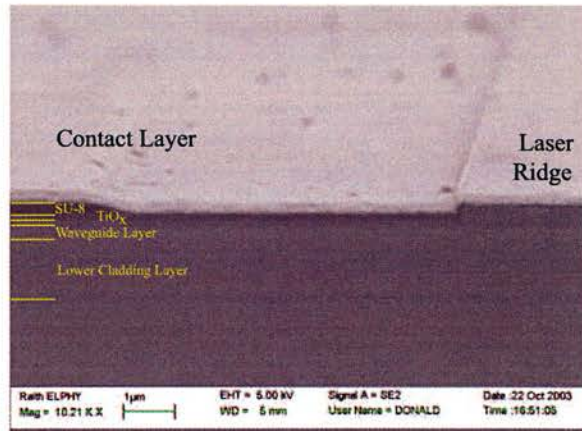


**Figure 5.7:** SEM image of the second stage laser end facet. Attention is drawn to the sandwiched insulating layer between the gold contact and substrate.

## Device Operation

The decrease in alignment tolerances, and formation of devices where high quality insulating layers exists right to the laser ridge, lasers with operating lifetimes greater than experienced during the initial work. The threshold currents typically obtained from devices formed to the second design are typically between 6 and 10 mA. The lasers created from this design demonstrated evidence of limited tuning.

### 5.3.3 Design Stage 3

In the third revision of the design, emphasis was placed on the creation of the long-long cavity configuration. With very few modification to the fabrication

process steps, the design outlined in Figure 5.8 was fabricated, demonstrating the third of the design iterations. Apart from the cavity length ratios the most significant changes for this design was the re-positioning of the contact pads.

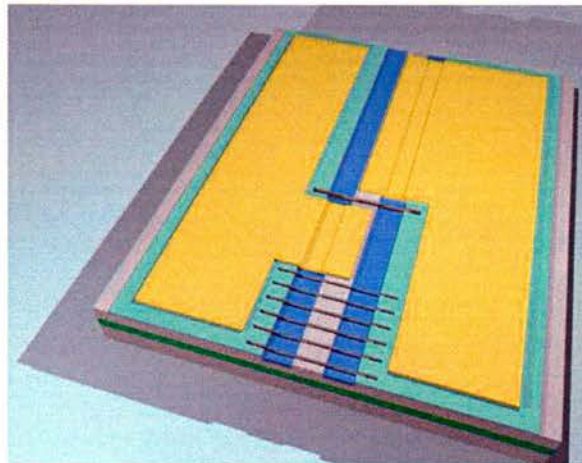


**Figure 5.8:** Conceptual schematic of the third design. Current revisions of the design incorporated the larger contact pads on either side of the ridge.

In order to increase device yield, a reciprocal device layout was introduced. In this layout two adjacent devices were placed back to back with the individual cavities effectively created as a single longer cavity. Figure 5.9 represents the realisation of this design after cleaving the devices into laser bars. Every cleaved laser bar possesses devices on either facet. This method of creating lasers offers twice as many devices per laser bar than previous designs.

Scribe marks can be seen on the right hand side of the chip, while cleavage markers (diamond shapes identifiers) can be seen forming a horizontal line between adjacent contact pads. During the cleaving process it is often the case that the cleave line will make it's own path across the wafer or chip. This is obviously dictated by the orientation of the crystal lattice planes. The accuracy of the cleaving process was found to be enhanced for chips which were thinned before cleaving. From Figure 5.9, the contact pads are obviously the gold coloured blocks while the green vertical stripes are the SU-8 insulating layers. Between these stripes lies the laser ridge.

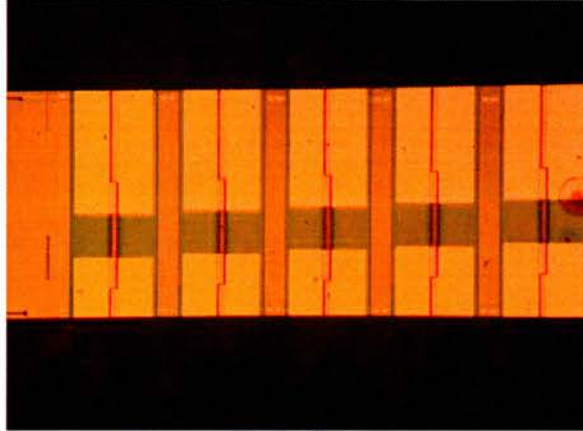


**Figure 5.9:** Typical bar of lasers from the third stage of design. Cleaving the laser bars to the correct lengths in a repeatable fashion proved to be difficult.

## 5.4 Device Summary

The fabrication of devices following the three design iterations provided significant experience and refinement of the techniques required for the creation of lasers and laser bars. Typically lasers grouped together forming laser bars of between 5 and 10 devices were created, mounted and tested. In addition to the active devices, waveguide ridges containing gratings were also fabricated and tested. Of the active devices created, those following the design specifications described in Section 3.4.2 provided the most interesting results. The results for shallow etched devices with cavities termed long-short and long-long are presented in the following chapter, where the tuning results range and operating characteristics are presented.

# Chapter 6

## Experimental Results and Discussion

### 6.1 Introduction

In this ‘experimental results and discussion’ chapter, the experimental methods used in determining the operating parameters and ranges of the coupled cavity lasers are outlined. Initially, a qualitative approach to the operation of the coupled cavity laser is presented with the key differences between the coupled cavity configuration and the single cavity device outlined. The main experimental setups and results from each are presented. The tuning range and side mode suppression ratio for a device operating in the single mode regime are then presented. Tuning curves constructed from individual wavelength scans demonstrate the effective tuning ranges of a typical device. The chapter concludes by relating the results obtained from the low current tuning experiments to the theoretically determined quantitative performance using the eigenvalue equation for longitudinally coupled cavity lasers.

### 6.2 Experiment

The experimental set-ups used for characterisation of the coupled cavity devices fabricated during this project is presented in Sections 6.2.1 and 6.2.2. The

standard electrical connection for testing coupled-cavity devices, is presented in Figure 6.1.

In this diagram, the longer of the two cavities, represents the lasing cavity, from which all optical measurements were taken. For the majority of experiments conducted the lasing cavity was operated in pulsed mode. Operating using a pulse source allows the manipulation of the pulse duty cycle, and therefore devices suspected to be influenced by (resistive) heating could be further investigated using shorter pulse duty-cycles. The pulse duty-cycle used in for testing routinely lay between 1 to 5 % of the pulse repetition period. The repetition periods typically lie in the region of 50 to 100  $\mu\text{s}$ . Operating the cavity in this fashion in addition to the heat dissipation provided by the sample mount prevented excessive heating of the sample.

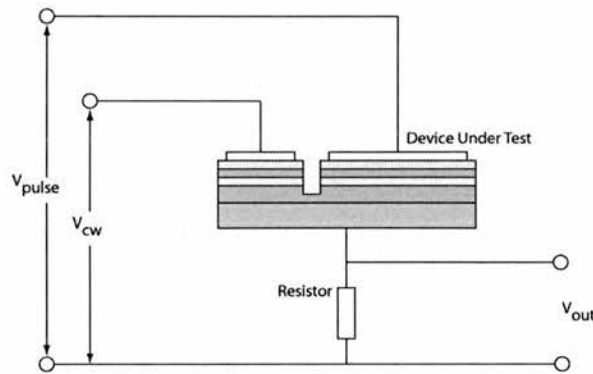


**Figure 6.1:** Schematic of a typical coupled cavity device under test conditions. The tuning cavity is pumped CW while the laser cavity is pumped pulsed with various duty cycles.

The magnitudes of the currents used to drive the lasing sections in the experiments were selected to lie just above the experimental threshold value for the cavity. Under standard characterisation, three sets of measurements were taken for each device tested. The threshold currents were found routinely be between 6 and 9 mA. To this end three different drive current values for the pulsed lasing section were chosen (10 mA, 15 mA and 20 mA) and characterisation conducted.

The shorter cavity is operated as a conventional CW laser, although every

effort to maintain the operation of this cavity below threshold is made. A standard Agilent DC power supply capable of incremental current steps of 1 mA is used to scan the ‘tuning’ current injected into this cavity from 0 mA to either 20 to 30 mA. The effect on the output wavelength from the lasing section as a function of current injection into the tuning cavity was observed.

The optical output of the device was captured using either a cylindrically lensed single mode (SM) fiber where available, a cleaved SM fiber butt coupled against the output facet or alternatively a microscope objective is used to focus the output onto a Germanium detector.

### 6.2.1 Light/Current Measurements

The technique of Light/Current measurements are used to determine the threshold current values for semiconductor laser cavities. The experimental set-up used to conduct the optical characterisation of the fabricated devices is demonstrated in Figure 6.2.

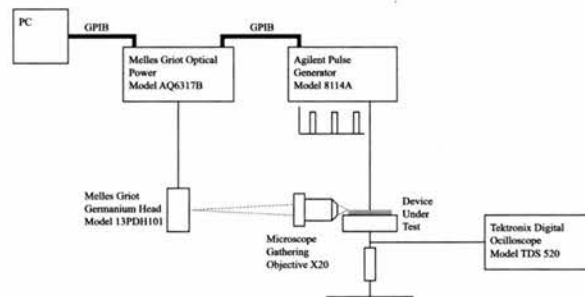


**Figure 6.2:** Schematic of L-I test set-up. The output from the lasing cavity was captures using an optical fiber .

A standard objective lens is used in front of the output laser facet to collect the optical output of the device. Both broad area lasers and lasers designed for single mode operation were tested using this method. An Agilent pulse generator was used to inject current into the cavities tested. Injecting current in this fashion minimised the heating effect associated with the current injected. The wafer structure dictated that the current is injected into the cavity from the p-side of the junction.

### 6.2.2 Tuning Spectra Measurements

The response of the lasers tested with respect to wavelength was measured using an ANDO AQ6317B optical spectrum analyser. The optical spectrum from the output facet of the device under test (either a single mode or a coupled cavity device) was captured using a single mode optical fiber. The test set-up used for these experiments is presented in Figure 6.3. When testing laser with the coupled cavity configuration, measurements were taken from the output facet of the lasing section. The lasing section was driven with a pulsed waveform, while a ramp function was used to drive the tuning cavity.

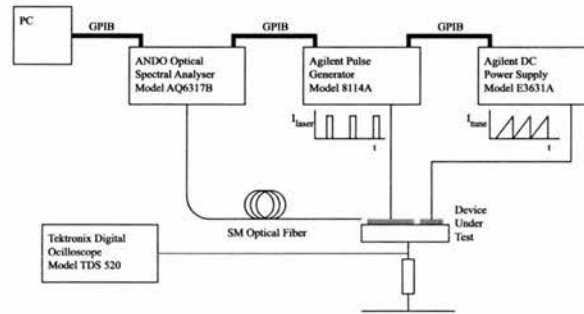


**Figure 6.3:** Schematic of a device under test. The tuning cavity is pumped CW while the laser cavity is pumped pulsed with various duty cycles.

By driving the tuning section of the laser with a ramp function and taking spectral traces of the lasing section's output at convenient points along the range of the ramp function allows the effect of the current injection in the tuning section to be measured. Comparison of the spectral traces proved the presence of tuning.

Operation of the devices for prolonged periods and with various duty cycles provided evidence that initial concerns for the effect of thermally heating in the samples were misplaced. Typical examples of obtained L/I and current tuning curves are presented in the following section.

## 6.3 Results

In this section the measured results obtained for the L-I curves of a typical laser cavity and wavelength tuning curves for two distinctly different coupled cavity laser configurations are presented. The wavelength tuning characteristics for a two section laser with a significant cavity length ratio is presented first. These results, from a laser with lasing and tuning cavity lengths of  $200\ \mu\text{m}$  and  $20\ \mu\text{m}$  respectively, confirm the previously established conjecture that the stability of a coupled cavity laser is enhanced for the long-short cavity configuration [131]. The second design investigated stems from the work presented in Section 3.4.2, where a cavity length difference of approximately  $15\ \mu\text{m}$  was determined to be optimum for length difference for tuning in the material configuration used. This cavity length difference when applied to device with tuning cavity length of  $280\ \mu\text{m}$  defines the configuration of the second device investigated.

### 6.3.1 L-I Curves

Using the experimental set-up outlined in Section 6.2.1, optical power measurements were conducted on a sample of coupled cavity lasers. The aim of the experiment was to determine the presence of and possibly quantify the magnitude of any thermal heating of the cavity. It is well known that the power characteristics of semiconductor laser diodes depend strongly on temperature, and that the threshold current of a double heterostructure laser increases significantly with temperature due to the diffusion of electrons and holes from the active layer and the enhancement of non-radiative recombination effects.

Due to large current densities injected over small active regions, during operation the laser diode can experience strong thermal effects. In an effort to ascertain the existence of temperature related problems in the test set-up and determine the degree of cooling required, the lasers were run in pulsed operation with a variable duty cycle from 10 % through to 70 % and the data normalised to CW conditions for comparison.

From the graph of peak optical power as a function of peak current in Figure 6.4, the efficiency of the lasers tested is around 30 %. Testing was conducted up to a current values of 20 mA, approximately three times the

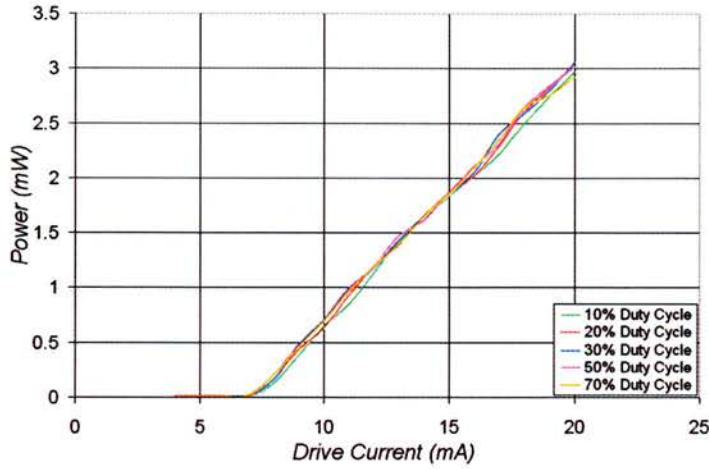


**Figure 6.4:** Graph of the peak output optical power as a function of peak current for a variety of duty cycles. The Threshold current obviously occurs around 7.3 mA for this particular laser.

threshold current. From the L-I results obtained, we can conclude that the effect of heating from device operation/testing can be considered as negligible for lower drive current values.

### 6.3.2 Tuning Curves - Long-Short Results

The tuning curves for a typical long-short coupled cavity laser possessing a high cavity length ratio is presented in Figure 6.5.

The tuning curve, taken over a tuning current range of 0 - 20 mA in steps of 1 mA, demonstrates that the modal spacing of the tuning cavity is significant enough such that the frequency of coincidence between the modes of the lasing cavity and those of the tuning cavity is limited. Intuitively we expect the range over which tuning takes place to be limited by the reduced number of coincidental modes existing between the cavities. This is demonstrated clearly from experimental results shown in Figure 6.5, where between vernier jumps 2, 3 and 4 lasing modes are experienced with increasing tuning current. The precise number of modes increases with tuning current due to an associated shift and expansion the gain spectrum. Exact details of the size and width of

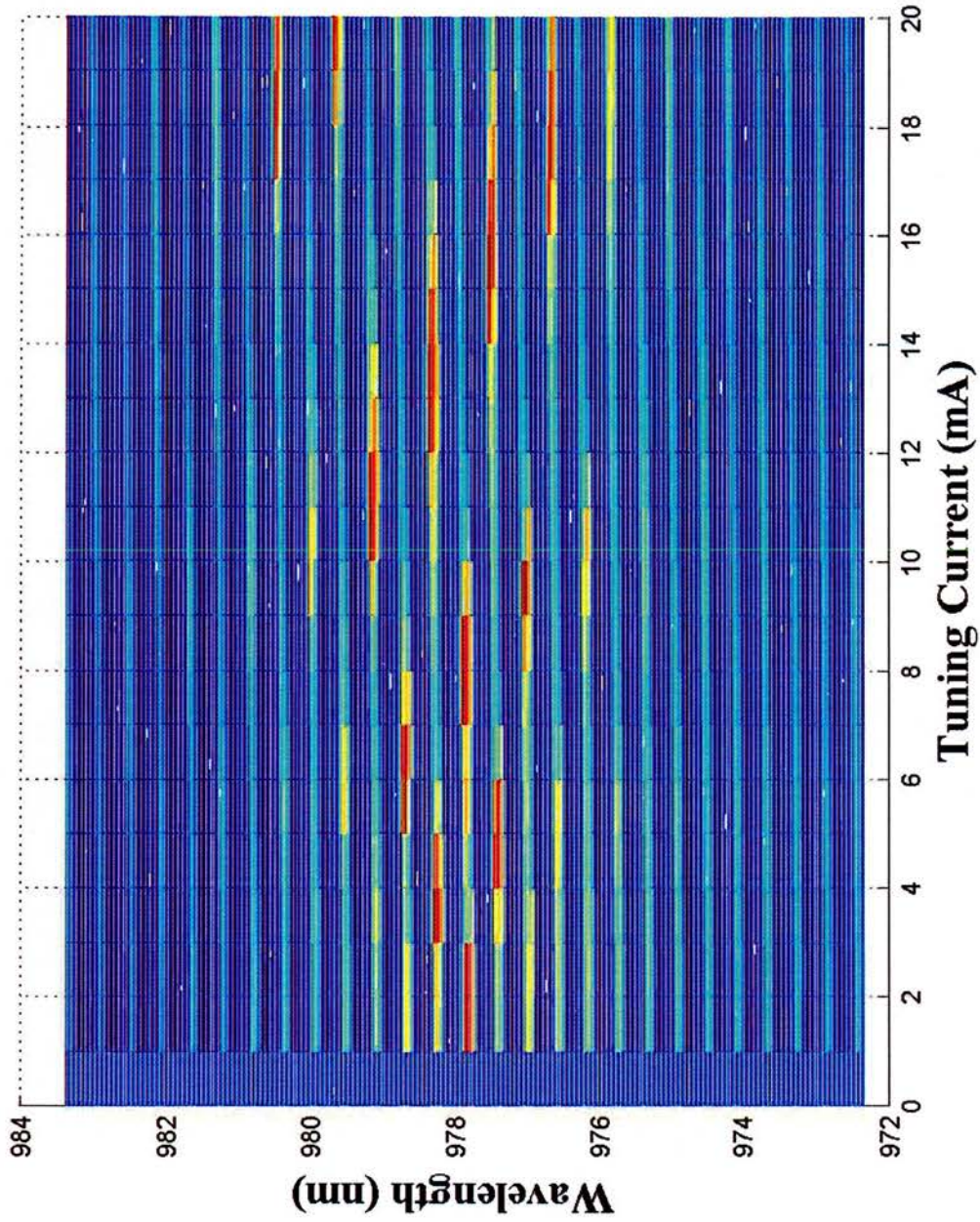


Figure 6.5: Typical tuning curves obtained from a long - short cavity device plotted on a Linear scale.

the gain depends directly upon the range of the tuning current under consideration. The number of discontinuous steps in a vernier range is significantly less than that demonstrated for the long-long cavity configuration.

These results are for initial experiments conducted on lasers where the cavity length difference was significant. The cavity lengths of this 'long-short' were designed to be 200 and 20  $\mu\text{m}$  for the lasing and tuning cavities respectively. The resonant modes of the coupled cavity device are seen to remain almost constant over a current range of between 2 to 3 mA. At this point a tuning step take place. The modal spacing of the coupled cavity device was determined to be 0.395 nm on average, while the discontinuous tuning step of 0.820 nm. The side mode suppression ratio for these cavity configurations was found to vary between 9 and 23 dB. The manner in which the tuning curve in Figure 6.5 changes suggests that the 'tuning' mechanism of the 'long-short' coupled cavity device is predominantly governed by the physical dimensions of the device and the gain spectrum rather than tuning by carrier injection. The variation in side mode suppression is attributed to the cavity length ratio, in that the long-short cavity configuration displays modal stability over larger variations in tuning current. This effect, *i.e.* the sparsity of coincidental modes, in conjunction with gain spectrum of the material used in the construction of the device conspire to give the spectrum demonstrated.

### 6.3.3 Tuning Curves - Long-Long Results

In contrast to 'long-short' cavity configurations, lasers based on the 'long-long' cavity demonstrate an increase in the degree of tuning motion. The cavity length ratio for this device was designed to be 280:300<sup>1</sup>  $\mu\text{m}$ . Figure 6.6 is a set of individual spectra demonstrating a smooth tuning range for an input tuning current varying over the range of 3 to 11 mA. The center wavelengths for the main mode of the output are listed in the column adjacent to the graph. The associated tuning current for the peak wavelength is also listed.

Over the full 30 mA range examined only a single vernier transition (at a

---

<sup>1</sup>As in the previous example, the physical dimension of the laser cavity will include an unavoidable error due to the accuracy of the cleaving process. Estimations of error are around  $\pm 5$  to  $10 \mu\text{m}$ .

tuning current of approximately 15 mA) was found to take place. The complete tuning curve is presented in Figure 6.8.

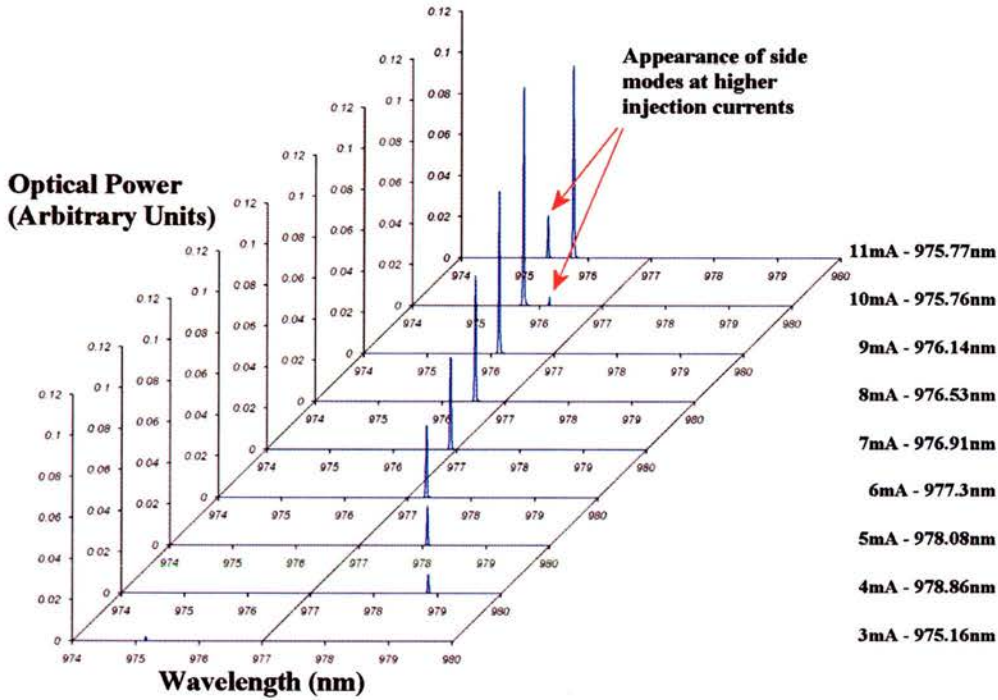


**Figure 6.6:** Typical tuning curves obtained from a long - long cavity device plotted on a Linear scale. Tuning currents and peak central wavelength are specified in the adjacent list.

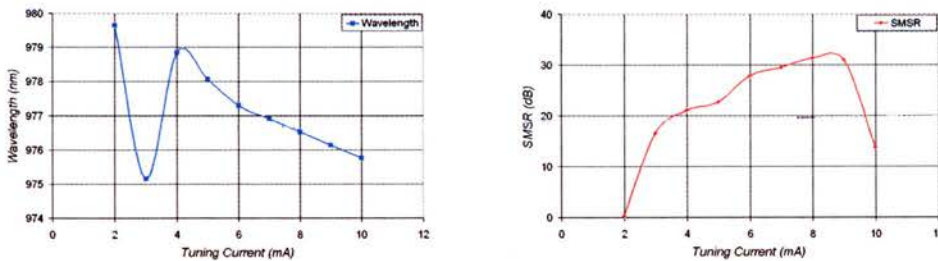
Intuitively, laser configurations where the difference between the lasing and tuning cavity lengths is small demonstrate a smoother, more dynamic tuning curve. From the spectra in Figure 6.6 it is evident that the degree of modal coincidence for the 280:300 laser is significantly greater than that for the 20:200 device. From the results the tuning step was determined to be 0.38 nm, while a modal spacing of 0.404 nm was calculated. It is important to distinguish between the range of tuning observed from the cavities and the degree of tunability within this range. The range of tuning is primarily determined by the material gain curve, while the ability to address the wavelengths within this gain envelope is a complex function of the device design, and operating

conditions of the laser.

Two further points are evident from the spectra in Figure 6.8. The first is the observable increase in the optical power from the device as tuning takes place. As the current injected into the tuning section of the device is increased the optical loss experiences by the resonant mode is reduced, resulting in the observed increase in the overall output power. The second observable feature indicated in Figure 6.6 is the appearance of side modes at higher operating currents. The suppression of side modes at higher operating currents is attributed to the gain of the lasing cavity being able to subjugate the modal selection mechanism of the device.

### 6.3.4 Overview of Results

The differences in the tuning characteristics for the two cavity length ratios demonstrate that for the short-long case there is a step-wise tuning characteristic, where the lasing mode of the device is almost constant over a 2 to 3 mA range of tuning current. The mode jumps to longer wavelengths are significantly larger in size than those displayed for the long-long cavity arrangement. The long-long cavity arrangement offers a much smoother tuning curve at the expense of an increased number of tuning ‘steps’ between vernier jumps.



(a) Operational wavelength as a function of tuning current for an asymmetric coupled cavity laser. (b) Side mode suppression ratio for the same asymmetric coupled cavity laser.

**Figure 6.7:** The tuning range as a function of tuning current (left) and the side-mode suppression ratio over the same range.

Figure 6.7 contains plots of the tuning range 6.7(a) and the side mode

suppression ratio 6.7(b) as a function of the tuning current for a 280:300  $\mu\text{m}$  coupled cavity laser. If we set the requirements for a minimum SMSR of 20 dB, a tuning range of 942 GHz was measured with a corresponding tuning current range of 6.13 mA. As one would expect, this tuning range decreases as the minimum acceptable SMSR is increased. At 30 dB, the tuning range drops to 287 GHz for a tuning current range of 2 mA. From the measurements taken, a modal spacing of approximately 0.408 nm was obtained for the range of tuning currents tested. This modal spacing is in good agreement with theoretical predictions presented in Section 3.4.5.

With reference to the wavelength tuning characteristic of Figure 6.7(a) a sudden shift in the operational wavelength of the coupled cavity laser can be observed. Shifts of this type are attributed to the undesired alignment of the cavity modes, which are usually the result of errors in the cavity lengths. The most significant source of variations in cavity lengths is due to tolerances in device cleaving.

The results presented in the annotated Figure 6.8 demonstrate the three main regions that are evident in the tuning characteristics during laser operation. The key features of the regions indicated in Figure 6.8 are;

**Region A** Over the current tuning range between 5 and 12 mA, the general trend of the tuning is towards (blue) shorter wavelength. The laser operates monochromatically and the tuning mechanism over this range is dominated by electronic tuning.

**Region B** At a value of 13 mA, the tuning range of the laser reaches the lower limit of the material gain curve. The modal discrimination due to the gain curve falls as the operational wavelength experiences gain roll-off. As the intensity of the mode drops, the condition for the existence of a new mode at the other end of the gain curve becomes favourable. This new mode is due to a second coincidence of the two cavity resonances combs. At 15 mA both the new and old modes exist in the cavity, their operational wavelengths lie at opposite ends of the gain spectrum at this point.

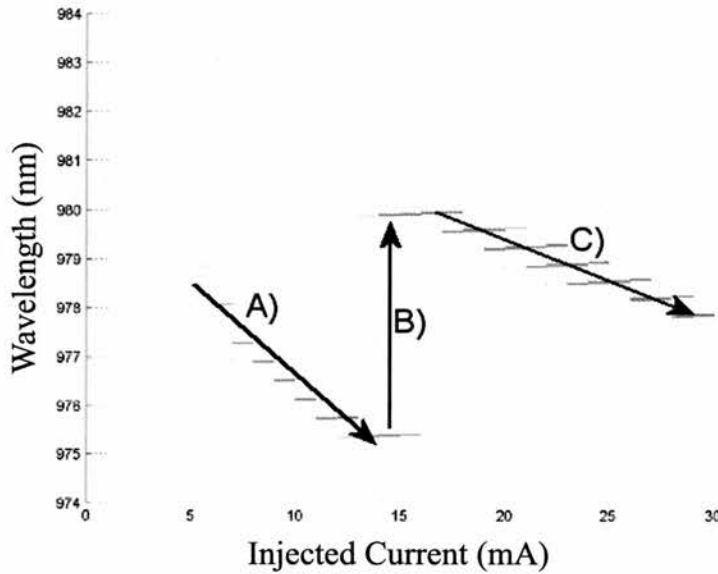


**Figure 6.8:** The tuning range as a function of tuning current presented in two dimensions. The device from which these results are taken comprises a  $300\ \mu\text{m}$  lasing cavity, a  $280\ \mu\text{m}$  tuning cavity and a cavity separation distance of  $960\ \text{nm}$ . From the graph three distinct features are evident.

**Region C** Over a restricted range from  $16$  to  $30\ \text{mA}$ , three significant effects become apparent. The first and most obvious is the loss of mono-tonic tuning. While the overall trend in this region of the tuning curves is to drive to shorter wavelengths there is an under-lying trend acting on each of the modes to drive to longer wavelengths. This is indicated in Figure 6.9 The second effect is that the laser ceases to operate as a true monochromatic source over this region. The appearance of a second mode towards the end of these tuning steps indicates that the mode discrimination mechanism is failing. The third change in the tuning curve concerns the magnitude of the tuning current required to shift the wavelength, the duration over which a mode of operation remains constant increases.

While it is possible to use moderate increases in sample temperature to explain the observed (red) shift to longer wavelengths, described in point 2

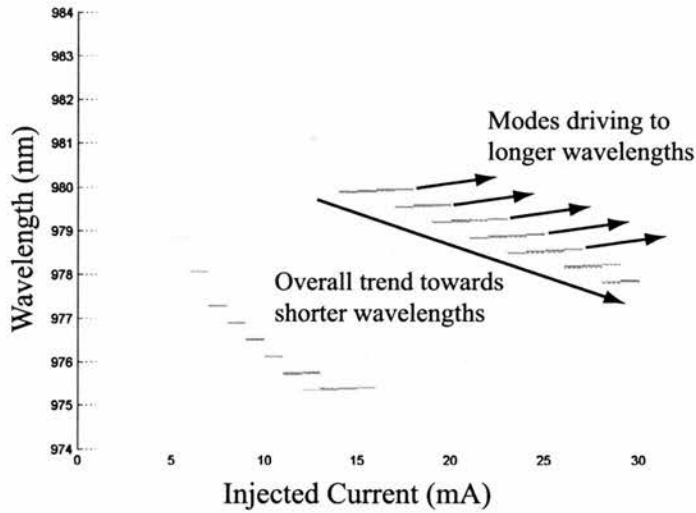


**Figure 6.9:** The tuning range as a function of tuning current presented in two dimensions. Emphasis is placed on the underlying trend acting on the modes of operation which are driving to longer wavelengths.

of Region C above, the effect of the carrier density on the tuning curves also contribute to these shifts.

## 6.4 Basis for Operation

The change in gain and refractive index with carrier density in conjunction with the carrier density's relationship to the injected currents and optical power provide the mechanism for operation of the coupled cavity arrangement. Linking the refractive index and gain change is crucial to understanding coupled cavity operation.

### 6.4.1 Single Cavity Laser

For a single cavity laser operating under normal conditions, the equation for the gain per unit length (Equation 2.9) must be satisfied to compensate for the optical losses incurred due to absorption, etc. and also the losses due to light emission. The concept of gain cancelling out the losses continues to apply

above the threshold condition although due to saturation effects, variation of the gain per unit length occurs. At these operating points, the condition of gain compensating for losses at all points along the laser length no longer applies, although the condition of the round trip gain being equal to one does. As threshold is approached a proportion of the spectral width of the spontaneous emission, which correspond to the Fabry-Perot resonances of the cavity are amplified.

While the circulating gain for these modes is very close to unity, further current injection causes preferential growth of these modes. The validity of the gain condition continues to remain true above threshold until longitudinal saturation effects start to occur. Stimulated emission pins the value of the carrier density required for gain  $\approx$  loss for the lasing mode. The gain per unit length is clamped to its threshold value for low to moderate (10 - 50 %) gain values over the threshold value. This 'locking' of the carrier density effectively sets the operating point of the laser as a whole, and as such the optical cavity length, refractive index and resonances attain a steady state condition.

During operation, fluctuations in the device temperature commonly cause subtle variations of the operating point, and slight drifts in the wavelength of lasing mode are experienced. Deliberate temperature modulation is the most common method available for the tuning of the single cavity laser. Manipulation of the optical cavity length and thereby the cavity resonances using thermal means is the basis of DFB laser tuning.

### 6.4.2 Coupled Cavity Laser

In contrast to the case of a single cavity laser, the gain, carrier concentration and refractive index of the coupled cavity arrangement are not pinned once threshold is achieved. Instead the relationship between the gain and carrier densities of both cavities is described by a complex interaction. The variation in the currents supplied to either cavity can cause significant changes in the operating conditions of the adjoining cavity. Figure 6.10 outlines the components of the basic coupled cavity arrangement.

In the coupled cavity laser, two carrier densities supplied by two different

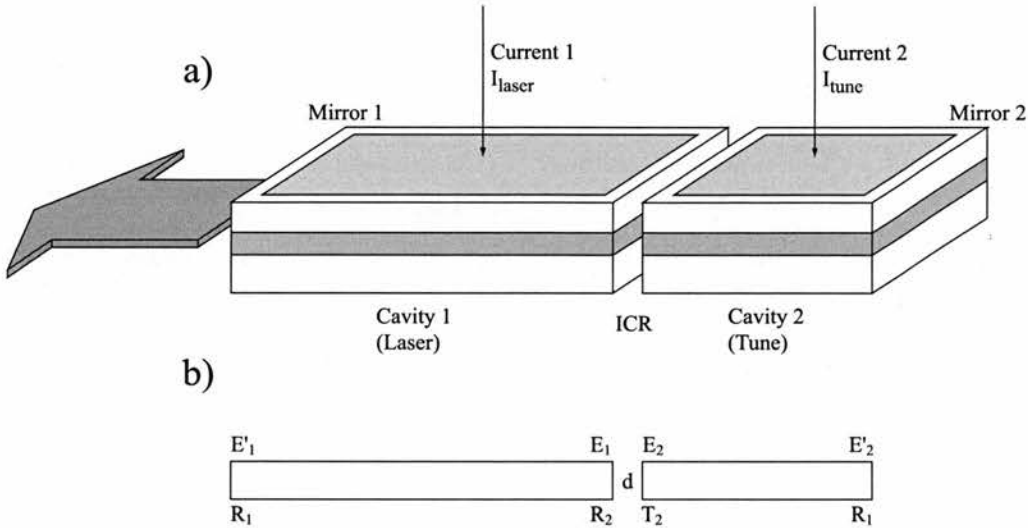


**Figure 6.10:** Figure a) Schematic of a coupled cavity arrangement. Both cavities of the composite device is electrically isolated. Currents are injected into the cavities independently. Figure b) Field transmission and reflection coefficients of the gap separating lasing and tuning sections.

injection currents operate in the device. Stimulated emission only provides a relationship between the two carrier densities, but does not pin them.

### The Qualitative Model

From Figure 6.10, if we assume that the 1<sup>st</sup> cavity represents a CW lasing cavity, and that the 2<sup>nd</sup> cavity takes the role of the tuning element, the interaction of the fields coupled between the two cavities act to modify the operating conditions of the overall device. In the case where no current is injected into the tuning cavity, normal operation of the laser cavity occurs, with the internal facet reflectivity of the 1<sup>st</sup> cavity being replaced by an effective reflectivity. This effective reflectivity, representing the culmination of the ICR, the spectral response of the second cavity and the reflectivity of the output facet (Mirror 2), is a function of both wavelength and carrier density  $R(\lambda, N_{\text{tune}})$ . During the operation of the coupled cavity device, current injected into the laser cavity ( $I_{\text{laser}}$ ) must overcome the various losses associated with the mirrors

$M_{1,2}$ , the ICR and the absorption of the tuning cavity for sustained oscillation.

The injection of carriers into the tuning cavity modifies the refractive index, effectively dropping its value (by an amount proportional to the current density  $I_{\text{tune}}$ ) relative to the laser cavity. This slight variation in the localised tuning carrier density and therefore refractive index causes a detuning of the system. With this drop in refractive index there is an associated shift upwards in the coincidental/lasing wavelength of the composite device. The slight shift of the coincidental resonance peak of the second cavity causes an effective increase in the loss experienced by the lasing mode. In order to maintain lasing conditions in this detuned state, the laser cavity consumes a larger proportion of injected carriers, effectively increasing the density of carriers resulting in an decrease in the refractive index of the lasing section. Increasing the carrier density in the tuning section, increases the state of population inversion, and as such effectively reduces the absorption of photons passing through the tuning cavity. The system is dynamic, but and quickly attains a new state of ‘equilibrium’. Fluctuations in the operating conditions of the laser can momentarily create bistable behaviour, which have possible uses in the fields of digital optical read/write or elements for an optical logic system [94, 132].

From the point of view of the gain, an increase in the current flowing into the tuning cavity ( $I_{\text{tune}}$ ) leads to an increase in the optical power generated in the tuning cavity, which in turn increases the stimulated emission in the lasing cavity. For a fixed current flowing into the lasing cavity ( $I_{\text{laser}}$ ), the gain in the laser cavity ( $g_{\text{laser}}$ ) will decrease. To compensate for this drop in the gain, the tuning cavity gain ( $g_{\text{tune}}$ ) must increase by a definite amount to maintain lasing. Therefore, neither ( $g_{\text{laser}}$ ) or ( $g_{\text{tune}}$ ) are pinned, but there is a relation between them. This also applied to the carrier densities  $J_{\text{laser}}$ ,  $J_{\text{tune}}$  and to the refractive indices  $n_{\text{laser}}$  and  $n_{\text{tune}}$  in the two cavities.

### The Quantitative Model

The fields of the two cavities of a coupled cavity laser are indicated in Figure 6.10. The fields at the gap ( $E'_1$  and  $E'_2$ ) are related to the complex transmission and reflection coefficients  $T_2$  and  $R_2$  that completely characterise the gap. The

field  $E'_{1/2}$  at the gap results from the reflection of  $E_{1/2}$  and the transmission of  $E_{2/1}$ .

$$\begin{aligned} E'_1 &= R_2 E_1 + T_2 E_2 \\ E'_2 &= R_2 E_2 + T_2 E_1 \end{aligned} \quad (6.1)$$

The electric field round trip through cavity 1/2 results in a relation between  $E_{1/2}$  and  $E'_{1/2}$

$$\begin{aligned} E_1 &= R_1 \exp[(g_1 - \alpha)L_1 + 2ik_1 L_1] E'_1 \\ E_2 &= R_1 \exp[(g_2 - \alpha)L_2 + 2ik_2 L_2] E'_2 \end{aligned} \quad (6.2)$$

Eliminating  $E'_{1/2}$  from the above equations, yields the homogeneous equations

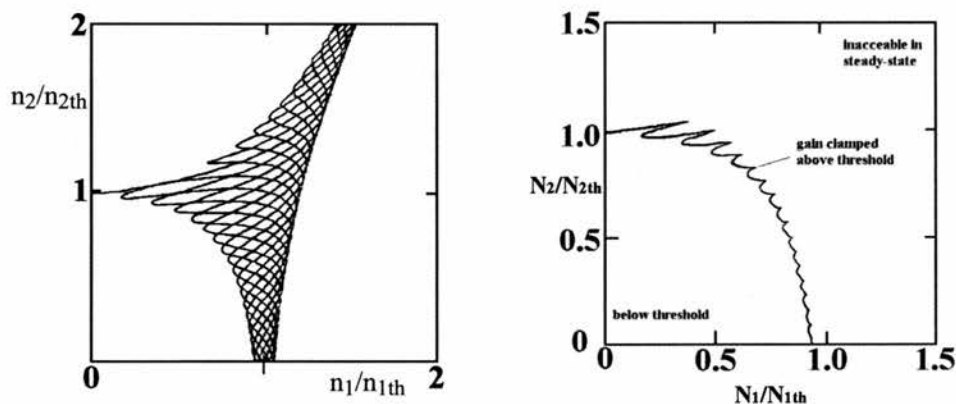
$$\begin{aligned} \left[ \frac{\exp[(g_1 - \alpha)L_1 + 2ik_1 L_1]}{R_1 R_2} - 1 \right] E_1 &= \frac{T_2}{R_2} E_2 \\ \left[ \frac{\exp[(g_2 - \alpha)L_2 + 2ik_2 L_2]}{R_1 R_2} - 1 \right] E_2 &= \frac{T_2}{R_2} E_1 \end{aligned} \quad (6.3)$$

The behaviour of two-element coupled cavity can be described by the equations of motion [133]. These equations describe the dynamic behaviour of the laser, and when solved for dc solutions, provide the conditions for stable and bistable regimes of operation. The modes of operation can be determined from the secular equation describing round trip self-reproduction condition. This yields the secular equation

$$\begin{aligned} \left[ \frac{\exp[-(g_1(N_1)L_1 + 2j\omega n_1(N_1)k_1 L_1/c)]}{R_1 R_2} - 1 \right] \times \\ \left[ \frac{\exp[-g_2(N_2)L_2 + 2j\omega n_2(N_2)k_2 L_2/c]}{R_1 R_2} - 1 \right] = \frac{T_2^2}{R_2^2} \end{aligned} \quad (6.4)$$

where  $g_i(N_i)$  is the linear gain constant for the  $i$ 'th cavity,  $n_i(N_i)$  is the index of refraction,  $R_1$  is the reflectivity of outside mirrors, and  $T_2^2/R_2^2$  is a coupling factor which characterises the gap (taking into account the length and reflectivity of the mirrors bounding the gap) [94].

In solving the equation for the carrier densities, one finds that for a fixed pair of cavity carrier densities  $(N_1, N_2)$  there are an infinite number of complex  $\omega$  solutions; each corresponding to a different longitudinal mode of the structure. The real part of the  $\omega$  represents the phase of the optical field and is not of interest, therefore we are purely interested in the imaginary part of the solutions. Considering the carrier density plane with this new criterion, one finds that the plane can be divided into three sections, namely that for  $\text{Im}(\omega) < 0$ ,  $\text{Im}(\omega) > 0$  and the line for which  $\text{Im}(\omega) = 0$ . The line defined by  $\text{Im}(\omega) = 0$  corresponds to a quasi-steady-state mode, which neither grows nor decays over time. For solutions where  $\text{Im}(\omega) < 0$  the solutions are found to grow without limit, which cannot be a realistic solution. Similarly for solutions where  $\text{Im}(\omega) > 0$  the mode cannot be sustained and decays to zero. Figure 6.11(a) demonstrates the superposition of ten modes for a coupled cavity laser with  $L_1 = 200 \mu\text{m}$  and  $L_2 = 20 \mu\text{m}$  and a normalised gap of  $1.5 \lambda$ .



(a) Plot of ten modes in the carrier density plane. (b) Different regions of the carrier density plane. Above threshold the carrier density is clamped onto the threshold carrier density line. Each cusp on the curve indicates a mode hop.

**Figure 6.11:** Plot of ten modes in the carrier density plane. The solutions are for the case where  $\text{Im}(\omega) = 0$ . Figure courtesy of [132].

The trace presented in Figure 6.11(b) defines the lowest possible combinations of  $N_1$  and  $N_2$  on the carrier density plane for which the condition of

$\text{Im}(\omega) = 0$  is maintained. The resulting curve define the operating point of the coupled cavity laser. This curve varies in size and shape depending upon the coupled cavity configuration. In the area below the line, where  $\text{Im}(\omega) > 0$ , no lasing state exists, while the area above the curve, where  $\text{Im}(\omega) < 0$ , is only accessible during transient operation.

Pragmatically the curve of Figure 6.11(b) represents the lowest possible modes (for an  $N_1, N_2$  combination) which the coupled lasers will operate. The overall curve is constructed from portions of individual modes, while the cusps of the curve correspond to hops between these modes. Above lasing the carrier density is clamped onto this threshold line (although is free to shift along the curve). Intuitively if the laser is driven to operate at the intersection of two curves, it could conceivably have two lasing modes. It is these modes, and the action of mode hopping between them which define discontinuous tuning nature of the coupled cavity lasers.

Careful observation of the curve in Figure 6.11(b) demonstrates concurrence between the qualitative and quantitative models described and presented above. If one considers the case for the second cavity running in a steady state condition, while the first cavity remains unpumped, one can regard the operating point to be on the vertical axis at  $N_1/N_{1\text{th}} = 1$ . As current injection into the first cavity commences, the carrier density of the second cavity is seen to increase slightly before the characteristic nature of the modes and cusps essentially the system behaves as a single laser with one mirror producing variable feedback. The afore mentioned detuning of the system and its effect on the carrier density of the lasing cavity required an initial increase in the ratio  $N_1/N_{1\text{th}}$ . Although the magnitude of this effect diminishes, the trend can be seen time and time again as the operating point of the laser moves along the line of permitted modes, the approach to the cusp is characterised by a subtle increase in the carrier density of the lasing cavity.

## 6.5 Discussion

Application of the quantitative model discussed in Section (6.4.2), using parameters for the device designs fabricated in the project is used to examine

the validity of the experimental results obtained during characterisation.

### 6.5.1 Device Modelling

In determining the curves which describe the modes in our devices, expressions for the gain and the refractive index variation as a function of the injected carrier density are required. For the gain variation with carrier density a logarithmic expression was derived from the data provided by the theoretical plot of the gain (Section 2.3.3). A linear approximation to the refractive index variation was adopted from [134, 103]. In short, the expressions used to approximate the gain and refractive index variations are:

$$g(N_x) = \Gamma g n_0 \log \left[ \frac{n}{n_0} \right] \quad (6.5)$$

$$n(N_x) = 3.5 - 0.001 \times \frac{n - n_0}{0.3 \times 10^6} \quad (6.6)$$

where 'g' is the gain parameter derived from the gradient of the peak gain as a function of carrier density,  $n_0$  is the transparency carrier density and x is the cavity reference.

The solutions to a multi-dimensional problem, such as the one presented here, were determined using the simplex method of Nelder and Mead [135]. This method finds local minima for generic multi-dimensional functions. The process of plotting the modal curves begins by seeding the carrier-density plane with randomly generating initial points. The Nelder-Mead simplex algorithm is not particularly efficient in terms of the number of function evaluations required to achieve a given level of accuracy, but was preferred over a derivative method because of the nature of the function. Experiments demonstrated that differential methods generally worked towards solutions for the higher values of the carrier density plane. The evaluation range of the model The 'tolerance' used for determining the cut-off point for the evaluation was  $1 \times 10^{-12}$  and Figures 6.12 and 6.13 represent the results obtained using this method evaluation.

### Modal Distributions

Figure 6.12 demonstrates the resulting mode graph for the long-short cavity configuration. The main feature of the graph is the magnitude of the individual lobes which define the preferred operating line for the device. In comparison to the long-long cavity configuration, these are approximately 2 to 3 times larger measured from cusp to cusp. The low density of the hairpin curves which make up the sweeping from the simulation is consistent with the observer performance of the long-short configuration.

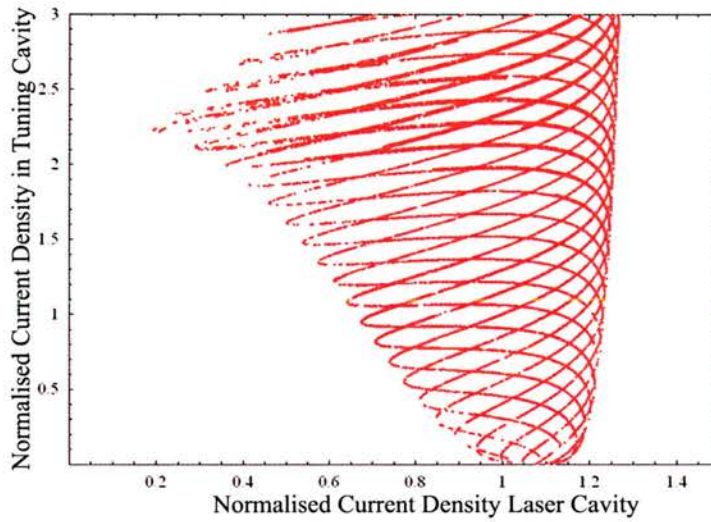


**Figure 6.12:** Modal contours for the condition  $\text{Im}(\omega) = 0$  over a 10 nm range centered around at a wavelength of 980 nm. The results are a theoretical prediction for the long-short cavity configuration.

The number of coincidental modes for the cavities is defined primarily by the modal spacing of the shorter cavity. The wavelength range over which the simulation was conducted was taken from the ranges demonstrated by the experiment, from 975 to 985 nm. Over this wavelength range the preferred operating mode can be seen to remain constant for a larger variation in tuning current. This is reflected in the almost linear nature of the modal contour and concurs with the results obtained experimentally.

Figure 6.13 demonstrates the theoretical prediction for the modal graph a

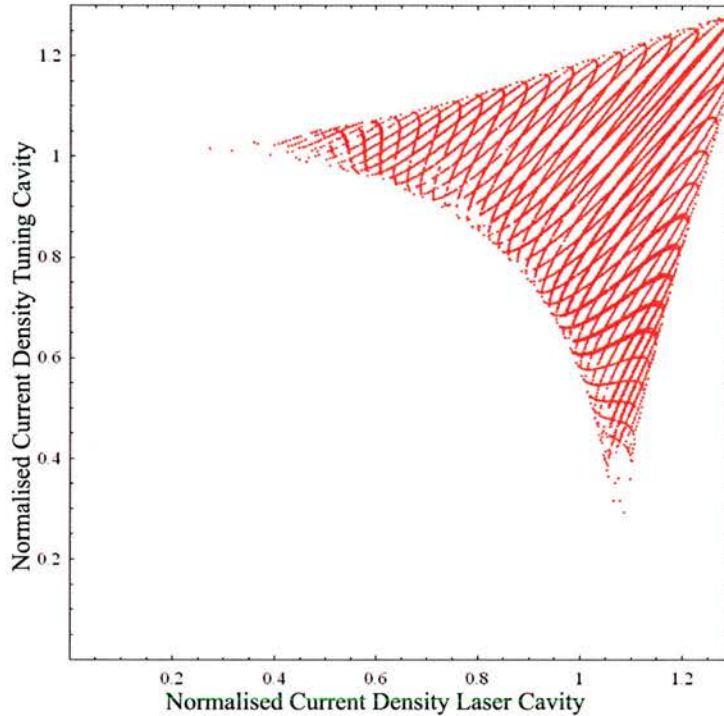


**Figure 6.13:** Modal contours for the condition  $\text{Im}(\omega) = 0$  over a 10 nm range centered around at a wavelength of 980 nm. The results are a theoretical prediction for the long-long cavity configuration.

long-long cavity configuration. In contrast with Figure 6.12 the density of the hairpin curves in the long-long cavity is significantly higher. The curvature of the operating line can be seen to be significantly greater than that for the long-short cavity devices, this is a direct result of the cavity lengths. The current range over which the laser remains in a single mode is therefore less than for the long-short cavity. This is in agreement with the measurements taken from the device, where up to twelve mode hops were detected between the vernier shifts in the operating wavelength range.

### Comparison of Results

Comparison of the theoretical and experimental results for the long-short cavities provide evidence for the accepted operational characteristics for this de-

vice, namely high wavelength stability and a limited range of tuning. The results for the long-long cavity also concur with the predicted results of a highly tunable laser which is sensitive to subtle changes in operating parameters.

Returning to Figure 6.8, if the vernier jump discussed as region B) in Section 6.3.4 was to be ignored, that is to say if the effect of the gain roll-off was to be ignored, the measured tuning curve could conceivably follow a characteristic form similar to that presented in Figure 6.14<sup>2</sup>.

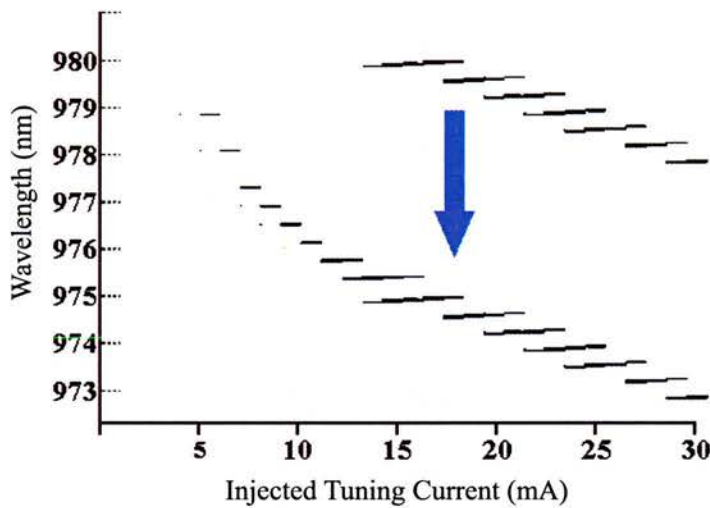


**Figure 6.14:** The experimental results from the long-long cavity configuration modified to effectively remove the vernier jump associated with the gain roll-off.

While the overall operation of the tuning curve is to drive to lower wavelengths, the tuning characteristic of the long-long cavity configuration can be seen to slow when the carrier injection levels become high. In explaining the slow down in tuning one could presume that there is a change in the general operation of the device from a laser interacting with a spectral tuning element to a case where two lasers are interacting independently. The fall/failure of side mode suppression at higher injection currents is conceivably a direct result of this interaction.

<sup>2</sup>The adaptation of Figure 6.8 to neglect the vernier jump was conducted using a graphics package, this curve in no way claims that the tuning follows this trend. It is presented for explanation purposes only.

### Investigation of Tuning Results

Figure 6.15 demonstrates the overlay of the experimental results with the theoretical prediction of the model. While the case of the 300:280  $\mu\text{m}$  (long-long) cavity configuration is presented here, results for the long-short provide a similar result. The obtainable tuning range for the laser was found to be very restricted when considering the available operating conditions predicted by the model.

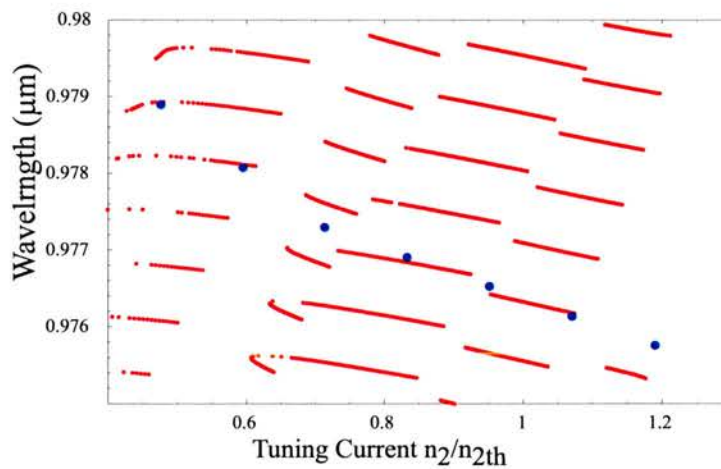


**Figure 6.15:** Overlay of the experimental onto the theoretical predictions for the 300:280 nm cavity configuration.

While the general trend of the tuning experimental curve is confirmed by the predictions from the model. The predictions are based on a one-dimensional analysis which does not attempt to take into account variations in the structure, imperfections or operating performance of the laser. The model developed thus far provides the permissible operating modes for specific current densities which are physically limited to a specific wavelength range. With this in mind, direct comparison of the experimental and theoretical results obtained is problematic. Figure 6.15 demonstrates the best fit for the experimental data taken during our tests. The operating wavelengths of the laser are indicated by the blue dots while the red lines represent truncated elements of the wavelength range over which the simulation was run. In an

effort to demonstrate the trend of the theoretical values a small margin either side of the operating wavelength point is plotted. This graph exemplifies the tuning trend displayed by the device.

### **Model Analysis**

As indicated, the theoretical predictions are based on a one dimensional model which does not describe the system realistically. In order to achieve a more realistic representation, the operation of the laser with regard to the photon density in each cavity, radiative and non-radiative recombination mechanisms and longitudinal mode profiles must be considered. Work currently being conducted by Dr. E. Avrutin of the University of York, provides a more rigorous model of the coupled cavity laser device. The results from this model have could not be yet correlated to the experimental data, and will be subject to future work.

Given the assumptions of gain and refractive index variation as a function of cavity carrier density, overall the measured tuning spectra agree within the limits of the model, given the relative simplicity of the model used.

# Chapter 7

## Conclusions and Further Work

### 7.1 Introduction

In this, the final chapter of the thesis, results obtained and key achievements in the project are summarised. Suggestions for further investigation into areas of the project which proved interesting or challenging are presented, and where possible, avenues to approach the issue are given. Finally a summary of the project goals/results is presented.

### 7.2 Conclusion on Results

This section considers the main achievements of the thesis. The fabrication processes described in this section were developed for the fabrication of wavelength tunable laser diodes containing sub-wavelength features.

#### **Developments in Fabrication Processing**

A chemically assisted ion beam etching (CAIBE) process was developed for the fabrication of deeply etched narrow gratings in the GaAs/AlGaAs laser material structure. Previously, a parallel plate reactive ion etch chamber was used to create grating features. This process, although very stable, was only able to achieve etch depths of around 800 nm to 900 nm before erosion of the PECVD SiO<sub>2</sub> etch mask lead to loss of feature dimensions. Various materials

were investigated as an etch mask substitute, SU-8, FOx-12 and PECVD SiO<sub>2</sub>. Of these FOx-12 proved the most resilient to the more aggressive CAIBE process. Using the combination of FOx-12 and CAIBE, repeatable etching of deep, narrow gratings measuring up to 2.2  $\mu\text{m}$  was demonstrated, an enhancement of 2.5 times that previously achieved.

### **Electron Beam Writing**

Electron beam lithography was used throughout the project for the definition of ultra-small 1-D gratings and 2-D periodic structures. The coincidental exposure of adjacent features in such densely packed sub-wavelength patterning leads to over exposure of the pattern. Correction methods were investigated and developed to compensate for this 'proximity exposure'. The procedure used to determine the correction parameters for the dose scaling method of proximity correct is presented.

### **Monolithic Integration of Reflector**

The monolithic integration of a Bragg reflector with a discretely tunable laser has been realised. The incorporation of a Bragg reflector makes it possible to achieve optical feedback from high index contrast, deep etched surface gratings. Electron beam lithography was used for the direct writing of sub-micron third order reflection gratings and permit the replacement of single outer cavity mirror and assisted in the monolithic integration of the devices.

Spectral response from solitary gratings manufactured using design and fabrication techniques employed in the construction of the actual compound device were taken. These results confirmed the effectiveness of the grating and that measured transmission spectra agreed with theoretically determined spectra. The fabrication techniques used do not therefore adversely affect the performance of the grating.

### **Coupled Cavity Laser Operation**

Two section coupled cavity lasers were designed, fabricated and characterised. Lasers with different cavity length ratios were investigated, and the influence of

this ratio on the operating characteristics of the device considered. Of the results presented, devices following the long-long cavity configuration proved to be the more interesting in terms of tuning range and side mode suppression ratio. Devices demonstrated single wavelength operation over wavelength ranges of 4 nm, and side mode suppression ratios up to 33 dB were observed. The 4 nm tuning range was achieved over a tuning current of 6 mA, where the modal spacing over this discontinuous tuning range was measured at approximately 0.408 nm.

## 7.3 Suggestions for Further Work

In this section, topics for which ‘further investigation’ could lead to the enhancement in the functionality of the lasers are suggested. The subsection entitled ‘towards integration’ explores the usefulness of the coupled cavity device and suggests issues which require attention if the coupled cavity laser is to be integrated. Possible applications of coupled cavity tunable laser conclude this section.

### 7.3.1 Further Investigation

#### Tuning Model Development

As a suggestion for further work on the topic of coupled cavity lasers, proper development of a model which would be capable of predicting the behaviour of the coupled cavity device could be considered as a worth while task. In this work a simplistic model was used, and assumptions made with regards to the laser geometries and operating conditions. A more realistic model could be constructed to provide an increased accuracy in the operation of the laser.

#### Side Mode Suppression Ratio

While the tunable lasers demonstrated tuning ranges comparable to other devices of similar configuration, values for the side mode suppression ratio were found to be acceptably high, although not constant over the complete tuning

range. One suggestion for future investigation would be to attempt to extending or optimising the SMSR over a larger portion of the tuning range. Possible routes to achieve this are to;

- Investigate the use of different cavity configurations, scrutinising the inter-cavity reflector and it's effect on the mode coupling between the individual cavities.
- Improve on the processes used in the fabrication of the laser structures. With current technologies the definition of features is limited to  $\pm 5$  nm, while the etching techniques can, conservatively, add a further 10 to 20 nm to the device features. Final cleaving the devices proved to be the most significant source of errors, with cleaving tolerances of around 3 to 5  $\mu\text{m}$  being the best achievable.
- Investigate the use of a different material structure, perhaps replacing the quantum wells used with a quantum dot active region, the rationale being that the emission wavelengths of quantum dots can extend up to nearly 1.3  $\mu\text{m}$ .

Although only a suggestion, one of the possible drawback with using a quantum dot approach lies in the the modified density of states of the quantum dot may dramatically reduce non-radiative recombination. Bringing the tuning section to threshold with less current could conceivably reduce the available tuning current range.

### **Enhancement of the Tuning Range**

Of all the parameters which define a high quality tunable laser, the tuning range is probably the most significant. The material base used in this project was a GaAs/AlGaAs waveguide containing two InGaAs quantum wells. The results presented demonstrated a 'vernier' jump as a result of the gain roll-off. Increasing this tuning range could conceivably be achieved by increasing the width of the material gain curve, by incorporating additional quantum wells of different widths. As a direct consequence of this increase in quantum well number, careful consideration must be give to the cavity structures to ensure that only one pair of resonances coincide at any tuning current.

The major drawback with increasing the number of quantum wells lies with the onset of lasing. While it is true that the larger number of wells will require an increase in the injected current to attain threshold, the gradient of the gain curve above threshold is significantly enhanced. It is conceivable that this may restrict the effect the tuning cavity has over the lasing cavity.

The discontinuous nature of the tuning curve is one aspect that can not be compensated for. It is the nature of simple two cavity devices to display this mode hopping. The incorporation of a third 'phase' control cavity/segment is the first step to reducing the effect, but this lies outwith the remit of the project.

### **Device Operation - Thermal Effects**

During testing the effects of temperature on the device operation has been presumed to be negligible. This assumption was deemed acceptable due to the magnitude of the currents used. At higher currents the evidence of the "red-shift" normally associated with the increase in temperature was observed. The incorporation of a Peltier cooler and associated monitoring/controlling circuitry on the sample mount would help determine the existence and severity of this effect.

## **7.3.2 Towards Integration**

### **Integration of a Semiconductor Optical Amplifier**

The optical output from the devices test is by modern standards relatively small. The integration of a SOA is one possible solution to increasing the output power from the laser. Integration of a DBR-laser with a booster SOA has been demonstrated elsewhere [136]. The first suggestion for future research could be to monolithically integrate the coupled cavity laser with a SOA.

### **Passive Waveguide using Quantum Well Intermixing**

Coupled cavity laser integration with both active and passive components will require the steering of the laser output to and from components. A further

suggestion for future work would be the integration of the laser with a passive waveguide formed using quantum well intermixing. The ability to control the quantum well bandgap across a III-V semiconductor laser wafer has been demonstrated using impurity-free vacancy diffusion [137].

### 7.3.3 Possible Applications

The possible roles for a stable tunable wavelength sources are almost without bound. The proliferation of WDM communication systems provides the main thrust for development in this branch of laser.

#### Photonic IC

The integration of photonic components to form high performance photonic integrated circuits (PICs) has been the ubiquitous driving force behind much research. The vision of highly reliable, low power, compact optical equivalents to currently available electronic ICs is very desirable, but progress hampered by the lack of a sound integration platform. Agility Communications, Inc., the champions of an InP-based platform, have demonstrated an integrated PIC transmitter incorporating a widely tunable laser, a back-side monitoring detector, a semiconductor optical amplifier (SOA), and an electroabsorption modulator (EAM). The entire transmitter was fabricated using a single re-growth stage to form gratings and define active and passive regions. Additionally the device is fabricated using the same layer structure and fabrication processes as single cavity lasers.

While it was not the intention for the devices created by this project to compete for wide scale deployment in WDM networks, it may be possible to implement small scale optical networks over the range currently covered by conventional electronics. The use of this type of laser in small 'hobby' optical networks, say for the provision of a communication system for small clusters of computers configured for parallel computing, may be one opportunity. The encapsulation for component integration of the laser with active and passive functions would be one the prerequisite for this type of application.

### **Distributed Computing**

One novel application for the lasers fabricated in this project is in the development of speckled computing. In a project currently being undertaken by fellow researchers, Chris Reardon and Dr. Christina Carlsson, Programmable System on Chip (PSoC) self contained micro-computers are being developed. The principle behind the speckled computing project lies with the PSoC, which may be programmed to gather and communicate information about the unit's surrounding environment. Deployment of these units in large quantities allows the creation of large surface area networks capable of monitoring and reporting the conditions to some form of centralised information database. In order to facilitate communication functionality, these stand-alone units employ wireless radio to communicate with one and other. One of the long term intentions of the 'SpeckNet' project is the conversion of communication from radio based to using optics.

The incorporation of a cheap, almost to the point of being disposable, coupled cavity laser capable of communicating over say five different wavelengths, would increase the functionality of the SpeckNet by permitting different aspects of the environment to be communicated over it's own channel, or subdivisions of the overall network to be dynamically switched to compensate for damage to the 'network fibre'.

## **7.4 Thesis Summary**

In assessing the effectiveness of the lasers constructed during the project several questions have to be addressed. Primarily, the monolithically fabrication two cavity laser configuration demonstrated relatively good tuning characteristics, side mode suppression ratio, and optical output. In comparison to the earliest demonstrations of these devices during the early eighties, an improvement in the SMSR has been shown. Although already stated, the progress of the multiple cavity tunable laser configuration has progressed to the stage where currently the integration of no fewer than seven cavities, including sections dedicated to optical detection and modulation, provide full wavelength

coverage (180 ITU-50 GHz channels).

The chief advantage two coupled-cavity devices offer over their “technologically advanced” cousins lies with the simplicity of the fabrication stages involved in their construction. The advances and availability of electron beam lithography have been the key factor in permitting true monolithic fabrication of these devices. Although the material system used for the creation of these multi-section lasers allows tunable operation over a relatively small wavelength range, the development of tunable photonic crystal coupled-cavity laser diodes based on InP have demonstrated a quasi-continuous tuning over 36 wavelength division multiplexing channels in a 29.6-nm window [90].

To conclude, a change in material base in conjunction with the technological developments over the last decade could conceivably re-inspire research in a tunable laser configuration, for which, until recently the importance has seemed to have faded.

# Bibliography

- [1] T.H. Maiman. "Stimulated Optical Radiation in Ruby". *Nature*, 187(4736):493–494, August 1960.
- [2] A.L. Schawlow and C.H. Townes. "Infrared and Optical Masers". *Physics Review*, 112(6):1940, 1958.
- [3] M.I. Nathan, W.P. Dumke, G. Burns, P.H. Dill Jr., and G.J. Lasher. "Stimulated Emission of Radiation from GaAs p-n Junctions". *Applied Physics Letters*, 1:62–65, 1962.
- [4] N. Holonyak and S.F. Bevacqua. "Coherent (Visible) Light from GaAs<sub>1-x</sub>P<sub>x</sub> Junctions". *Applied Physics Letters*, 1(4):82–83, December 1962.
- [5] T.M. Quist, R.H. Rediker, R.J. Keyes, W.E. Krag, B. Lax, A.L. McWhorter, and H.J. Zeigler. "Semiconductor Maser of GaAs". *Applied Physics Letters*, 1(4):91, December 1962.
- [6] R.N. Hall, G.E. Fenner, J.D. Kingsley, T.J. Soltys, and R.O. Carlson. "Coherent Light Emission from GaAs Junctions". *PRL*, 9:366–368, 1962.
- [7] N. Holonyak, R. M. Kolbas, R. D. Dupuis, and P. D. Dapkus. "Room-Temperature Continuous Operation of Photopumped MOCVD Al<sub>x</sub>Ga<sub>1-x</sub>As – GaAs – Al<sub>x</sub>Ga<sub>1-x</sub>As Quantum-Well Lasers". *Applied Physics Letters*, 33(1):73–75, July 1978.
- [8] R. D. Dupuis, P. D. Dapkus, R. Chin, Jr. N. Holonyak, and S. W. Kirchoefer. "Continuous 300 K Laser Operation of Single-Quantum-

- Well  $\text{Al}_x\text{Ga}_{1-x}\text{As} - \text{GaAs}$  Heterostructure Diodes Grown by Metalorganic Chemical Vapour Deposition". *Applied Physics Letters*, 34(4):265–267, February 1979.
- [9] Y. Abe, K. Kishino, Y. Suematsu, and S. Arai. "GaInAsP/InP Integrated Laser with Butt-Jointed Built-in Distributed-Bragg-Reflection Waveguide". *Electronics Letters*, 17(25):945–947, 1981.
- [10] K. Kobayashi, K. Utaka, Y. Abe, and Y. Suematsu. "CW Operation of 1.5 - 1.6  $\mu\text{m}$  Wavelength GaInAsP/InP Buried Heterostructure Integrated Twin-Guide Laser with Distributed Bragg Reflector". *Electronics Letters*, 17(11):366–368, 1981.
- [11] M.G. Littman and H.J. Metcalf. "Spectrally Narrow Pulsed Dye Laser without Beam Expander". *Applied Optics*, 17(14):2224–2227, July 1978.
- [12] J. Hill. "Laser Diode Technology and Application". Reprt, Institute of Physics, Pertland State University, March 2005.
- [13] D. Anthon, J.D. Berger, and S. Dutta. "MEMS-tuned devices take on sensing and testing applications". *Laser Focus World*, 40(12):99–103, December 2004.
- [14] P. Chanclou, M. Thual, A. Laurent, J. Lostec, and M. Gadonna. "Wavelength Selector External Cavity Laser Diode by Fiber Switch". *Optical Fiber Technology*, 6(4):329–343, October 2000.
- [15] J.D. Grade, K.Y. Yasumura, and H. Jerman. Advanced, vibration-resistant, comb-drive actuators for use in a tunable laser source. *Sensors and Actuators A-Physical*, 114(2–3):413–422, September 2004.
- [16] Y-P. Lan, C-Y Chen, R-P. Pan, and C-L. Pan. "Fine Tuning of a Diode Laser Wavelength with a Liquid Crystal Intracavity Element". *Optical Engineering*, 43(1):234–238, January 2004.
- [17] Y-P. Lan, R-P. Pan, and C-L. Pan. "Mode-Hop-Free Fine-Tuning of an External-Cavity Diode Laser Wavelength with an Intracavity Liquid Crystal Cell". *Optics Letters*, 29(5):510–512, March 2004.

- [18] M.G. Littman. "Single Mode Operation of Grazing Incidence Pulsed Dye Laser". *Optics Letters*, 3(4):138–140, October 1978.
- [19] A. Densmore, K. Pimenov, and V.I. Tolstikhin. "Integrated Electroabsorption Attenuator-Photodetector for Optical Power Control in WDM Transmission Systems". *IEEE Journal Selected Topics Quantum Electronics*, 8(6):1435–1444, Nov./Dec. 2002.
- [20] J. Struckmeter, A. Euteneuer, B. Smarsly, M. Breede, M. Born, and M. Höfmann. "Electronically Tunable External-Cavity Laser Diode". *Optics Letters*, 24(22):1573–1574, November 1999.
- [21] J. Struckmeier, A. Euteneuer, B. Smarsly, M. Breede, M. Born, M. Hofmann, L. Hildebrand, and J. Sacher. "Electronically tunable external-cavity laser diode". *Optics Letters*, 24(22):1573–1574, November 1999.
- [22] T-S. Shih, Y-P. Lan, Y-F. Lin, R-P. Pan, and C-L. Pan. "Single-Longitudinal-Mode Semiconductor Laser with Digital and Mode-Hop-Free Fine-Tuning Mechanisms". *Optical Engineering*, 12(26):6434–6439, December 2004.
- [23] J.D. Grade, H. Jerman, and T.W. Kenny. "Design of large deflection electrostatic actuators". *Journal of MicroElectroMechanical Systems*, 12(3):335–343, June 2003.
- [24] D. Anthon, J.D. Berger, J. Drake, S. Dutta, A. Fennema, J.D. Grade, S. Hrinya, F. Ilkov, H. Jerman, D. King, H. Lee, A. Tselikov, and K. Yasumura. "External cavity diode lasers tuned with silicon MEMs". *IEEE Leos Newsletter*, 15(5):9–10, 2001.
- [25] K. Liu and M. Littman. "Novel geometry for singlemode scanning of tunable lasers,". *OL*, 6(3):117–118, 1981.
- [26] P.D. Wang, P. Tayebati, D. Vakhshoori, C.C. Lu, M. Azimi, and R.N. Sacks. "Half-Symmetric Cavity Microelectromechanically Tunable Vertical Cavity Surface Emitting Lasers with Single Spatial Mode Operating near 950 nm". *Applied Physics Letters*, 75(7):897–898, August 1999.

- [27] P. Tayebati, P.D. Wang, D. Vakhshoori, and R.N. Sacks. "Widely Tunable Fabry-Perot Filter using Ga(Al)As-AlO(x) Deformable Mirrors". *Photonic Technology Letters*, 10(3):394–396, March 1998.
- [28] T. Wolf, S. Illek, J. Rieger, B. Borchert, and M.C. Amann. "Tunable Twin-Guide (TTG) Distributed Feedback (DFB) Laser with over 10 nm Continuous Tuning Range". *Electronics Letters*, 29(24):2124–2125, November 1993.
- [29] P. Vogel and V. Ebert. "Near Shot Noise Detection of Oxygen in the A-Band with Vertical-Cavity Surface-Emitting Lasers". *Applied Physics B*, 72(1):127–135, January 2001.
- [30] V. Nagali, J.T. Herbon, D.C. Horning, D.F. Davidson, and R.K. Hanson. "Shock-tube Study of High-Pressure H<sub>2</sub>O Spectroscopy". *Applied Optics*, 38(33):6942–6950, November 1999.
- [31] M. Lackner, F. Winter, G. Totschnig, M. Ortsiefer, J. Roskopf, M.C. Amann, and R. Shau. "Spectroscopic Application of Long-Wavelength ( $< 2 \mu\text{m}$ ) VCSEL Diode Lasers". *Technisches Messen*, 70(6):294–305, June 2003.
- [32] J. Wang, S.T., J.B. Jeffries, and R.K. Hanson. "Oxygen Measurements at High Pressures with Vertical Cavity Surface-Emitting Lasers". *Applied Physics B*, 72(7):865–872, May 2001.
- [33] S.T. Sanders, D.W. Mattison, J.B. Jeffries, and R.K. Hanson. "Rapid Temperature Tuning of a 1.4- $\mu\text{m}$  Diode Laser with Application to High-Pressure H<sub>2</sub>O Absorption Spectroscopy". *Optics Letters*, 26(20):1568–1570, October 2001.
- [34] S.T. Sanders, D.W. Mattison, J.B. Jeffries, and R..K. Hanson. "Sensors for High-Pressure, Harsh Combustion Environments using Wavelength-Agile Diode Lasers". *Proceedings of the Combution Institute*, 29(Part 2):2661–2667, 2002.

- [35] C.E. Zah, M.R. Amersfoort B.N. Pathak, F.J. Favire, P.S.D. Lin, N.C. Andreadakis, A.W. Rajhel, R. Bhat, C. Caneau, M.A. Koza, and J. Gamelin. "Multiwavelength DFB Laser Arrays with Integrated Combiner and Optical Amplifier for WDM Optical Networks". *IEEE Journal Selected Topics Quantum Electronics*, 3(4):584–597, April 1997.
- [36] D. Van Thourhout, A. Van Hove, T. Van Caenegem, I. Moerman, P. Van Daele, R. Baets, X.J.M. Leijtens, and M.K. Smit. "Packaged Hybrid Integrated Phased-Array Multi-Wavelength Laser". *Electronics Letters*, 36(5):434–436, March 2000.
- [37] K. Kudo, M. Ishizaka, T. Sasaki, H. Yamazaki, and M. Yamaguchi. "1.52-1.59- $\mu$  m Range Different-Wavelength Modulator-Integrated DFB-LD's Fabricated on a Single Wafer". *Photonic Technology Letters*, 10(7):929–931, July 1998.
- [38] K. Kudo, H. Yamazaki, T. Sasaki, and M. Yamaguchi. "Wide-wavelength range detuning-adjusted DFB-LD's of different wavelengths fabricated on a wafer". *Photonic Technology Letters*, 9(10):1313–1315, October 1997.
- [39] C.E. Zah, M.R. Amersfoort, B. Pathak, F. Favire, P.S.D. Lin, A. Rajhel, N.C. Andreadakis, R. Bhat, C. Caneau, and M.A. Koza. "Wavelength Accuracy and Output Power of Multiwavelength DFB Laser Arrays with Integrated Star Couplers and Optical Amplifiers". *Photonic Technology Letters*, 8(7):864–866, July 1996.
- [40] A. Champagne, M. Lestrade, J. Camel, R. Maciejko, and B. Tromborg. "Degradation of Side-Mode Suppression Ratio in a DFB Laser Integrated with a Semiconductor Optical Amplifier". *IEEE Journal of Quantum Electronics*, 40(7):871–877, July 2004.
- [41] L.A. Coldren. "Multi-section Tunable Laser with Differing Multi-element Mirrors". *U.S. Patent 4 846 325*, 1990.
- [42] V. Jayaraman, L.A. Coldren, S.P. Denbaars, and A. Mathur P.D. Dapkus. "Wide Tunability and Large Mode-Suppression in a Multi-section

- Semiconductor Laser using Sampled Gratings". *Integrated Photonics Research*, paper WF1-1, 1992.
- [43] V. Jayaraman, D.A. Cohen, and L.A. Coldren. "Demonstration of Broadband Tunability in a Semiconductor-Laser using Sampled Gratings". *Applied Physics Letters*, 60(19):2321–2323, May 1992.
- [44] H. Ishii, Y. Tohmori, T. Tamamura, and Y. Yoshikuni. "Modified Multiple-Phase-Shift Super-Structure-Grating DBR Lasers for Broad Wavelength Tuning". *Electronics Letters*, 30(14):1141–1142, July 1994.
- [45] H. Ishii, H. Tanobe, F Kano, Y. Tohmori, Y. Kondo, and Y. Yoshikuni. "Broad-Range Wavelength Coverage (62.4 nm) with Superstructure-Grating DBR Laser". *Electronics Letters*, 32(5):545–455, February 1996.
- [46] H. Ishii, H. Tanobe, F Kano, Y. Tohmori, Y. Kondo, and Y. Yoshikuni. "Quasicontinuous Wavelength Tuning in Super-Structure-Grating (SSG) DBR Lasers". *IEEE Journal of Quantum Electronics*, 32(3):433–441, March 1996.
- [47] H. Ishii, F Kano, Y. Tohmori, Y. Kondo, T. Tamamura, and Y. Yoshikuni. "Broad-Range (34 nm) Quasicontinuous Wavelength Tuning in Superstructure-Grating DBR Laser". *Electronics Letters*, 30(14):1134–1135, July 1994.
- [48] C. Ougier, A. Talneau, F. Delorme, Y. Raffle, J. Landreau, and D.Mathoorasing. "Sampled-Grating DBR Lasers with 80 Addressable Wavelengths Over 33nm for 2.5Gbit/s WDM Applications". *Electronics Letters*, 32(17):1592–1593, August 1996.
- [49] Y. Tohmori, Y. Yoshikuni, H. Ishii, F. Kano, T. TAMAMURA, and Y. KONDO. "Over 100 nm Wavelength Tuning in SuperStructure Grating (SSG) DBR Laser". *Electronics Letters*, 29(4):352–354, February 1993.
- [50] V. Jayaraman, Z.M. Chuang, and L.A. Coldren. "Theory, Design, and Performance of Extended Tuning Range Semiconductor-Lasers with

- Sampled Gratings". *IEEE Journal of Quantum Electronics*, 29(6):1824–1834, June 1993.
- [51] F. Delorme, G. Alibert, C. Ougier, S. Slempek, and H. Nakajima. "Sampled-Grating DBR Lasers with 101 Wavelengths Over 44nm and Optimised Power Variation for WDM Applications". *Electronics Letters*, 34(3):279–281, February 1998.
- [52] J. Gowar. "Optical Communication Systems". Prentice Hall, Second edition, 1993.
- [53] R.E. Wagner and R.C. Alferness. "MONET: Multiwavelength Optical Networking". *Journal of Lightwave Technology*, 14:1349–1355, June 1996.
- [54] B. Mukherjee. Wdm optical communication networks: Progress and challenges. *IEEE Journal on Selected Areas in Communications*, 18(10):1810–1824, October 2000.
- [55] A.P. Kanjamala and A.F.J. Levi. "Wavelength Switching in Multicavity Lasers". *Applied Physics Letters*, 71(3):300–302, July 1997.
- [56] M. Möhrle, B. Sartorius, C. Bornholdt, O. Brox, A. Sigmund, R. Steingrüber, M. Radziunas, and H.-J. Wünsche. "Detuned Grating Multisection-RW-DFB Lasers for High Speed Optical Signal Processing". *IEEE Journal Selected Topics Quantum Electronics*, 7:217–223, 2001.
- [57] L.A. Coldren and S.W. Corzine. "Continuously-Tunable Single Frequency Semiconductor Lasers". *IEEE Journal of Quantum Electronics*, 23(6):903–908, June 1987.
- [58] K. Kobayashi and I. Mito. "Single Frequency and Tunable Laser Diodes". *Journal of Lightwave Technology*, 6(11):1623–1633, November 1988.
- [59] B. Tuck and C. Christopoulos. "Physical Electronics". Edward Arnold, 1986.

- [60] J. Singh. “*Semiconductor Optoelectronics*”. McGraw-Hill, Inc., 1995.
- [61] M.J. Cooke. “*Semiconductor Devices*”. Prentice Hall, 1990.
- [62] S. Wang. “*Fundamentals of Semiconductor Theory and Device Physics*”. Prentice Hall, 1989.
- [63] L. Aucoin, Y.C. Chou, A.N. Downey, R. Ferro, S. Kayali, G.E. Ponchak, and R.R. Romanofsky. “*GaAs Properties, Device Structures and Circuits*”. Jet Propulsion Laboratory, NASA, 1996.
- [64] S.L. Chuang. “*Physics of Optoelectronic Devices*”. John Wiley and Sons Inc, 1995.
- [65] A. Kurobe, H. Furuyama, S. Naritsuka, N. Sugiyama, Y. Kokubun, and M. Nakamura. “Effects of Well Number, Cavity Length and Facet Reflectivity on the Reduction of Threshold Current of GaAs/AlGaAs Multiquantum Well Lasers”. *IEEE Journal of Quantum Electronics*, 24:635–640, 1988.
- [66] M. Rosenzweig, M. Möhrle, H. Düser, and H. Venghaus. “Threshold Current Analysis of InGaAs-InGaAsP Multiquantum-Well Seperate-Confinement Lasers”. *IEEE Journal of Quantum Electronics*, 27(6):1804–1811, June 1991.
- [67] J.S. Osinski, Y. Zou, P. Grodzinski, A. Mathur, and P.D.Dapkus. “Low-Threshold-Current-Density 1.5  $\mu\text{m}$  Laser using Compressively Strained InGaAsP Quantum Wells”. *Photonic Technology Letters*, 4(12):1313–1315, January 1992.
- [68] J.S. Osinski, K.M. Dzurko, S.G. Hummel, and P.D.Dapkus. “Optimisation of Stripe Width for Low-Threshold Operation of Quantum Well Laser Diodes”. *Applied Physics Letters*, 56(25):2487–2489, June 1990.
- [69] P.W.A. McIlroy, A. Kurobe, and Y. Uematsu. “Analysis and Application of Theoretical Gain Curves to the Design of Multi-Quantum-Well Lasers”. *IEEE Journal of Quantum Electronics*, 21:1958–1963, 1985.

- [70] W. Whelan-Curtin. “*The Fabrication of Microstructures for Ultrashort Pulse Generation in Monolithic Modelocked Semiconductor Laser*”. PhD thesis, School of Physics and Astronomy, University of St. Andrews, St. Andrews Scotand, 2005.
- [71] S.P. Cheng, F. Brillouet, and P. Correc. “Design of Quantum Well AlGaAs-GaAs Stripe Lasers for Miniturization of Threshold Current-Application to Ridge Structures”. *IEEE Journal of Quantum Electronics*, 24(12):2433–2440, December 1988.
- [72] T. Makino. “Analytical Formulas for the Optical Gain of Quantum Wells”. *IEEE Journal of Quantum Electronics*, 32(3):493–501, March 1996.
- [73] S.I. Pegg, M.J. Adams, and K. Poguntke. “Absorptive Switching and Spectral Characteristics of the Side-Injection Light-Controlled Bistable Laser Diode”. *IEEE Journal of Quantum Electronics*, 36(1):94–99, January 2000.
- [74] M.B. Flynn. “*Modelling of Monolithic Integrated Semiconductor Diode Lasers as Wavelength Tunable and Ultrashort Puleded Sources*”. PhD thesis, School of Physics and Astronomy, University of St. Andrews, St. Andrews Scotand, 2004.
- [75] A.W. Snyder and J.D. Love. “*Optical Waveguide Theory*”. Chapman and Hall, First edition, 1996.
- [76] T. Tamir. “*Integratged Optics*”. Berlin: Springer Verlag, 1975.
- [77] S. Adachi. “GaAs, AlAs, and  $\text{Al}_x\text{Ga}_{1-x}\text{As}$  - Material Parameters for use in Research and Device Applications”. *Journal of Applied Physics*, 53(3):1–29, 1985.
- [78] R.J. Deri and M.A. Emanuel. “Consistent Formula for the Refractive Index of  $\text{Al}_x\text{Ga}_{1-x}\text{As}$  below the Band Edge”. *Journal of Applied Physics*, 77:4667–4669, 1995.

- [79] D.W. Jenkins. "Optical Constants of  $\text{Al}_x\text{Ga}_{1-x}\text{As}$ ". *Journal of Applied Physics*, 68:1848–1853, 1990.
- [80] A. Yariv. "*Quantum Electronics*". Wiley, New York, Third edition, 1989.
- [81] T.F. Krauss. "*Integrated Semiconductor Ring Lasers*". PhD thesis, Faculty of Engineering, University of Glasgow, May 1992.
- [82] D.T.F. Marple. "Refractive Index of GaAs". *Journal of Applied Physics*, 35(4):1241–1242, April 1964.
- [83] H. Burkhard, H. W. Dinges, and E. Kuphal. "Optical Properties of  $\text{In}_{1-x}\text{Ga}_x\text{P}_{1-y}\text{As}_y$ , InP, GaAs, and GaP Determined by Ellipsometry". *Journal of Applied Physics*, 53(1):655–662, January 1982.
- [84] E.D. Palik. "*Handbook of Optical Constants of Solids*". Academic Press, 1985.
- [85] S. Adachi. "Model Dielectric Constants of GaP, GaAs, GaSb, InP, InAs and InSb". *Physical Review B*, 35(14):7454–7463, May 1987.
- [86] D.A. Yanson. "*Generation of Terahertz-Modulated Optical Signals Using AlGaAs/GaAs Laser Diodes*". PhD thesis, Faculty of Engineering, University of Glasgow, January 2004.
- [87] E. Hecht. "*Optics*". Addison-Wesley Publishing Company, Inc., Second edition, 1987.
- [88] S. Mahnkopf, M. Kamp, A. Forchel, and R. März. "Tunable Distributed Feedback Laser with Photonic Crystal Mirrors". *Applied Physics Letters*, 82:2942–2944, 2003.
- [89] S. Mahnkopf, M. Kamp, R. März, G.H. Duan, V. Colson, and A. Forchel. "Wavelength Switching by Mode Interference of Coupled Cavities with Photonic Crystal Reflectors". *Applied Physics B*, 77:733–737, 2003.
- [90] S. Mahnkopf, R. März, M. Kamp, G.H. Duan, F. Lelarge, and A. Forchel. "Tunable Photonic Crystal Coupled-Cavity Laser". *IEEE Journal of Quantum Electronics*, 40:1306–1314, 2004.

- [91] D. H. Brown, M.B. Flynn, L. O'Faolain, W. Sibbett, and T.F. Krauss. "Coupled Cavity Lasers Incorporating Bragg Mirrors". *IEEE LEOS Meeting*, 2:583–584, 2003.
- [92] L.A. Coldren and T.L. Koch. "Analysis and Design of Coupled-Cavity Lasers - Part II: Transient Analysis". *IEEE Journal of Quantum Electronics*, 20(6):617–623, June 1984.
- [93] L.A. Coldren and T.L. Koch. "Analysis and Design of Coupled-Cavity Lasers - Part I: Threshold Gain Analysis and Design Guidelines". *IEEE Journal of Quantum Electronics*, 20(6):659–670, June 1984.
- [94] C.H. Henry and R.F. Kazarinov. "Stabilization of Single Frequency Operation of Coupled-Cavity Lasers". *IEEE Journal of Quantum Electronics*, 20(7):733–744, July 1984.
- [95] P.G. Agrawal and N.K. Dutta. "*Semiconductor Lasers*". Van Nostrand Reinhold, New York, Second edition, 1993.
- [96] L.A. Coldren, K.J. Ebeling, B.I. Miller, and J.A. Rentschler. "Single Longitudinal Mode-Operation of Two-Section GaInAsP/InP Lasers Under Pulsed Excitation". *IEEE Journal of Quantum Electronics*, 19(6):1057–1062, 1983.
- [97] D. Marcuse and T.P. Lee. "Rate Equation Model of a Coupled Cavity Laser". *IEEE Journal of Quantum Electronics*, 20(2):166–176, 1984.
- [98] J. Buus and M.J. Adams. "Influence of Gap Width on Mode-Discrimination in Cleaved Coupled Cavity Lasers". *Electronics Letters*, 20(14):579–580, 1984.
- [99] L.A. Coldren and T.L. Koch. "Analysis and Design of Coupled-Cavity Lasers - Part I: Threshold Gain Analysis and Gain Guidelines". *IEEE Journal of Quantum Electronics*, 20(6):659–670, June 1984.
- [100] L.A. Coldren, K. Furuya, B.I. Miller, and J.A. Rentschler. "Etched Mirror and Groove-Coupled GaInAsP/InP Laser Devices for Integrated Op-

- tics". *IEEE Journal of Quantum Electronics*, 18(10):1679–1687, October 1982.
- [101] T.L. Koch and L.A. Coldren. "Optimum coupling junction and cavity lengths for coupled-cavity semiconductor lasers". *Journal of Applied Physics*, 57(3):740–754, February 1985.
- [102] C.H. Henry, R.A. Logan, and K.A. Bertness. "Spectral Dependence of the Change in Refractive Index due to Carrier Injection in GaAs Lasers". *Journal of Applied Physics*, 52:4457–4461, 1981.
- [103] J.S. Manning and R. Olshansky. "Carrier-Induced Index Change in Al-GaAs Double-Heterostructure Lasers". *Electronics Letters*, 17(14):506–507, July 1981.
- [104] S. Adachi. "Optical Properties of Al(x)Ga(1-x)As Alloys". *Physical Review B*, 38(17):12345–12352, December 1988.
- [105] M. Alouani, L. Brey, and N.E. Christensen. "Calculated Optical-Properties of Semiconductors". *Physical Review B*, 37(3):1167–1179, January 1988.
- [106] P.A. Wolff. "Theory of the Band Structure of Very Degenerate Semiconductors". *Physics Review*, 126:405–412, 1962.
- [107] B.R. Bennett, R.A. Soref, and J.A. Del-Alamo. "Carrier-Induced Change in Refractive Index of InP, GaAs and InGaAsP". *IEEE Journal of Quantum Electronics*, 26(1):113–122, January 1990.
- [108] L.A. Coldren, G.A. Fish, Y. Akulova, J.S. Barton and L. Johansson, and C.W. Coldren. "Tunable Semiconductor Lasers: A Tutorial". *Journal of Lightwave Technology*, 22(1):193–202, January 2004.
- [109] P.A. O'Brien. "Spatial Coherence in Large Aperture Semiconductor Lasers". PhD thesis, University College Cork, Ireland, 1999.
- [110] A. Yariv. "Optical Electronics in Modern Communications". Oxford University Press, Fifth edition, 1997.

- [111] L.A. Coldren and S.W. Corzine. “*Diode Lasers and Photonic Integrated Circuits*”. John Wiley and Sons Inc., First edition, 1995.
- [112] R. Olshansky, C.B. Su, J. Manning, and W. Powazinik. “Measurement of Radiative and Nonradiative Recombination Rates in InGaAsP and AlGaAs Light Sources”. *IEEE Journal of Quantum Electronics*, 20:838–854, 1984.
- [113] K.A. Lister, B.G. Casey, P.S. Dobson, S. Thoms, D.S. Macintyre, C.D.W. Wilkinson, and J.M.R. Weaver. “Pattern Transfer of a 23 nm-period Grating and Sub-15nm Dots into CVD Diamond”. In *Micro And Nano Engineering*, volume 73–74, pages 319–322, 2004.
- [114] G. Owen and P. Rissman. “Electron beam proximity effect correction by reverse field pattern exposure”, June 1982. United States Patent 4463265.
- [115] R. Wüest, P. Strasser, M. Jungo, F. Robin, D. Erni, and H. Jäckel. “An Efficient Proximity-Effect Correction Method for Electron-Beam Patterning of Photonic-Crystal Devices.”. *Microelectronic Engineering*, 67–68:182–188, 2003.
- [116] Jörgen Bengtsson. “Direct Inclusion of the Proximity Effect in the Calculation of Kinoforms”. *Applied Optics*, 33(22):4993–4996, August 1994.
- [117] K.A. Lister, B.G. Casey, P.S. Dobson, S. Thoms, D.S. Macintyre, C.D.W. Wilkinson, and J.M.R. Weaver. “Total soltion in 157 nm Lithography for low 65 nm node semiconductor devices”. In *Micro And Nano Engineering*, volume 74–74, pages 11–15, 2004.
- [118] R. Wüest, F. Robin, C. Hunziker, P. Strasser, D. Erni, and H. Jäckel. “Limitations of Proximity-Effect Corrections for Electron-Beam Patterning of Planar Photonic Crystals”. *Optical Engineering*, 44(4):1–10, April 2005.
- [119] R. Wüest, P. Strasser, M. Jungo, F. Robin, D. Erni, and H. Jäckel. “An Efficient Proximity-Effect Correction Method for Electron-Beam

- Patterning of Photonic-Crystal Devices". *Microelectronic Engineering*, 67:182–188, 2003.
- [120] S. Yasin, D.G. Hasko, and H. Ahmed. "Comparison of MIBK/IPA and water/IPA as PMMA developers for electron beam nanolithography". In *Microelectronic Eng.*, volume 61–62, page 745, 2003.
- [121] H.H. Berger. "Models for Contacts to Planar Devices". *Solid State Electronics*, 15:145–158, 1972.
- [122] G. Stareev, H. Kunzel, and G. Dortmann. "A Controllable Mechanism of Forming Extremely Low-Resistance Non-alloyed Ohmic Contacts to Group III-V Compound Semiconductors". *Journal of Applied Physics*, 74(12):7344–7356, Dec 1993.
- [123] G. Stareev. "Formation of Extremely Low-Resistance Ti/Pt/Au Ohmic Contacts to P-GaAs". *Applied Physics Letters*, 62(22):2801–2803, May 1993.
- [124] K.S. Sandhu, A.E. StatonBevan, and M.A. Crouch. "Electrical and Microstructural Investigation of Au/Pd/Ti Ohmic Contacts for Al-GaAs/GaAs Heterojunction Bipolar Transistors". *Materials Science and Technology*, 11(10):1083–1088, October 1995.
- [125] G.K. Reeves and H.B. Harrison. "Obtaining the Specific Contact Resistance from Transmission Line Model Measurements". *IEEE Electr. Device Lett.*, 3:111–113, 1998.
- [126] E. Höfling, R. Werner, F. Schäfer, J.P. Reithmaier, and A. Forchel. "Short-cavity Edge-emitting Lasers with Deeply Etched Distributed Bragg Mirrors". *Electronics Letters*, 35(2):154–155, January 1999.
- [127] T.F. Krauss, O. Painter, A. Scherer, J.S. Roberts, and R.M. De La Rue. "Photonic Microstructures as Laser Mirrors". *Opt. Eng.*, 37(4):1143–1148, April 1998.

- [128] Y. Yuan, T. Brock, P. Bhattacharya, C. Caneau, and R. Bhat. "Edge-emitting Lasers with Short-period Semiconductor/air Distributed Bragg Reflector Mirrors". *Photonic Technology Letters*, 9(7):881–883, 1997.
- [129] F. Waibel, E. Ritter, and R. Linsbod. "Properties of TiOx Films Prepared by Electronbeam Evaporation of Titanium and Titanium Suboxides". *Applied Optics*, 42(22):4590–4593, August 2003.
- [130] H. Selhofer, E. Ritter, and R. Linsbod. "Properties of Titanium Dioxide Films Prepared by Reactive Electron-beam Evaporation from Various Starting Materials". *Applied Optics*, 41(2):756–762, February 2002.
- [131] J.E. Bowers, J.E. Bjorkholm, C.A. Burrus, L.A. Coldren, B.R. Hemenway, and D.P. Wilt. "Cleaved-coupled-cavity lasers with large cavity length ratios for enhanced stability". *Applied Physics Letters*, 44(9):821–823, May 1984.
- [132] R.J. Lang and A. Yariv. "Intermodal Stability of a Coupled-Cavity Semiconductor Laser". *IEEE Journal of Quantum Electronics*, 22(5):631–636, May 1986.
- [133] R. J. Lang and A. Yariv. "Analysis of the Dynamic Response of Multi-element Semiconductor Lasers". *IEEE Journal of Quantum Electronics*, QE-21(10):1683–1688, October 1985.
- [134] W.W. Chow and D. Depatie. "Carrier-induced Refractive-index change in Quantum-well Lasers". *Optics Letters*, 13(4):303–305, April 1988.
- [135] J.A. Nelder and R. Mead. "A Simplex Method for Function Minimization". *Computer Journal*, 7:308–313, 1965.
- [136] M.F.C. Stephens, D. Nasset, K.A. Williams, E.A. Kelly, R.V. Penty, I.H. White, and M.J.Fice. "Wavelength Conversion at 40 Gbit/s via Cross-Gain Modulation in Distributed Feedback Laser Integrated with Semiconductor Optical Amplifier". *Electronics Letters*, 35(20):1762–1764, September 1999.

- [137] B.S. Ooi, K. McIlvaney, M.W. Street, A.S. Helmy, S.G. Ayling, A.C. Bryce, J.H. Marsh, and J. S. Roberts. "Selective Quantum-Well Inter-mixing in GaAsAlGaAs Structures Using Impurity-Free Vacancy Diffusion". *IEEE Journal of Quantum Electronics*, 33(10):1784–1793, October 1997.